Nagarjuna Remalli

An Investigation of Low Temperature Creep Controlling Mechanisms in a Martensitic Spring Steel

Schriftenreihe des Lehrstuhls
für Werkstoffsysteme für den Fahrzeugleichtbau
im Institut für Werkstofftechnik

Herausgeber: Prof. Dr. rer nat. Robert Brandt

Band 4

Dissertation, Universität Siegen, 2023

"An Investigation of Low Temperature Creep Controlling Mechanisms in a Martensitic Spring Steel" in *Schriftenreihe des Lehrstuhls für Werkstoffsysteme für den Fahrzeugleichtbau im Institut für Werkstofftechnik*
1. Auflage, 4. Band

Herausgeber:
Prof. Dr. rer. nat. Robert Brandt
Universität Siegen, Fakultät IV: Naturwissenschaftlich-Technische Fakultät, Department Maschinenbau, Lehrstuhl für Werkstoffsysteme für den Fahrzeugleichtbau, Am Eichenhang 50, 57076 Siegen, Deutschland

Autor:
Nagarjuna Remalli

Umschlaggestaltung, Druck und buchbinderische Verarbeitung:
UniPrint, Universität Siegen
Hölderlinstraße 3, 57076 Siegen, Deutschland

ISSN: 2700-7529

Gedruckt auf alterungsbeständigem holz- und säurefreiem Papier.

An Investigation of Low Temperature Creep Controlling Mechanisms in a Martensitic Spring Steel

DISSERTATION
to obtain the degree of Doctor
of Engineering

submitted by
Nagarjuna Remalli, M.Tech.

submitted to the School of Science and Technology
of the University of Siegen
Siegen 2023

Supervisor and first appraiser

Prof. Dr. rer. nat. Robert Brandt

University of Siegen

Second appraiser

Prof. Koteswararao V. Rajulapati

University of Hyderabad

Date of the oral examination

23.11.2023

Dedicating

to

Prof. Dr.-Ing. Vadali V. S. S. Srikanth

Acknowledgements

This work was financially supported by "Indo-German Science and Technology Centre (IGSTC)" under grant number: 01DQ19006A. Sincere thanks to Mr. Hans Westphal and Mrs. Alexandra Stinner (Deutsches Zentrum für Luft- und Raumfahrt) for their kind support during the execution of this project. Thanks to the Industrie- und Handelskammer (IHK) Siegen for the financial support through the IHK-Siegen fellowship in the early stages of my research.

Sincere thanks to my supervisor, Professor Robert Brandt who gave me the opportunity to do doctoral research. The technical advice and the freedom he has given me to pursue this research are acknowledged. His time spent in discussions and review of this research is highly appreciated.

Despite the hurdles caused by COVID-19, the efforts of Dr. Manjini Sambandam and Mr. Gobinath Rajavel (JSW Steel Ltd. Salem Works), as well as Mr. Steffen Klapprott and Mr. Jens Heßland (Mubea Fahrwerksfedern GmbH, Weißensee) in delivering the material in a timely manner are appreciated. The cooperation of Professor Koteswararao V. Rajulapati and his students Mr. Mohsin Hasan and Mr. Nanda Kishore Karnam (University of Hyderabad) with heat treatment is acknowledged. I thank Professor Frank Walther and his scientific staff (TU Dortmund) for their support with low temperature creep testing. A part of this work was performed at the "Micro- and Nanoanalytics Facility (MNaF)" of the University of Siegen. Thanks to Dr. Yilmaz Sakalli for providing me with training on electron microscopes.

I acknowledge the help from Professor Bhanu Sankara Rao Kota during the early stages of this project by providing me with pertinent information.

It was a pleasure working at "Lehrstuhl für Werkstoffsysteme für den Fahrzeugleichtbau". I thank all my colleagues for their support in the execution of this project. My special thanks go to Mr. Mathias Münch who made my stay in Siegen comfortable. The time spent in scientific discussions with him is highly appreciated. Many thanks to the student assistants Tomas Feldberg, Maximilian Zink, Sarah Usmani, and Jule Beineke who assisted me during the course of this investigation. Without their support, it is not feasible to complete this dissertation in a timely manner. I thank Dr. Johny Varghese for proofreading the draft.

Many thanks to Mr. Srikanth Batna and Mr. Balu Danavath, Mrs. Supriya Patibanda, and Mrs. Pratyusha Turlapati for being just a phone call away. I sincerely

thank many great Telugu scholars, especially Mr. Veturi Sundararama Murthy and Mr. Chembolu Seetharama Sastry for accompanying me through their literary works.

Finally, I owe so much to my parents for the freedom and support given to pursue my wishes. I especially thank my brother, *Uttili* for showering unconditional love and for being my stress buster.

Siegen, December 2023
Nagarjuna Remalli

Abstract

The rising demand for electric vehicles urges automotive suppliers to push their limits on the sag resistance of suspension coil springs. However, the mechanisms contributing to sag loss in a coil spring or low temperature creep (LTC) in martensitic spring steel (MSS) are still unclear. Furthermore, the LTC rate-controlling mechanisms in MSS remain elusive. In the current research, an attempt has been made to unfold the LTC rate-controlling mechanisms in SAE 9254 steel grade.

First and foremost, the LTC mechanism-based models, i.e. strain hardening theory (SHT), and exhaustion creep model (ECM) are developed to make them capable of describing the stress σ and temperature T dependent LTC strain of a material. Subsequently, the modified SHT and reworked ECM are verified and validated at the example of SAE 9254. The temperature-dependent LTC behavior of inductively quenched and tempered (IQT) SAE 9254 and martempered SAE 9254 are studied at the temperatures 298 $K \leq T \leq 353$ K for a duration of 1 hr at each condition. The stress σ dependent LTC behavior of IQT SAE 9254 is studied at the stresses 1071 $MPa \leq \sigma \leq 1634$ MPa, and the stress σ dependent LTC behavior of martempered SAE 9254 is studied at the stresses 421 $MPa \leq \sigma \leq 632$ MPa.

A combined analysis by means of (i) the reworked ECM, and (ii) advanced microstructural characterization prior to and post LTC suggests that dislocation glide, mainly localized in the metastable retained austenite phase, is one of the basic LTC contributing mechanisms in SAE 9254. Stress-assisted martensitic transformation (SAMT) and, at elevated temperatures, strain-induced martensitic transformation (SIMT) are the additional LTC contributing mechanisms. Furthermore, the considered approach suggests that the LTC rate-controlling mechanisms are stress-assisted recovery (SAR), SAMT, and, at elevated temperatures, SIMT.

Kurzfassung

Die steigende Nachfrage nach Elektrofahrzeugen zwingt Automobilzulieferer dazu, ihre Grenzen bei der Setzfestigkeit von Fahrwerksfedern zu erweitern. Der Mechanismus, der zum Setzverlust einer Fahrwerksfeder oder zum Low Temperature Creep (LTC) eines martensitischen Federstahls beiträgt, ist jedoch noch unklar. Darüber hinaus ist ebenfalls der Kriechraten kontrollierende Mechanismus im Tieftemperaturbereich nicht bekannt. In der aktuellen Studie wurde versucht, den Kriechraten kontrollierenden Mechanismus im Tieftemperaturbereich für die Stahlsorte SAE 9254 zu ermitteln.

Zunächst werden die LTC-Mechanismusbasierten Modelle, d.h. die Strain Hardening Theory (SHT) und das Exhaustion Creep Model (ECM) weiterentwickelt. Anschließend werden die modifizierten LTC-Mechanismusbasierten Modelle verifiziert und am Beispiel der Stahlsorte SAE 9254 validiert. Es werden die mechanischen Eigenschaften des Inductively Quenched and Tempered (IQT) und martemperten SAE 9254 im Temperaturbereich von 298 $K \leq T \leq 353$ K für eine Stunde untersucht. Der überprüfte Spannungsbereich für das spannungsabhängige LTC-Verhalten liegt im Fall von IQT zwischen 1071 $MPa \leq \sigma \leq 1634$ MPa und im Fall des martemperten Stahl zwischen 421 $MPa \leq \sigma \leq 632$ MPa.

Eine zusammenhängende Analyse mit Hilfe (i) eines mechanismusbasierten ECM und (ii) einer erweiterten mikrostrukturellen Charakterisierung vor und nach dem LTC legt nahe, dass das Versetzungsgleiten, welches hauptsächlich in der Restaustenit-Phase stattfindet, ein grundlegender Mechanismus des LTC ist. Der hier vorgestellte Ansatz berücksichtigt die Stress Assisted Recovery (SAR) und die Stress-Assisted Martensitic Transformation (SAMT) für niedrigere Temperaturen sowie die Strain-Induced Martensitic Transformation (SIMT) bei erhöhten Temperaturen als Kriechraten kontrollierenden Mechanismus.

Contents

List of Abbreviations and Symbols

Abbreviations

BEV	Battery Electric Vehicles
BSE	Back-Scattered Electron
CRSS	Critical Resolved Shear Stress
DIC	Digital Image Correlation
EBSD	Electron Back Scattered Diffraction
ECM	Exhaustion Creep Model
FCC	Face Centered Cubic
FWHM	Full Width at Half Maximum
ICE	Internal Combustion Engine
IPF	Inverse Pole Figure
IQT	Inductively Quenching and Tempering
KAM	Kernel Average Misorientation
LTC	Low Temperature Creep
MSS	Martensitic Spring Steel
PAG	Prior Austenite Grain
RoA	Reduction of Area
SAMT	Stress Assisted Martensitic Transformation
SAPD	Stress Assisted Plastic Deformation
SAR	Stress Assisted Recovery
SDE	Strength Differential Effect
SE	Secondary Electron
SEM	Scanning Electron Microscope

SFE	Stacking Fault Energy
SHT	Strain Hardening Theory
SIMT	Strain Induced Martensitic Transformation
TIT	Thermal Induced Transformation
TRIP	Transformation Induced Plasticity
TTT	Time-Temperature-Transformation
TWIP	Twinning Induced Plasticity
UTS	Ultimate Tensile Strength
XRD	X-ray Diffraction
YS	Yield Strength

Important Symbols

α'	Tempered martensite	
γ	Retained austenite	
ϵ	Epsilon carbide	
Ac_3	Austenization temperature	[K]
M_s	Martensitic start temperature	[K]
M_f	Martensitic finish temperature	[K]
σ	Applied stress	[Pa]
T	Temperature	[K]
σ_e	Yield strength	[Pa]
ε_{cr}	LTC strain	[−]
$\dot{\varepsilon}_{cr}$	LTC rate	[1/s]
t	Creep time	[s]
α^S	SHT creep parameter	[−]
δ^S	SHT creep parameter	[1/s]
k	Boltzmann constant	[J/K]
h	Planck constant	[J/s]
ν_e	Activation volume	[m^3]

f_0	Vibration frequency	[1/s]
P	Number of pairs	[−]
V	Unit cell volume	[m^3]
ρ	Dislocation density	[$1/m^2$]
ρ_m	Mobile dislocation density	[$1/m^2$]
l	Average length of mobile dislocation	[m]
G_i	Inherent activation energy	[J/mol]
ΔG_i	Net activation energy	[J/mol]
G_e	Maximum inherent activation energy	[J/mol]
ν_i	Inherent activation volume	[m^3]
σ_i	Inherent activation stress	[Pa]
$\Delta\sigma_i$	Net activation stress	[Pa]
g_i	Specific activation energy	[−]
Δg_i	Specific net activation energy	[−]
N	Total number of obstacles per unit volume	[−]
$N(g_i)$	Relative number of obstacles with specific activation energy g_i	[−]
$\phi(g_i)dg_i$	Normalized obstacle distribution function	[−]
$N_\sigma(\Delta g_i)$	Effective number of obstacles with specific net activation energy Δg_i	[−]
$\phi_\sigma(\Delta g_i)d(\Delta g_i)$	Effective obstacle distribution function	[−]
ρ_m^a	Activated mobile dislocation density	[$1/m^2$]
$q(t)$	Probability function for the activation of pairs	[−]
ΔL_σ	Average effective distance moved by mobile dislocation element	[m]
ΔL	Average distance between two pairs in adjacent unit cells	[m]
M	Taylor factor	[−]
b	Burgers vector	[nm]
$\varphi(\Delta g_i)$	Fraction of thermally activated dislocation elements	[−]

f_w	Vibration frequency of dislocation element to surmount the obstacle successfully	[1/s]
t_w	Average waiting time of dislocation element in front of the obstacle	[s]
σ_G	Internal opposing stress	[Pa]
h	Strain hardening coefficient	[Pa]
$p\left(\Delta g_i, t\right)$	Probability function of survival of a dislocation pair	[−]
α^E	ECM creep parameter	[−]
f_0^*	ECM creep parameter	[1/s]
f_1^*	ECM creep parameter	[1/s]
l^*	Gauge length	[mm]
d	Gauge diameter	[mm]
2θ	Diffraction angle	[°]
D	Crystallite size	[nm]
$M_\perp$	Dislocation distribution factor	[−]
$\overline{C}$	Average dislocation contrast factor	[−]

List of Figures

List of Tables

Chapter 1

Introduction

1.1 Engineering Background

Martensitic spring steels (MSS) used in commercial spring applications are known for their superior sag resistance and fatigue strength. The primary functions of suspension coil springs are the absorption of shocks and vibrations, and the prevention of wheel lift to ensure a good grip of wheels while coping with the weight of a passenger car. The coil spring undergoes a progressive deformation, i.e. sag loss caused by loading during service. The rate of a suspension coil spring does not change by sag loss. However, the load taken by coil spring decreases which affect the spring characteristics, (a) the driver's ability to steer the car safely, (b) ride height, (c) riding quality, and (d) reduction of payload. This technical problem becomes acute when considering the recent trend towards electric vehicles since electric vehicles, especially battery electric vehicles (BEV), are heavier than internal combustion engine (ICE) vehicles. The design stress of the coil springs being used currently is limited and may not withstand very high design stresses that exist in the case of BEV. Hence, there is still a need to improve either the sag resistance of coil spring or low temperature creep (LTC) resistance of spring steel in accordance with the standards of BEV. Improvements in the LTC resistance of spring steels have been achieved through a heuristic approach, i.e. raising the tensile strength of MSS by a laborious process of effective micro-alloying and heat treatment [1–6]. Although the raise in tensile strength improves the LTC resistance, the fatigue strength under corrosive environment, and formability of MSS would be adversely affected. Besides, the high tensile strength of MSS causes problems during a coil spring fabrication process, e.g. cutting tool damage and wire rod breakage. Surprisingly, few LTC investigations on martensitic steels revealed that the LTC resistance does not depend on the tensile strength of the material [7–12]. Thus, there is a pressing need to understand the mechanisms on a microscopic scale contributing to the macroscopic LTC strain for further development of an advanced MSS. However, the underlying mechanisms responsible for LTC in MSS still remain elusive.

Hence, the current research is targeted to unfold the LTC rate-controlling mechanisms in an MSS.

1.2 Scientific Background

Creep is defined as a time-dependent plastic deformation at a constant stress σ less than the yield strength (YS) σ_e, and at a constant temperature T less than the melting temperature T_m of a material. Depending on the applied temperature T, creep is classified as LTC ($T < 0.3 \cdot T_m$), intermediate creep ($0.3 \cdot T_m \leq T \leq 0.6 \cdot T_m$), and high temperature creep ($T > 0.6 \cdot T_m$). Figure 1.1(a) shows the schematic representation of the loading process in creep testing. The creep strain $\varepsilon_{cr}(t)$ is then defined by the

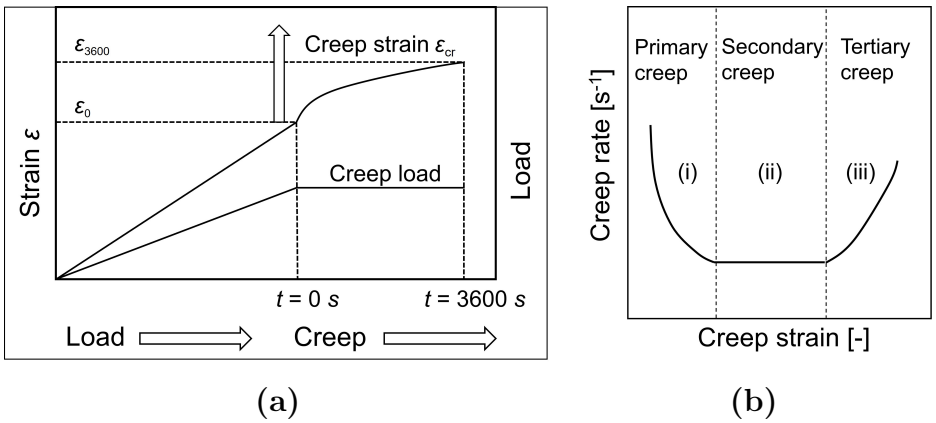

Figure 1.1: (a) Schematic representation of loading process in creep testing[13], (b) Creep rate $\dot{\varepsilon}_{cr}(t)$ as a function of creep strain $\varepsilon_{cr}(t)$[14]

change of strain after achieving the creep load σ, i.e.

$$\varepsilon_{cr}(t) = \varepsilon(t) - \varepsilon_0 \tag{1.1}$$

here $\varepsilon_{cr}(t)$, $\varepsilon(t)$, and ε_0 are time-dependent creep strain, total strain, and instantaneous strain, respectively[13]. The creep strain $\varepsilon_{cr}(t)$ typically consists of three stages: (i) the primary stage, (ii) the secondary stage, and (iii) the tertiary stage (s. Figure 1.1(b)). In the primary stage, the creep rate $\dot{\varepsilon}_{cr}(t)$ decreases with creep strain. During the secondary or steady stage, the creep rate reaches a minimum and remains constant. The creep rate increases rapidly in the tertiary creep until the fracture occurs.

Ample amount of LTC investigations on a wide range of materials, e.g. Ti-alloys[15–17], stainless steel[18;19], pipeline steel[20], Cu[21], and pure Al[22] have been performed over the last three decades, which are summarised by Kassner et al.[23]. However, the LTC investigations confined to high-strength martensitic steels, especially under the restricted conditions of $\sigma < \sigma_e$ and $T < T_m$, are limited[9–13;24–28], and

these results were reported that LTC strain ε_{cr} in high-strength martensitic steels is confined to the primary stage creep only.

Improvements in LTC resistance of MSS have been achieved by raising the tensile strength of spring steel through targeted application of various strengthening mechanisms[1–8]. Kawasaki et al.[2] examined the room temperature sag loss behavior of coil springs made of SAE 9254 steel grade under maximum torsion stress of 1126 MPa applied for 96 hr. They reported an improvement in the sag resistance of coil springs with a raise in the tensile strength of SAE 9254. It was presumed that the fine grain structure attained by inductively quenching and tempering (IQT) technology and retained austenite (γ) phase are effective for strengthening SAE 9254[3]. However, later, they speculated that carbide precipitation is more effective than γ phase in IQT spring steel[3]. Yamamoto et al.[5] considered SUP7 and SUP7-Nb-V steel grades to evaluate the sag loss behavior of coil springs by torsion LTC tests. An improvement in the sag resistance of coil springs was noticed with an increase in the hardness of spring steel grades. Furthermore, the SUP7-Nb-V exhibited superior sag resistance than SUP7, which was attributed to the precipitation-hardening effect of carbide-forming elements V and Nb, and the noticed grain refinement was only a co-product of the simultaneous addition of these elements. It was presumed that sag loss in coil springs resulted from the movement of mobile dislocations. Consequently, they speculated that NbC and V_4C_3 precipitates, as well as prior austenite grain (PAG) boundaries, act as obstacles for mobile dislocations in SUP7-Nb-V steel[5]. Nam et al.[29] considered the torsional Bauschinger test[1] to evaluate the sag resistance of Si-Cr spring steel. Their results suggest that the addition of Mo and W enhances the sag resistance of Si-Cr spring steel, which was attributed to the precipitation-hardening effect by stabilizing the cementite particles during the tempering of Si-Cr spring steel[29]. Tata et al.[1] reported an improvement in the sag resistance of coil springs with increasing Si content up to 2.2 wt.%, which was attributed to the precipitation-hardening effect by refining and stabilizing the ϵ-carbides. Choi[31] proposed a unique step tempering method to increase the density of ϵ-carbides. Si is also considered an effective element to enhance the LTC resistance of MSS through solid solution strengthening[32]. Irrespective of the strengthening mechanisms, the authors mentioned above presumed that the LTC strain in MSS is contributed by dislocation glide. Therefore, the attained improvement in LTC resistance while strengthening MSS was speculated to be a result of hindering the movement of mobile dislocations by obstacles such as PAG boundaries, precipitates, and carbides. However, none of them has provided evidence for the hypothesis. The work of Yamamoto et al.[5] revealed that the sag resistance decreases with in-

[1]The hysteresis loop area measured in the torsional Bauschinger test is directly proportional to the sag resistance of coil spring[30]

creasing hardness of MSS beyond HV 550. Surprisingly, few LTC investigations on martensitic steels revealed that the LTC resistance does not depend on the tensile strength of the material[7–12].

In contrast to the above-mentioned efforts, Murai et al.[7;8] achieved an improvement in the LTC resistance of SAE 9254 steel without altering its tensile strength through warm deformation of QT wire rod by means of cyclic bending. According to them, the imposed 2.9% strain led to an increase in the dislocation density by the formation of a rigid dislocation network that effectively interlocks the existing mobile dislocations. Consequently, they speculated that the LTC resistance was improved due to the reduction in density of mobile dislocations, which are presumed to be LTC contributors[7]. Zhao et al.[9] reported that the LTC strain of high strength low carbon low alloy steel wire was decreased by 65% due to warm deformation at 573 K for 300 s. Like Murai et al., the reduction in LTC strain was attributed to the reduction in mobile dislocation density due to dislocation rearrangement, which was determined with the aid of X-ray diffraction (XRD). Besides, they reported a simultaneous increase in internal friction by the re-dissolution of solute atoms yielded by warm deformation.

The LTC studies of Liu et al.[10–12] on SAE 4340 containing minor ferritic phase in the tempered martensite (α') matrix revealed that the LTC resistance depends on neither hardness nor YS σ_e of the material. The SAE 4340 samples having the same hardness of 52 ± 0.5 HRC and YS σ_e of 1280 ± 10 MPa but different ferrite contents of $0 - 4\%$ have setup through optimizing the heat treatment parameters. It is observed that the SAE 4340 multiphase steel exhibit significant room temperature creep strain ε_{cr} which increases with increasing ferrite content. It was claimed that the LTC strain was rather predominantly contributed by slip localization in the minor ferrite phase of SAE 4340 steel[10–12]. Alfredsson et al.[26] have investigated the LTC deformation behavior of high-strength martensitic roller-bearing steel with γ as a secondary phase. They considered both dislocation glide and γ phase transformation as LTC contributing mechanisms for their mechanical materials model.

Although the direct experimental evidence is still due, the above-mentioned authors have unanimously proposed dislocation glide as one of the basic mechanisms of the primary stage LTC behavior of MSS. However, to the knowledge of the author, no study has addressed the LTC rate-controlling mechanisms in MSS so far. Therefore, the current research is targeted to disclose the LTC rate-controlling mechanisms in SAE 9254 steel through an approach of combined analysis by means of (i) an LTC mechanism-based model, and (ii) advanced microstructural characterization prior to and post LTC. The research objectives and a roadmap to achieve them are comprehensively described in Chapter 3.

Chapter 2

State of the Art Technology and Literature Review

2.1 Martensitic Spring Steels: Effect of Micro-Alloying

The primary property requirements of spring steels used in commercial suspension coil springs are high sag resistance, fatigue strength, high hardenability, and ultimate tensile strength (UTS) with a decent amount of reduction of area (RoA). The spring steels are categorized based on their strength as UTS of 1200 MPa, 1800 MPa, and 2000 MPa. Up to 1200 MPa requirements, simple low alloy steels are adequate. The 1800 MPa steels are high Si-Cr low alloy steels[31]. The 2000 MPa steels are a special class of high Si steels with additional micro-alloying. The micro-alloying of the spring steel plays a very key role in improving UTS as well as ductility which affects the spring formability.

In general, the 2000 MPa steels are medium C steel (0.5 wt.%) with additional micro-alloying elements usually Si, Cr, Mn, Mo, V, and Nb. The addition of Si provides tempering resistance by delaying the transition of ϵ-carbides to cementite during tempering[33–38]. Furthermore, the growth of cementite particles is controlled since Si rejected from cementite particles acts as a growth barrier and yields a refined dispersion of cementite particles[34;39]. Consequently, the sag resistance is enhanced through stabilizing the ϵ-carbides and refining the cementite particles[1]. However, surface decarburization is a major concern for Si-rich spring steels, e.g. SAE 9260. Cr suppresses the decarburization caused by high Si content and improves the hardenability, simultaneously[2]. The addition of Cr and/or Mo provides tempering resistance by refining cementite particles at higher tempering temperatures of $T > 673\ K$[40]. Mn contributes to high hardenability and enhanced UTS through dislocation pinning by solid solution strengthening. The addition of V and Nb improves the fatigue strength

and sag resistance of spring steel by ensuring grain refinement through effectively interlocking the PAG boundaries with the fine precipitates VC and NbC[6;29].

The spring steels usually supplied by steel makers are in the form of hot rolled wire rods having UTS $\approx$ 900 MPa, which can be attributed to the microstructure containing softer phases, i.e. pearlite and ferrite[41]. The as-received hot rolled wire rods undergo the QT process to meet the requirements of a component maker, i.e. UTS of $\geq$ 2000 MPa with a decent amount of RoA through the formation of hard martensitic microstructure. The microstructure evolution during the QT process of spring steel is described in the following section.

2.2 Retained Austenite in Martensitic Spring Steel

The schematic representation of microstructure evolution during the QT process of spring steel is shown in Figure 2.1. To begin with, the as-received wire rods are heated and held enough time at the above austenitization temperature (Ac_3) to obtain austenitic microstructure. Subsequently, these wire rods are quenched using a quenching media which is often maintained at a temperature T below the martensitic start temperature (M_s). Water, oil, and compressed air are the most commonly used quenching media. Due to the rapid cooling rate in the quenching process, the austenite phase transforms into a hard, brittle martensitic phase. However, a part of the austenite remains in the martensitic matrix without undergoing transformation during quenching which is recognized as retained austenite (γ) phase[42]. The volume fraction of the γ phase retained after quenching depends on the factors, e.g. quenching media, temperature, and time.

The as-quenched MSS exhibit high strength and low ductility owing to the hard martensitic matrix with supersaturated C content, which affects the formability of spring steel. Thus, a second stage of heating, called tempering, is adopted, i.e. reheat the as-quenched wire rods to the temperatures $T \geq 373\ K$ to improve the ductility while maintaining reasonably high UTS[43]. The structural changes that occur during the tempering of martensitic microstructure are divided into the aging and tempering process[44]. At low tempering temperatures $T < 373\ K$, the martensitic phase undergoes aging, i.e. the highly mobile C atoms in the quenched martensite phase rearrange themselves and migrate to the interfaces, e.g. dislocations, lath boundaries[44]. The tempering of MSS is classified into three stages depending on the tempering temperature. During stage 1 tempering $423\ K \leq T \leq 523\ K$, the supersaturated C atoms in the as-quenched martensite precipitate as transition ϵ-carbides ($Fe_{2.4}C$) with hexagonal crystal packing[45]. Consequently, the C content in the supersaturated martensite

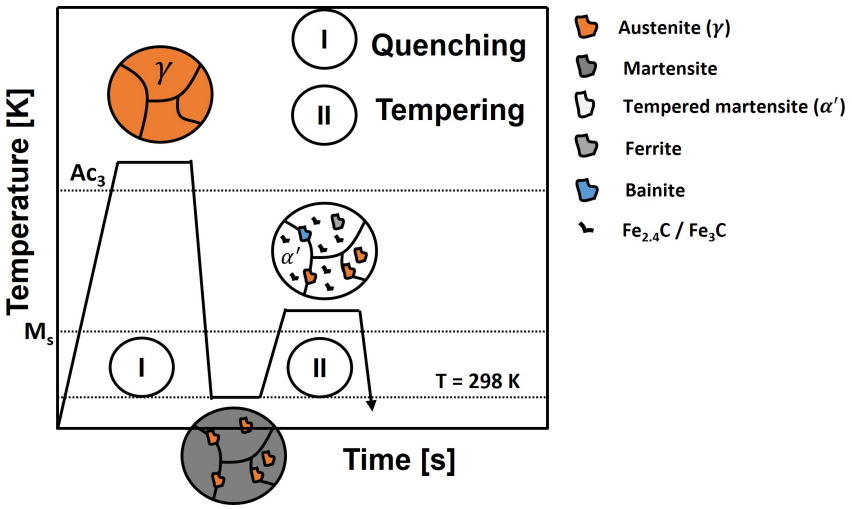

Figure 2.1: Schematic representation of microstructure evolution during the QT process of spring steel

is reduced to about 0.25 wt.% and the resulting matrix with low C content is recognized as tempered martensite (α')[46]. During stage 2 tempering 473 $K \leq T \leq 573$ K, the metastable γ phase decomposes into ferrite and cementite (Fe_3C) particles. During stage 3 tempering $T \geq 523$ K, the transition ϵ-carbides in the α' phase transform to stable cementite particles with orthorhombic crystal structure[47;48]. The coarsening and spheroidization of cementite particles take place with a further increase in tempering temperature and/or tempering time.

In industrial practice, the QT process is performed by means of either conventional furnace treatment[31] or inductive treatment[2;49] or a combination of both to achieve the desired mechanical properties of MSS. The adopted heat treatment technology (i.e. furnace vs inductive) certainly has an impact on the mechanical properties and microstructural features of MSS. The rapid heating rate and shorter processing time in IQT are advantages to obtaining superior mechanical properties without surface decarburization. However, the α' matrix attained through IQT technology contains a relatively high dislocation density due to a lack of time for dislocation annihilation and recovery. Consequently, the precipitation behavior of cementite gets affected[50]. Furthermore, the IQT process caused micro-segregation of C and additional micro-alloying elements owing to short processing time[50;51]. Consequently, there exists a variation in martensitic start temperature M_s locally on a microscopic scale which led to the inhomogeneous distribution of γ phase in MSS.

Stability of Retained Austenite

MSS contains a significant amount of γ phase due to the incomplete martensitic transformation during the QT process. The γ phase in MSS exists in metastable nature owing to its supersaturated C content at the ambient conditions. Indeed, the stability of the γ phase in martensitic steels depends on several factors, e.g. chemical composition, morphology, stress, temperature, strain, and strain rate[52]. The elements Mn and Ni act as γ phase stabilizers[53;54]. Surprisingly, it was reported that high Si content promotes the stability of the γ phase on quenching through increasing the C concentration of γ phase[55;56]. The γ phase in martensitic steel exists in the form of blocky γ_B and filmy γ_F morphologies. The blocky γ_B phase is located in the vicinity of PAG boundaries, whereas the filmy γ_F phase is present along the lath boundaries of α' phase, predominantly[57]. It is commonly reported that the blocky γ_B phase is relatively less stable in comparison with the filmy γ_F phase due to its bigger size and low carbon content. Thus, the blocky γ_B phase transforms to martensite during deformation, whereas the filmy γ_F phase retains stability even after fracture[58]. However, the filmy γ_F phase is vulnerable to elevated temperatures and decomposes to ferrite and cementite particles owing to its high carbon content[59]. The low strain rates in a tensile deformation promote the transformation of γ to α' phase, and the rate of transformation suppresses at higher strain rates due to the lack of time for heat dissipation. The heat generated during tensile deformation at higher strain rates would raise the temperature locally, and then stabilize the γ phase[60].

2.3 Deformation Mechanisms in Retained Austenite

The plastic deformation in γ phase is primarily contributed by means of dislocation glide owing to its face-centered cubic (FCC) crystal structure with high symmetry and 12 possible slip systems[14]. The most favorable slip system in γ phase is $\{111\} < 110 >$, where $\{111\}$ is the close packed plane and $< 110 >$ is the slip direction. The Burgers vector of a perfect dislocation for the considered slip system of γ phase is $\frac{a}{2}[10\overline{1}]$, with a being the lattice parameter. The energy of a dislocation is directly proportional to the square of the magnitude of its Burgers vector. Thus, the perfect dislocation, $\frac{a}{2}[10\overline{1}]$ in the γ phase is often dissociating into partial dislocations, $\frac{a}{6}[11\overline{2}]$ and $\frac{a}{6}[2\overline{11}]$, to reduce the line energy[61]

$$\frac{a}{2}[10\overline{1}] \rightarrow \frac{a}{6}[11\overline{2}] + \frac{a}{6}[2\overline{11}]. \tag{2.1}$$

The dissociation width between the partial dislocations depends on the stacking fault energy (SFE) which is a function of the material's composition[62;63] and the temperature[64]. It is often reported that the smaller the SFE, the greater the dissociation width between partial dislocations[65]. Consequently, the magnitude of SFE plays a decisive role in the activation of secondary deformation mechanisms, i.e. transformation-induced plasticity (TRIP), and twinning-induced plasticity (TWIP) along with dislocation glide in the γ phase. Figure 2.2 shows the temperature T dependence of SFE of SAE 9254 steel grade generated by JMatPro® software. The SFE increases linearly with temperature T in the range of $283K \leq T \leq 373K$. It is often reported that with decreasing SFE, the active deformation mechanisms in γ phase change from (i) dislocation glide to (ii) dislocation glide and TWIP to (iii) dislocation glide and TRIP[63;66;67]. The TRIP mechanism is activated at low SFE $< 20\ {}^{mJ}/_{m^2}$, whereas the TWIP mechanism becomes active for SFE of $20 - 40\ {}^{mJ}/_{m^2}$. Beyond SFE $> 40\ {}^{mJ}/_{m^2}$, the plasticity in γ phase is contributed by dislocation glide solely[68].

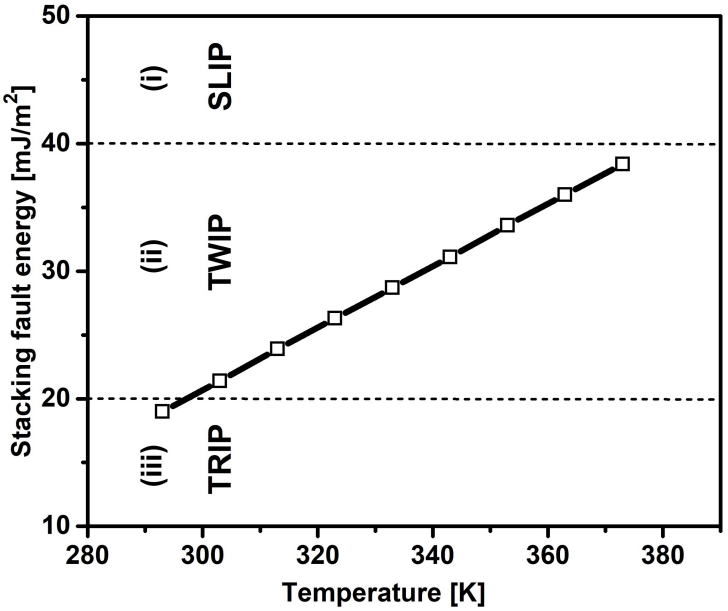

Figure 2.2: Temperature dependence of SFE for SAE 9254 composition determined by means of JMatPro® software

Transformation Induced Plasticity

The $\gamma \rightarrow \alpha'$ phase transformation is driven by a decrease in the change in Gibbs free energy (ΔG)

$$\Delta G = \Delta G_{ch} + \Delta G_{mech} \tag{2.2}$$

with ΔG_{ch} being the change in chemical free energy, i.e. the difference between free energies of γ and α' phases, ΔG_{mech} being the mechanical free energy associated with

the strain energy generated by applied stress σ as shown in Figure 2.3[69]. The chemical free energy ΔG_{ch} decreases with increasing temperature T. Thus, the additional free energy ΔG_{mech} contribution must increase with the raise in temperature T to promote further phase transformation. The volume changes that occurred during $\gamma \rightarrow \alpha'$ phase transformation contribute to plasticity in terms of volumetric transformation strain. Based on the monotonic and cyclic loading tests on a carburized 4320 steel, Neu et al.[24] have classified the γ phase transformation primarily into four regimes depending on the test temperature T (s. Figure 2.4)[24;70].

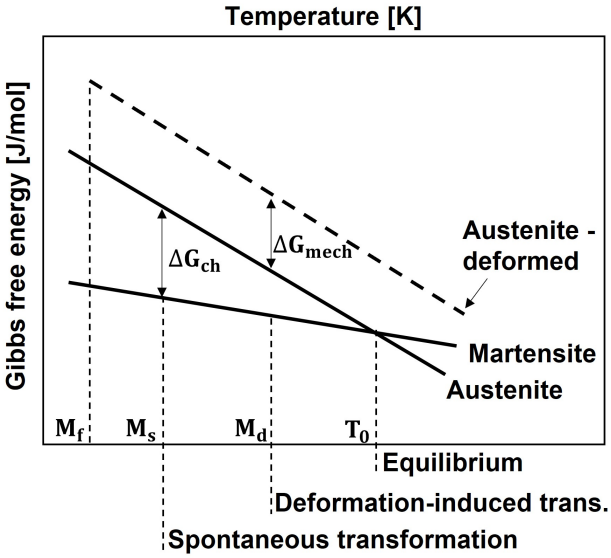

Figure 2.3: Variation of Gibbs free energy for γ and α' phases with temperature[69]

Athermal transformation of the γ phase occurs by cooling the material to subzero temperatures, e.g. cooling in liquid nitrogen or hydrogen. Hence, the free energy ΔG required for athermal transformation is provided through ΔG_{ch}, exclusively. The athermal transformation of the γ phase consider to be a spontaneous transformation, and the rate of transformation remains constant irrespective of the degree of undercooling[70]. Although the γ phase in MSS is metastable at the ambient conditions, the chemical free energy ΔG_{ch} is insufficient for a spontaneous martensitic transformation. However, an additional free energy ΔG_{mech} provided through an externally applied stress σ promotes martensitic transformation known as stress-assisted martensitic transformation (SAMT) at the existing nucleation sites in the parent phase[71]. SAMT is dominant in the temperatures of 298 $K \leq T \leq$ 323 K (s. Figure 2.4)[24]. As the chemical free energy ΔG_{ch} contribution decreases with increasing temperature, ΔG_{mech} contribution must increase with the raise in temperature for further phase transformation. It is observed that the SAMT of γ phase exhausts at the temperature $T = 333\ K$[72]. At elevated temperatures, new nucleation sites for martensitic transformation are generated during the plastic deformation, e.g. intersection of microbands,

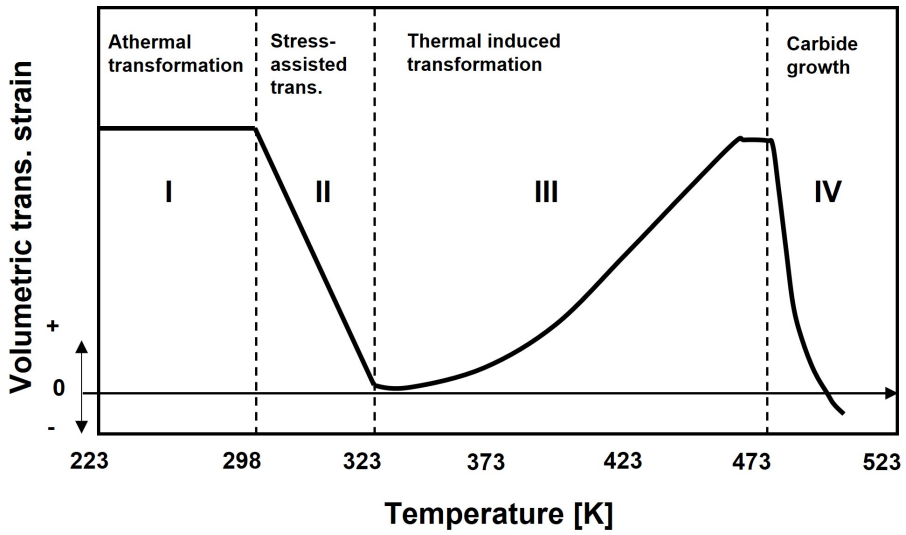

Figure 2.4: Schematic representation of the four regimes of the γ phase transformation in a carburized 4320 steel in the temperatures 223 $K \leq T \leq$ 523 K [24]

and yields to strain-induced martensitic transformation (SIMT) [73;74]. The SAMT and SIMT mechanisms shall be related to the deformation-induced transformation of the γ phase depicted in Figure 2.3.

Thermal-induced transformation (TIT) of γ phase was noticed in a carburized 4320 steel with 35% of γ phase at the temperatures $T \geq 353$ K [24]. The mechanism associated with TIT is similar to the tempering process. At low temperatures, the γ phase decomposes into ferrite and transition carbides, whereas bainitic transformation is preferable at elevated temperatures [24].

The γ phase contributes to plasticity in combination with dislocation glide and mechanical twinning if the SFE is $20-40$ $^{mJ}/_{m^2}$ [75]. TWIP is a prominent deformation mechanism in the steels containing Mn of $18-30$ wt.% along with C, Si, Al, and Cr [76]. The strain hardening in TWIP steels is provided through the formation of deformation twins.

2.4 LTC Investigations on Martensitic Steels

Though plenty of literature is describing the phenomenon of developing martensitic steels with enhanced LTC resistance through heuristic approaches (refer to section 1.2), the research work attempted to address the underlying mechanisms behind LTC in martensitic steels is very limited. The LTC strain ε_{cr} in martensitic steels is confined to the primary stage creep only, i.e. the creep rate $\dot{\varepsilon}_{cr}$ decreases with creep strain ε_{cr} [9–13;24–28] (s. Figure 1.1(b)). Two empirical creep laws, named power law and

logarithmic law[2], are in use to describe the primary stage LTC strain in a material. According to a power law[77;78], the LTC strain

$$\varepsilon_{cr}(t) = m \cdot \left(\frac{t}{t^*}\right)^{m^*} \tag{2.3}$$

where m and m^* being the material parameters, t being time, and t^* being the arbitrary reference time. On the other hand, according to a logarithmic creep law[79;80], the LTC strain

$$\varepsilon_{cr}(t) = \alpha \cdot \ln(\beta \cdot t + 1) \tag{2.4}$$

where $\alpha(\sigma, T)$ and $\beta(\sigma, T)$ are material specific creep parameters.

Oehlert et al.[13] studied the effect of stress σ, loading rate, and loading history on the room temperature creep behavior of martensitic steel grades AISI 4340, 3.5NiCrMoV, and AerMet100. They reported that the stress-dependent room temperature creep strain of these steel grades follows a logarithmic creep law. Liu et al.[10–12] examined the impact of varying small amounts of a secondary phase, i.e. ferrite in the α' matrix, on the room temperature creep behavior of SAE 4340. Samples having the same YS σ_e of $1280 \pm 10\ MPa$ but different ferrite contents of $0 - 4\%$ exhibit a room temperature creep strain that follows a logarithmic creep law. Neu et al.[25] studied the LTC behavior of carburized 4320 steel having a α' matrix with $14 - 35\%$ of γ phase. Their experiments revealed that the stress and temperature-dependent LTC strain obeys a logarithmic creep law. Alfredsson et al.[26] investigated the LTC behavior of the roller-bearing steel grade 100CrMnMo8. They reported that the LTC strain obeys a logarithmic creep law in material with a bainitic matrix. However, the LTC strain in the very same steel grade with a α' matrix follows a power law. It is evident from the above-mentioned LTC investigations that the logarithmic creep law (s. Eq. (2.4)) is rather well suited to describe the primary stage LTC behavior in martensitic steels.

Besides, the stress σ and temperature T dependence of LTC strain, as well as the creep parameters $\alpha(\sigma, T)$ and $\beta(\sigma, T)$ are studied by some of the above-mentioned authors. Oehlert et al.[13] reported that LTC strain ε_{cr}, as well as the creep parameters α and β increase with stress σ. However, the creep parameter α exhibited rather a strong stress σ dependence than the other creep parameter β. The stress σ and temperature T dependence of LTC strain is evident in the studies of Neu et al.[25] on carburized 4320. However, their studies were lacking in examining the stress σ and temperature T dependence of creep parameters. Alfredsson et al.[26] have reported

[2]Later, two LTC mechanism-based models have been developed to describe the logarithmic creep behavior

the stress σ and temperature T dependence of LTC strain in roller-bearing steel grade 100CrMnMo8. However, the stress σ and temperature T dependence of the creep parameters were not covered in their investigations. The LTC studies of Münch et al.[49] on 64SiCrV6 having α' matrix revealed an increase in the LTC strain ε_{cr}, and the creep parameter α with stress σ and temperature T.

The authors mentioned above have unanimously proposed dislocation glide as the underlying mechanism behind the stress σ and temperature T dependent LTC strain ε_{cr} in martensitic steels related to a logarithmic creep law[9–13;24–27]. However, the room temperature creep studies of Liu et al.[10–12] on SAE 4340 with $0-4\%$ ferrite content allowed to take this assumption one step forward. The increase in room temperature creep strain with increasing ferrite content was attributed to the hypothesis of slip localization mainly in the softer ferrite phase[12]. The experiments of Neu et al.[24;70;72] revealed that two deformation modes are contributing to the total strain under constant load: (i) the LTC strain by means of dislocation glide, and (ii) the volumetric transformation strain[3] due to the $\gamma \rightarrow \alpha'$ phase transformation. According to them, γ phase transformation could be aided by either SAMT or TIT depending on the test temperature T (s. Figure 2.4). Alfredsson et al.[26] have considered the occurrence of γ phase transformation under tensile loading in terms of the strength differential effect (SDE)[4] in their LTC models for a good correlation with experimental data.

Although various mechanisms are presumed to be LTC contributors in martensitic steels, i.e. dislocation glide, slip localization, and phase transformation (SAMT and/or TIT), the actual mechanisms behind the primary stage logarithmic creep in martensitic steels are yet to be understood. Furthermore, the LTC rate-controlling mechanisms remain elusive.

2.5 LTC Mechanism-Based Models

Two LTC mechanism-based models, named strain hardening theory (SHT)[82] and exhaustion creep model (ECM)[83–85] were proposed to explicate the logarithmic creep behavior, as well as to justify the creep rate reduction with time. The material is assumed to be single-phase, homogeneous, and isotropic in nature, and the LTC strain is contributed by dislocation glide solely. Thus, the creep rate $\dot{\varepsilon}_{cr}$ shall be expressed

[3] Bhadeshia[81] stated that volumetric transformation due to time-dependent phase transformation obeys a logarithmic creep law.

[4] SDE refers to the display of larger YS σ_e under uni-axial compression load than uni-axial tensile load.

by the Orowan equation

$$\dot{\varepsilon}_{cr} = \rho_m \cdot b \cdot v \tag{2.5}$$

with ρ_m being the mobile dislocation density, b being the Burgers vector, and v being the velocity of mobile dislocation. Consequently, a decrease in creep rate with time could be a result of a decrease in the mobile dislocation density or a decrease in the velocity of mobile dislocation, or a combined result of both [13].

2.5.1 Strain Hardening Theory

A mechanism-based SHT was proposed by Orowan [82] which describes a decrease in LTC rate with time in terms of a decrease in dislocation velocity. It is considered that the activation stress σ required for dislocation glide increases as the LTC strain proceeds due to an increase in back stress exerted by obstacles in the opposite direction to the dislocation motion. Consequently, the dislocation dynamics get affected during LTC deformation. However, the nature of these obstacles has not clearly described by him. Seeger [86] has proposed that the change in dislocation dynamics during deformation resulted from the intersection of mobile dislocations with a kind of sessile dislocations, which are immobile in nature. Alden [18] has argued that the LTC rate reduction is a combined effect of a decrease in dislocation velocity and a reduction in density of mobile dislocations. Like others, the decrease in dislocation velocity was attributed to the increase in back stress during LTC deformation. Besides, he claimed that some of the mobile dislocations were arrested by the dislocation network during LTC, then became immobile in nature. Consequently, the fraction of mobile dislocations gets reduced. Irrespective of their claims on the LTC rate-controlling mechanisms, the authors mentioned above have concluded that the strain hardening approach yields a logarithmic creep law. Kassner et al. [23] have re-examined the SHT, then confirmed the logarithmic creep law similar to

$$\ln \dot{\varepsilon}_{cr} = \ln(\alpha \cdot \beta) - \frac{1}{\alpha} \cdot \varepsilon_{cr} \tag{2.6}$$

with

$$\alpha = \frac{k \cdot T}{h \cdot \nu_e} \quad \text{and} \quad \beta = \frac{c}{\alpha} \cdot \exp\left(-\frac{d}{T}\right) \tag{2.7}$$

with creep parameters $\alpha(T)$ and $\beta(T)$. Here k is the Boltzmann constant, h is the Planck constant, ν_e is the activation volume, c and d are the material constants.

2.5.2 Exhaustion Creep Model

Nabarro[83;84] came up with a distinct approach, i.e. ECM to unveil the LTC rate-controlling mechanisms related to a logarithmic creep law. A year later, the same ECM concept was presented in a simplified manner by Smith[85]. According to them, the material is single-phase, homogeneous, and isotropic in nature and it contains pairs of obstacles and dislocation elements. It is considered that each pair has to be activated so that the dislocation element overcoming the obstacle can move a certain distance to contribute to LTC strain. It is considered that these obstacles have a distribution of inherent activation energies G_i and inherent activation stresses σ_i (s. Figure 2.5). The obstacles possessing activation stress σ_i less than the constant

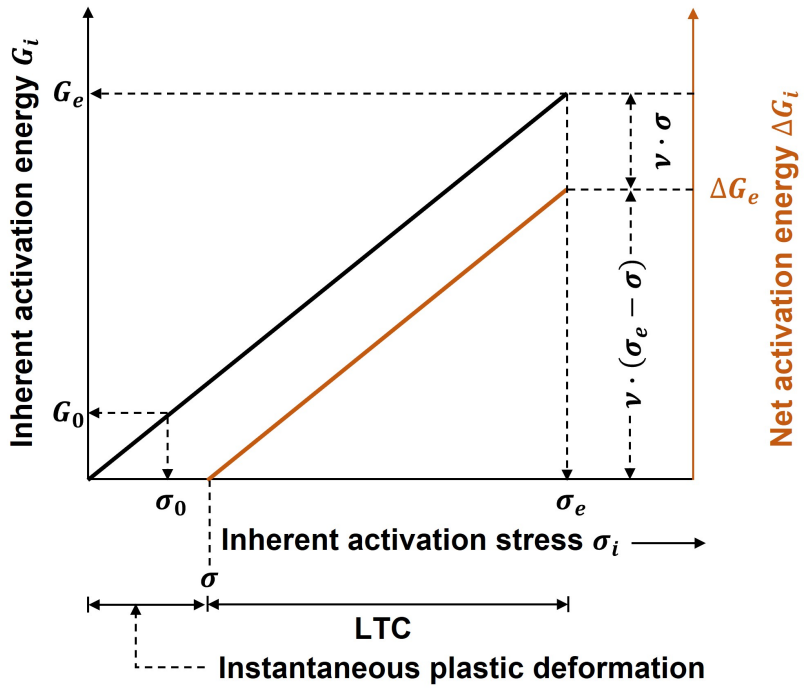

Figure 2.5: Classification of obstacles based on the inherent activation energy G_i and inherent activation stress σ_i

applied stress σ, i.e. $\sigma_i < \sigma$, are activated spontaneously and contributed to instantaneous plastic strain in LTC testing. To justify the transient nature of LTC strain, these obstacles are assumed to be exhausted immediately, once the dislocation element successfully surmounts the obstacle[87]. Since the dislocation elements must overcome the obstacles with progressively larger activation energies as the LTC strain proceed, the LTC rate diminishes with time due to the exhaustion of numerous obstacles with small activation energies[83–85;87]. However, their ECM version discussed neither the nature of these obstacles nor the mechanism behind the progressive exhaustion of them clearly. Welch et al.[88] have re-examined the ECM, then they claimed that the LTC rate diminishes due to exhaustion of mobile dislocations instead of obstacles by dislo-

cation intersection mechanism. Irrespective of their claims on the LTC rate-controlling mechanisms, the authors mentioned above have stated that the ECM approach led to a logarithmic creep law

$$\varepsilon_{cr}(t) = \alpha \cdot \ln(\beta \cdot t) \tag{2.8}$$

with

$$\alpha = e \cdot T \quad \text{and} \quad \beta = \text{constant} \tag{2.9}$$

where $\alpha(T)$, β are material specific creep parameters, and e is a material constant. However, Cottrell[89] claimed in his latest work that the ECM is incomplete, and doesn't yield to a logarithmic creep law once it is completed.

2.5.3 Shortcomings of LTC Mechanism-Based Models

Martensitic steels exhibit the stress σ and temperature T dependence of LTC strain related to a logarithmic creep law. Furthermore, the experimentally derived creep parameters also exhibit significant stress σ and temperature T dependency (refer to section 2.4). As an example, the experimentally derived creep parameters α and β of martensitic steel grades AISI 4340, AerMet100, and 3.5NiCrMoV were extracted from the work of Oehlert et al.[13], and presented here in Figure 2.6.

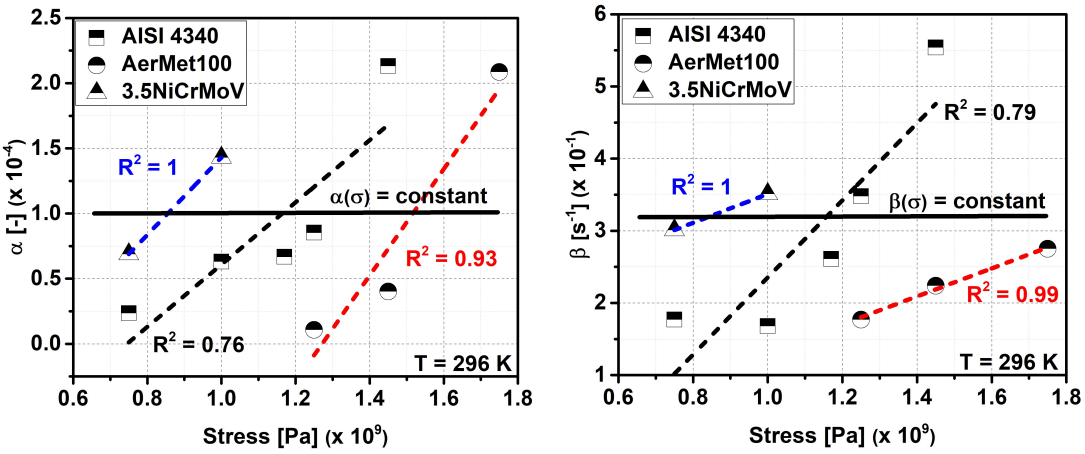

(a) (b)

Figure 2.6: Stress dependence of (a) creep parameter α, (b) creep parameter β at constant temperature $T = 296\ K$[13]

Though the SHT approach yields a logarithmic creep law (s. Eq. (2.6)), it conceives the creep parameters $\alpha(T)$ and $\beta(T)$ as independent of stress σ (s. Eq. (2.7)). Thus, the SHT is incapable of describing the stress σ dependency of the experimentally derived creep parameters shown in Figure 2.6. Neu et al.[25] attempted to incorporate the stress σ dependency of the creep parameter α in their kinetic model of logarithmic creep in terms of the deviatoric stress. However, their analyses were not in line

with the experimentally derived stress σ and temperature T dependency of the creep parameters. Alfredsson et al.[26] attempted to extend the SHT by combining a logarithmic creep model with the SDE effect in order to well describe the LTC behavior of high-strength roller-bearing steel. However, their approach was purely related to the mechanics of the material rather than a mechanism-based approach addressing the LTC rate-controlling mechanisms. Furthermore, their work was lacking in verifying the extended SHT in terms of stress σ and temperature T dependence of creep parameters. Since a mechanism-based model ought to describe the stress σ and temperature T dependence of creep parameters correctly, still there is a necessity for the development of the SHT. Subsequently, the modified SHT needs to be verified and validated at the example of an MSS to disclose the LTC rate-controlling mechanisms in the respective steel grade.

Nabarro[83;84] and Smith[85] stated that the ECM approach yields a logarithmic creep law (s. Eq. (2.8)). Therefore, the above-mentioned shortcomings of SHT in describing the stress σ dependence of creep parameters shall be extended to the ECM as well. Besides, the ECM is incomplete and doesn't yield to a logarithmic creep law once it is completed as stated by Cottrell[89] in his latest work. Thus, the existing version of ECM is unqualified in describing the LTC behavior of martensitic steels. Hence, there is a necessity to rework the ECM from scratch through a mechanism-based approach to justify the stress σ and temperature T dependence of LTC strain, as well as the creep parameters. Subsequently, the reworked ECM needs to be verified and validated at the example of an MSS to disclose the LTC rate-controlling mechanisms in the respective steel grade.

Chapter 3

A Roadmap to Achieve the Research Objectives

3.1 Research Objectives

Though various mechanisms are presumed to be LTC contributors in martensitic steels, the actual mechanisms behind LTC in an MSS are yet to be understood. Besides, the LTC rate-controlling mechanisms remain elusive. Therefore, the main focus of the current research is to disclose the LTC rate-controlling mechanisms in an MSS. To accomplish the target, the main objectives of the considered research approach are as follows: (1) develop the LTC mechanism-based models, i.e. SHT and ECM to overcome their respective shortcomings described in section 2.5.3, (2) verify and validate the developed LTC mechanism-based models, i.e. modified SHT and reworked ECM, at the example of an MSS, and (3) propose and validate the experimental-based hypothesis of LTC rate-controlling mechanisms in the investigated MSS.

3.2 A Roadmap to Achieve the Research Objectives

A research approach of combined analysis by means of (i) an LTC mechanism-based model, and (ii) mechanical testing followed by advanced microstructural characterization prior to and post LTC is considered to disclose the LTC rate-controlling mechanisms in an MSS. A roadmap of the research approach to disclosing the LTC rate-controlling mechanisms in an MSS is shown in Figure 3.1.

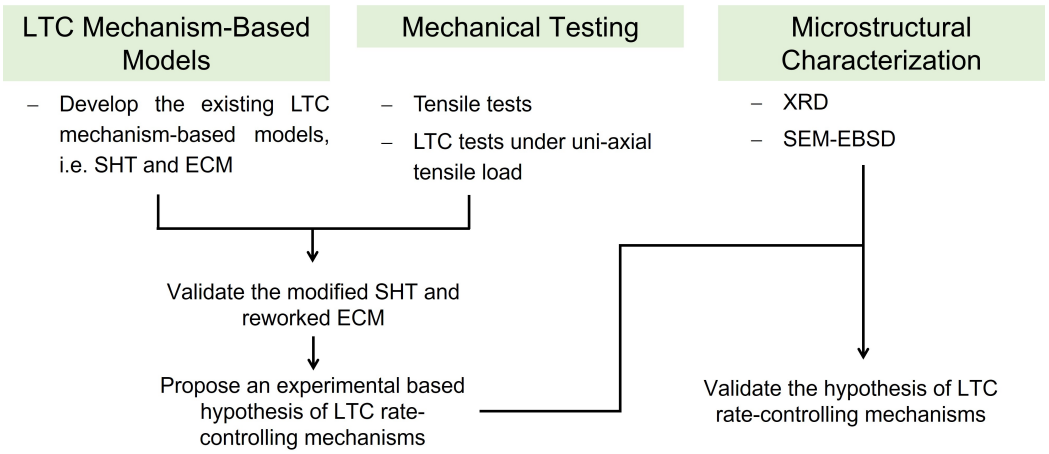

Figure 3.1: A roadmap of the research approach to disclosing the LTC rate-controlling mechanisms in an MSS

Research Objective #1: Develop the Low Temperature Creep Mechanism-Based Models

An LTC mechanism-based model ought to describe the stress σ and temperature T dependence of LTC strain, as well as the creep parameters correctly. However, the major drawback of the existing LTC mechanism-based models, i.e. SHT and ECM is their inability to describe the stress σ and temperature T dependence of creep parameters. It is noticed that the earlier generation authors have considered the obstacles possessing inherent activation stresses σ_i in the range of $0 - \infty$. Furthermore, the obstacle distribution function was assumed to be a slowly varying function of applied stress σ. These two considerations led to the handicapped SHT and ECM. It can be overcome by restricting the obstacles having activation stresses σ_i up to YS σ_e, and by introducing a reasonable stress σ dependent obstacle distribution function. Furthermore, the incomplete version of ECM shall be completed without any approximations by means of today's resources. The details of developing the SHT and ECM are described comprehensively in Chapter 4.

Research Objective #2: Verify and Validate the Developed Low Temperature Creep Mechanism-Based Models

The developed LTC mechanism-based models, i.e. modified SHT and reworked ECM are verified and validated in a two-stage process at the example of IQT SAE 9254. In the first stage of verification, the ability of the developed models to describe the stress σ and temperature T dependence of LTC strain is verified by the best fitting of the LTC strain of IQT SAE 9254 with their respective creep laws. Subsequently, the

individual creep parameters are derived from the best fitting. In the second stage of verification, the derived creep parameters ought to represent the stress σ and temperature T dependency in terms of their respective creep laws, correctly. The unqualified model shall be ruled out at this stage for further validation. As mentioned in the section 2.5, the LTC models are developed based on the consideration that LTC strain is contributed by dislocation glide. Hence, the magnitude of the derived activation volume ν_e and YS σ_e from the second stage fitting of creep parameters would be supportive in the process of validating the developed LTC mechanism-based models. The independent verification followed by validation of the modified SHT and reworked ECM at the example of IQT SAE 9254 are presented in Chapter 6.

Research Objective #3: Propose and Validate the Hypothesis of LTC Rate-Controlling Mechanisms in an MSS

Successful validation of the reworked ECM at the example of IQT SAE 9254 followed by microstructural characterization prior to and post LTC with the aid of XRD are supported in constructing an experimental-based hypothesis of LTC rate-controlling mechanisms in IQT SAE 9254 (refer to Chapter 6).

However, it is challenging to validate the hypothesis at the example of IQT SAE 9254 that contains a rather low volume fraction of γ phase (8.9%) in the form of nano-islands (s. Figure 5.11(a)). Consequently, the author feels increasing the γ phase would be convenient to validate the proposed hypothesis of the LTC rate-controlling mechanisms in SAE 9254. Hence, the martempering technology [90] (refer to section 5.2.2) is considered to increase the volume fraction of γ phase in the very same SAE 9254 steel grade. The microstructural changes due to LTC, i.e. the γ phase fraction, and dislocation density determined by XRD, as well as Kernel-Average-Misorientation (KAM), and respective phase maps obtained from SEM coupled with electron back-scattered diffraction (EBSD) shall provide firm support to validate the proposed hypothesis of the LTC rate-controlling mechanisms in SAE 9254 (refer to Chapter 7 and Chapter 8).

Chapter 4

Modification of Low Temperature Creep Mechanism-Based Models

The purpose of this chapter is to review the existing LTC mechanism-based models, i.e. SHT and ECM, followed by reworking them to overcome their respective drawbacks postulated in section 2.5.3.

It is generally assumed that LTC in martensitic steels is sustained by a dislocation glide mechanism analogous to plastic deformation. However, in contrast to plastic deformation, the uni-axial stress σ during LTC is significantly smaller than the YS σ_e of the material. A punctiform obstacle or spatial residual stress may constrain the mobility of each linear mobile dislocation element under a load σ. Considering only the interaction with an obstacle, each pair, consisting of a mobile dislocation element and an obstacle, respectively, has to become activated, so that the dislocation element can move for a certain distance before it gets arrested by another obstacle again. In a rather simple approach, the considered material is homogeneous, and it possesses a specific number P of such pairs per volume. The unit volume V, which contains only one pair, then reads

$$P \cdot V = 1 \Rightarrow V = \frac{1}{P}. \tag{4.1}$$

Figure 4.1 shows such a dislocation element that is arrested by an obstacle in its unit volume V. With the average length l of such a mobile dislocation element, the density ρ_m of mobile dislocations is accordingly defined by

$$\rho_m = \frac{l}{V} = l \cdot P \tag{4.2}$$

For the sake of simplicity, it is assumed that the specific number P of pairs per volume and the mobile dislocation density ρ_m are slowly varying functions in time t.

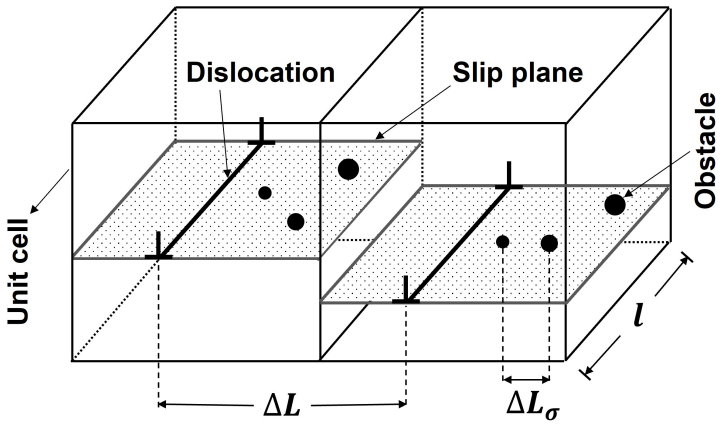

Figure 4.1: Schematic representation of dislocation pairs in slip plane of adjacent unit cells

4.1 The Obstacle Distribution Function

The nature of an obstacle, that prevents the movement of the dislocation element, is defined by its inherent activation energy G_i, and activation volume ν_i. Thermal activation of the pair of a dislocation element and an obstacle, respectively, under the stress σ at a temperature T is controlled by the net activation energy ΔG_i

$$\Delta G_i = G_i - \nu_i \cdot \sigma = \nu_i \cdot \Delta\sigma_i \tag{4.3}$$

where $\sigma_i = {}^{G_i}/_{\nu_i}$ denotes the inherent activation stress and $\Delta\sigma_i = \sigma_i - \sigma$ is the net activation stress, respectively (s. Figure 2.5). The maximum inherent activation energy G_e of obstacles manifests itself at the YS σ_e, i.e.

$$G_e = \nu_e \cdot \sigma_e \tag{4.4}$$

Hence, the specific activation energy g_i and the specific net activation energy Δg_i are defined as

$$g_i = \frac{G_i}{G_e} \quad \text{and} \quad \Delta g_i = \frac{\Delta G_i}{G_e}. \tag{4.5}$$

with $0 \leq g_i < 1$. It is assumed here that the activation volume ν_i is either ν_e, i.e. a constant, or a monotonically increasing function of g_i. i.e.

$$\nu_i = \nu(g_i) \quad \text{and} \quad \frac{d\nu(g_i)}{g_i} \geq 0 \tag{4.6}$$

so that $0 \leq \Delta g_i < {}^{(\sigma_e - \sigma)}/_{\sigma_e}$. Besides, the considered pair of a dislocation element and an obstacle, the unit volume V contains further obstacles in the path of the activated mobile dislocation element. The collectivity of these obstacles within this path, i.e.

in the specific glide plane, is defined by the total number N of obstacles per unit volume V

$$N = \int_0^1 N(g_i) \cdot dg_i \tag{4.7}$$

with $N(g_i) \cdot dg_i$ being the relative number of obstacles per unit volume V having a specific inherent activation energy g_i. Then the normalized obstacle distribution function $\phi(g_i)\ dg_i$ reads

$$\phi(g_i)dg_i = \frac{N(g_i)}{N} \cdot dg_i \Rightarrow \int_0^1 \phi(g_i) \cdot dg_i = 1. \tag{4.8}$$

Under a uni-axial stress σ, the total effective number N_σ of obstacles is smaller than N and it reads as a function of the specific net activation energy Δg_i

$$N_\sigma = \int_0^{\frac{\sigma_e - \sigma}{\sigma_e}} N_\sigma(\Delta g_i) \cdot d(\Delta g_i) < N \quad \text{with} \quad N_\sigma(\Delta g_i) = N(g_i) \tag{4.9}$$

Then the normalized effective obstacle distribution function $\phi_\sigma(\Delta g_i) \cdot d(\Delta g_i)$ reads

$$\begin{aligned} \phi_\sigma(\Delta g_i) \cdot d(\Delta g_i) &= \frac{N_\sigma(\Delta g_i) \cdot d(\Delta g_i)}{N_\sigma} \\ \Rightarrow \int_0^{\frac{\sigma_e - \sigma}{\sigma_e}} \phi_\sigma(\Delta g_i) \cdot d(\Delta g_i) &= 1 \end{aligned} \tag{4.10}$$

For the sake of comparability between both approaches to be considered, here it is assumed that (i) the obstacles are distributed homogeneously between the limits of specific activation energy g_i, i.e. 0 and 1, and (ii) the obstacles have a uniform activation volume $\nu_i = \nu_e$ leading to

$$\phi_\sigma = \frac{\sigma_e}{\sigma_e - \sigma} \quad \text{and} \quad N_\sigma = N \cdot \frac{\sigma_e - \sigma}{\sigma_e}. \tag{4.11}$$

4.2 The Strain Rate Equation

Irrespective of the nature of the specific LTC model or theory, a function $q(\Delta g_i, t)$ specifies the specific number $P_i^a(t)$ of pairs per unit volume V of a mobile dislocation element and an obstacle of the specific net activation energy Δg_i, which have been previously activated, whereby

$$P_i^a(t) = P^a(\Delta g_i, t) = P \cdot q(\Delta g_i, t) \tag{4.12}$$

This specific number $P^a(t)$ of pairs as well as the density ρ_m^a of previously activated mobile dislocations then read

$$P^a(t) = P \cdot q(t) \quad \text{and} \quad \rho_m^a(t) = \rho_m \cdot q(t) \tag{4.13}$$

with the time dependent probability function $q(t)$ for the activation of pairs

$$q(t) = \int_0^{\frac{\sigma_e - \sigma}{\sigma_e}} q(\Delta g_i, t) \cdot \phi_\sigma(\Delta g_i) \cdot d(\Delta g_i) \tag{4.14}$$

For the sake of simplicity, it is assumed that mobile dislocation elements only interact with punctiform obstacles and explicitly not with other linear mobile dislocation elements. After its activation, a dislocation element is able to move for an average, effective distance ΔL_σ before it is getting arrested by the next obstacle (s. Figure 4.1). This average, effective distance ΔL_σ is given by

$$\Delta L_\sigma = \frac{\Delta L}{N_\sigma \cdot V} \tag{4.15}$$

with ΔL being the average length of the distance between each two pairs in adjacent unit cells, that is projected into the active glide plane. The LTC strain ε_{cr} of a specimen, which results from the activation of pairs and the motion of mobile dislocation elements, is defined by an Orowan-type equation

$$\varepsilon_{cr}(\sigma, t) = M \cdot b \cdot \Delta L_\sigma \cdot \rho_m^a(t) = \frac{M \cdot b \cdot \Delta L}{N_\sigma \cdot V} \cdot \rho_m^a(t) \tag{4.16}$$

where M denotes the Taylor factor and b is Burgers vetor. The strain rate $\dot{\varepsilon}_{cr}$ of LTC finally becomes

$$\dot{\varepsilon}_{cr}(\sigma, t) = \frac{M \cdot b \cdot \Delta L}{N_\sigma \cdot V} \cdot \dot{\rho}_m^a(t) \tag{4.17}$$

with

$$\dot{\rho}_m^a(t) = \rho_m \cdot \dot{q}(t) \tag{4.18}$$

4.3 The Thermal Activation of Pairs

In a state of thermodynamic equilibrium, only a small fraction $\varphi(\Delta g_i)$ of dislocation elements is able to surmount an obstacle of magnitude Δg_i by thermal activation according to the Maxwell-Boltzmann statistics, i.e.

$$\varphi(\Delta g_i) = \exp\left(-\frac{G_e \cdot \Delta g_i}{k \cdot T}\right). \tag{4.19}$$

In a more elementary description, a dislocation element makes its attempts to surmount the obstacle at a vibration frequency f_0. Then the frequency f_w with which a dislocation element is surmounting an obstacle becomes

$$f_w = t_w^{-1} = f_0 \cdot \varphi(\Delta g_i) = f_0 \cdot \exp\left(-\frac{G_e \cdot \Delta g_i}{k \cdot T}\right) \tag{4.20}$$

with the average waiting time t_w of dislocation in front of the obstacle.

4.4 Modified Strain Hardening Theory

According to Kassner[23], the probability $q(\Delta g_i, t)$ of the activation of a pair, i.e. a dislocation element surmounting one obstacle, is defined by the product of time t and a frequency f_w

$$q(\Delta g_i, t) = f_w \cdot t \quad \text{with} \quad f_w = f_0 \cdot \exp\left(-\frac{G_e \cdot \Delta g_i}{k \cdot T}\right) \tag{4.21}$$

with f_0 being a vibration frequency of a dislocation element that attempts to surmount an obstacle. The hypothesis implies that the effective specific net activation energy $\Delta g_{eff,i}$ gets increased during LTC by internal opposing stress σ_G that is proportional to the LTC strain ε_{cr}. Hence, the specific net activation energy Δg_i becomes an effective specific net activation energy $\Delta g_{eff,i}$

$$\Delta g_{eff,i} = \Delta g_i + \frac{\nu_e \cdot \sigma_G}{G_e} = \Delta g_i + \frac{\nu_e \cdot h}{G_e} \cdot \varepsilon_{cr} \tag{4.22}$$

with h being the strain-hardening coefficient. The rate $\dot{q}(t)$ of activation becomes

$$\dot{q}(t) = \phi_\sigma \cdot f_0 \cdot \frac{k \cdot T}{G_e} \cdot \left[1 - \exp\left(-\frac{G_e}{k \cdot T} \cdot \frac{\sigma_e - \sigma}{\sigma_e}\right)\right] \cdot \exp\left(-\frac{\nu_e \cdot h \cdot \varepsilon_{cr}}{k \cdot T}\right). \tag{4.23}$$

leading to a differential equation describing LTC like

$$\ln \dot{\varepsilon}_{cr} = \delta^S - \frac{1}{\alpha^S} \cdot \varepsilon_{cr} \tag{4.24}$$

where the pair of creep parameters α^S and δ^S are

$$\alpha^S = \frac{k \cdot T}{h \cdot \nu_e} \quad \text{and} \quad \delta^S = \ln\left(\alpha^S \cdot \beta^S\right) \tag{4.25}$$

with

$$\beta^S = \frac{D}{\alpha^S} \cdot T \cdot \frac{\sigma_e}{(\sigma_e - \sigma)^2} \cdot \left[1 - \exp\left(-\frac{G_e}{k \cdot T} \cdot \frac{\sigma_e - \sigma}{\sigma_e}\right)\right] \tag{4.26}$$

with D being a material constant. With the initial value condition $\varepsilon_{cr}|_{t=0} = 0$, the LTC strain ε_{cr} according to modified SHT leads to a logarithmic creep law

$$\varepsilon_{cr} = \alpha^S \cdot \left(\beta^S \cdot t + 1\right). \tag{4.27}$$

4.5 Reworked Exhaustion Creep Model

The concept of an ECM was proposed by Mott and Nabarro[83;84] in terms of a net activation stresses $\Delta\sigma_i$ of the obstacles that is here reworked according to Eq. (4.3) to a model based on the specific net activation energy Δg_i. According to them, a material contains a total specific number $N_\sigma\left(\Delta g_i\right)$ of obstacles per unit volume having a specific net activation energy Δg_i that can be surmounted only once by a dislocation element. However, the author considered here temperature T dependent multiple activations $n(T)$ of a dislocation element prior to getting exhausted. Furthermore, a homogeneous distribution $N(g_i) = N$ of obstacles having inherent activation energies in a range $0 < g_i < 1$ is considered[83]. According to Nabarro[83;84], Smith[85], and Welch[88], the probability function $p\left(\Delta g_i, t\right)$ of the survival of one pair per unit volume V for a time t without activation reads

$$p\left(\Delta g_i, t\right) = \exp\left[-f_0 \cdot \exp\left(-\frac{G_e \cdot \Delta g_i}{k \cdot T}\right) \cdot t\right]. \tag{4.28}$$

The rate of activation $\dot{q}(t)$ then becomes

$$\dot{q}(t) = -\phi_\sigma \cdot \int_0^{\frac{\sigma_e - \sigma}{\sigma_e}} \dot{p}\left(\Delta g_i, t\right) \cdot d\left(\Delta g_i\right) \tag{4.29}$$

and the LTC strain rate $\dot{\varepsilon}_{cr}$ becomes with Eq. (4.14) and Eq. (4.17)

$$\dot{\varepsilon}_{cr} = -\frac{M \cdot b \cdot \Delta L \cdot \phi_\sigma}{N_\sigma \cdot V} \cdot \rho_m \cdot \int_0^{\frac{\sigma_e - \sigma}{\sigma_e}} \dot{p}\left(\Delta g_i, t\right) \cdot d\left(\Delta g_i\right). \tag{4.30}$$

Further simplification led to the LTC strain rate $\dot{\varepsilon}_{cr}$ becomes

$$\dot{\varepsilon}_{cr} = \frac{\alpha^E}{t} \cdot \left[\exp\left(-f_1^* \cdot t\right) - \exp\left(-f_0^* \cdot t\right)\right] \tag{4.31}$$

With the initial value condition $\varepsilon_{cr}|_{t=0} = 0$, the LTC strain $\varepsilon_{cr}(t)$ according to the reworked ECM exhibits a non-logarithmic creep behavior shown as

$$\varepsilon_{cr}(t) = \alpha^E \cdot \left[\ln\left(\frac{f_0^*}{f_1^*}\right) + E_1\left(f_0^* \cdot t\right) - E_1\left(f_1^* \cdot t\right)\right] \tag{4.32}$$

with $E_1(x)$ being an exponential integral function [91] and

$$\alpha^E(\sigma, T) = C \cdot \frac{\sigma_e}{(\sigma_e - \sigma)^2} \cdot T \cdot n(T) \tag{4.33}$$

$$f_0^*(T) = \frac{f_0}{n(T)}, \quad \text{and} \quad f_1^*(\sigma, T) = f_0^*(T) \cdot \exp\left[-\frac{\nu_e \cdot (\sigma_e - \sigma)}{k \cdot T}\right] \tag{4.34}$$

$$n(T) = \frac{f_0}{f_0^*(T)}, \quad \text{and} \quad \frac{f_1^*(\sigma, T)}{f_0^*(T)} = \exp\left[-\frac{\nu_e \cdot (\sigma_e - \sigma)}{k \cdot T}\right] \tag{4.35}$$

with C being a materials constant, ν_e being the mean activation volume of the here-considered obstacles, and k being the Boltzmann constant. The creep parameters α^E, f_0^*, and f_1^* are functions of stress σ and temperature T with f_0 being a frequency with which the dislocation attempts to overcome an obstacle.

Chapter 5

Material, Heat Treatment, and Methods

5.1 Material

SAE 9254 (s. Table 5.1) wire rods of 12 mm diameter are supplied in hot rolled condition by JSW Steel Ltd. Salem Works, India, and Saarstahl AG, Germany. The UTS and YS σ_e of as-received wire rods are determined by the University of Hyderabad as 927 MPa and 474 MPa, respectively, which can be attributed to the microstructure containing softer phases, i.e. pearlite and ferrite[41]. The hot rolled wire rods are IQT processed (refer to section 5.2.1) to achieve the desired mechanical properties according to the industrial requirements. Martempering heat treatment (refer to section 5.2.2) is also adopted to tailor the microstructure to conveniently validate the proposed hypothesis of LTC rate-controlling mechanisms in SAE 9254.

Table 5.1: Chemical composition of SAE 9254 (in wt.%) provided by the material suppliers

C	Si	Mn	Cr	Fe
0.53	1.32	0.69	0.71	Bal.

5.2 Heat Treatment

The superior mechanical properties of MSS are achieved through the QT process, and the microstructure evolution during the QT process is described in section 2.2. In industrial practice, the QT process is performed by means of either inductive treatment[2] and/or conventional furnace treatment[31] or a combination of both.

5.2.1 Inductively Quenching and Tempering

In the current research, the SAE 9254 hot rolled wire rods supplied by Saarstahl AG, Germany, are IQT processed at Mubea Fahrwerksfedern GmbH, Weißensee, Germany. Figure 5.1 shows the schematic representation of the IQT process adopted in industrial practice. The steel wire rod, pulled from a wire coil by means of feeding rolls, is passed through a pinch of rolls to get the straightened configuration. Subsequently, the wire rod is fed to the induction heating coil to get austenitized at 1223 K followed by quenching to ambient temperature T. Here, water spray maintained at room temperature T was used as a quenching media. Thereupon, the quenched wire rods once again passed through the induction heating coil for tempering at 723 K followed by cooling to ambient temperature T by means of water spray.

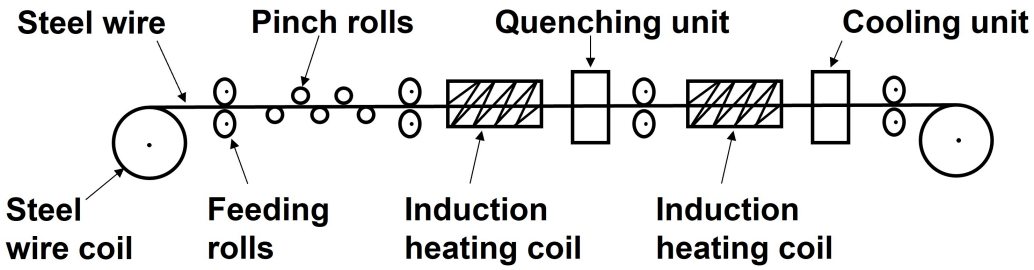

Figure 5.1: Schematic representation of the IQT process adopted in industrial practice[8]

5.2.2 Martempering

The Martempering technology[90] is considered to increase the volume fraction of γ phase in the very same SAE 9254 steel grade. The time-temperature-transformation (TTT) diagram for the considered steel grade has been generated with the aid of JMatPro® software to assess the martensitic start (M_s) and finish (M_f) temperatures (s. Figure 5.2(a)). Subsequently, the hot rolled wire rods supplied by JSW Steel Ltd. Salem Works, India, are martempered in three separate batches at the University of Hyderabad, India, as shown in Figure 5.2(b). A muffle furnace Nabertherm L3/12 was used to austenize the samples at 1183 K for 1200 s followed by quenching in an oil bath maintained at 523 K for 60 s, which is slightly below the M_s temperature. Thereupon, these samples were air-cooled to the ambient temperature T. In the second stage of heating, the samples were heated to 583 K for 1500 s followed by oil quenching to the ambient temperature T.

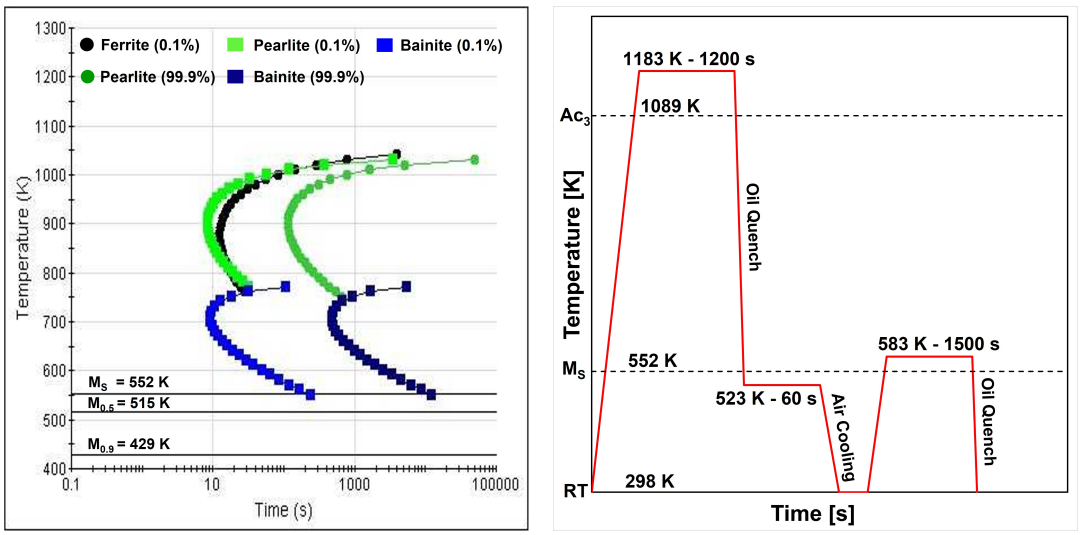

(a) (b)

Figure 5.2: (a) TTT diagram of SAE 9254 generated by JMatPro® software, (b) Schematic representation of the martempering heat treatment

5.3 Fabrication of the Specimens

Specimens for tensile and LTC testings were fabricated from both the IQT and martempered SAE 9254 wire rods along the rolling direction with a gauge length $l^* = 25\ mm$ and gauge diameter $d = 4\ mm$ as shown in Figure 5.3. The specimens were fabricated by means of lathe machine cutting maintained the depth of cut as 0.1 mm increments at 2000 rpm. The entire fabrication of specimens was processed under cooling to avoid the unwanted microstructural changes in the specimens caused by heat input in the processing zone. The specimen geometry was designed for accurate measurements of small-scale LTC strain. The considered conical head avoids slipping the specimen while testing.

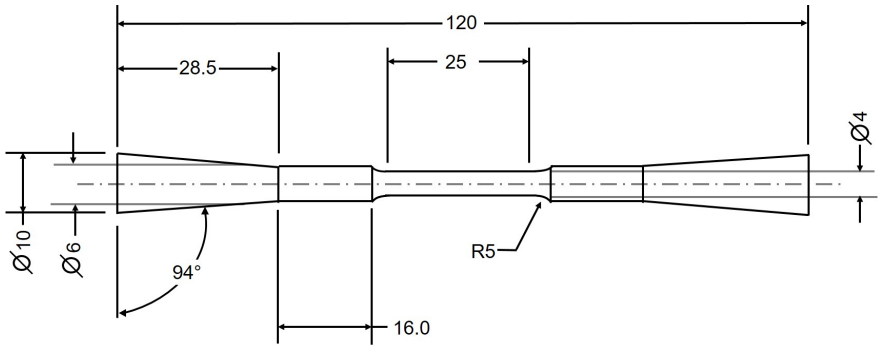

Figure 5.3: Tensile and LTC specimen dimensions in mm

5.4 Analysis and Testing Methods

5.4.1 Tensile Test

The tensile tests were performed by means of the universal testing system Shimadzu AG-X equipped with a 100 kN load cell. The system is used in combination with a thermostatic chamber (s. Figure 5.4(a)). Strain measurements were realized by using the high-resolution digital image correlation (DIC) system Limess Q400 with two cameras for 3D-evaluation of each specimen's surface (s. Figure 5.4(b)). A DIC speckle pattern was applied by priming the specimen's surface with a special heat-resistant black paint. Subsequently, white paint in the form of randomly distributed dots was applied. Pictures for correlation were taken time-triggered every 0.5 s during tensile testing.

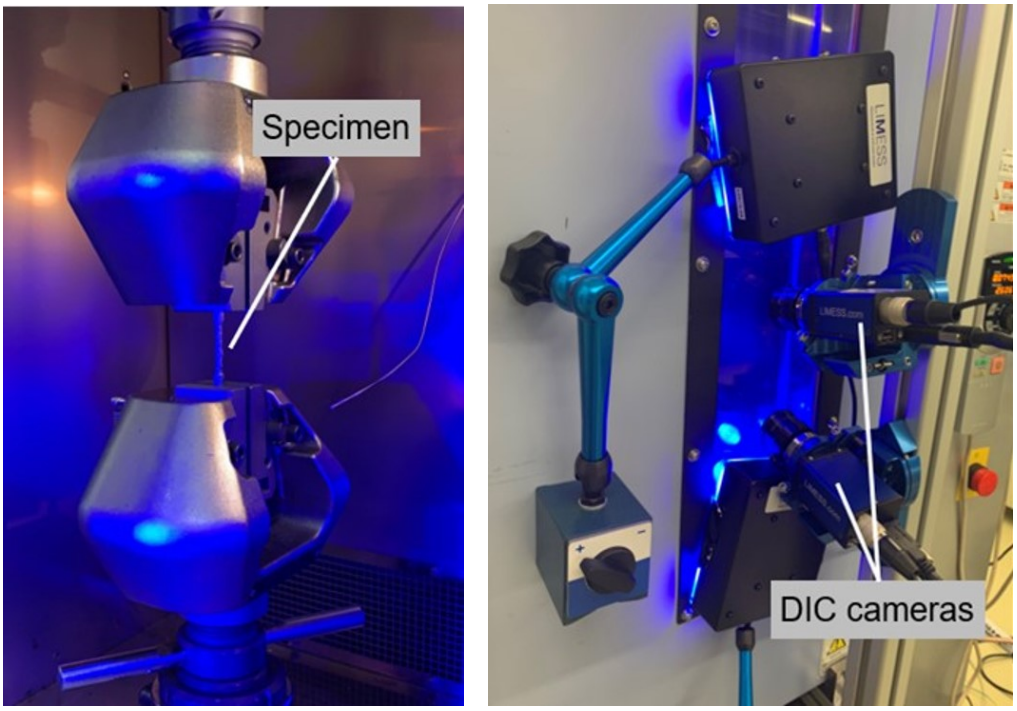

(a) **(b)**

Figure 5.4: (a) Specimen clamped inside, (b) DIC setup outside, of the thermostatic chamber

The UTS and YS σ_e of IQT and martempered SAE 9254 were determined in the temperatures 298 $K \leq T \leq 353$ K at a constant strain rate of $2.5 \cdot 10^{-4}$ s^{-1}. Three specimens were tested at each condition, respectively. Figure 5.5 shows an example of a stress-strain curve of SAE 9254. The mechanical properties, i.e. UTS, YS σ_e, and RoA are determined according to their definitions[14]. Figure 5.5 inset shows the determination of 0.2% offset YS σ_e from the stress-strain curve.

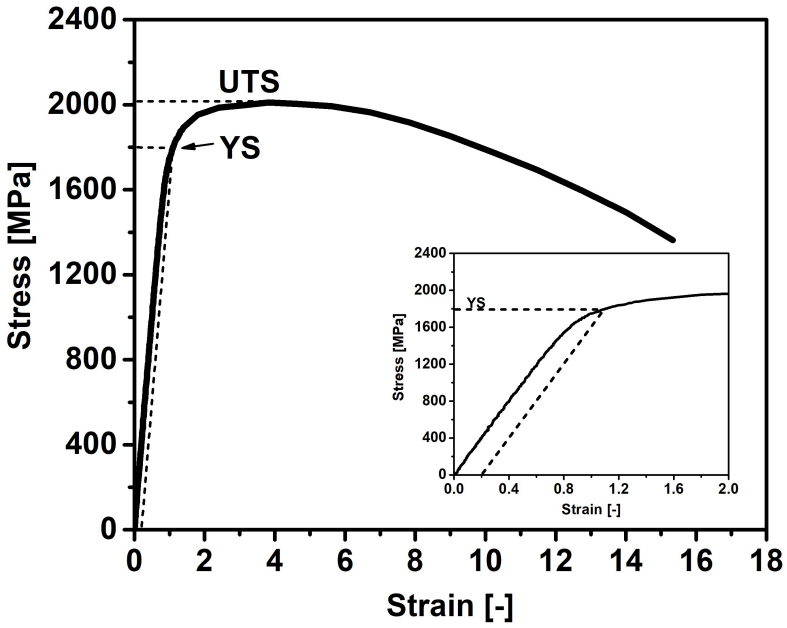

Figure 5.5: Stress-strain diagram of SAE 9254 steel; Inset: Determination of 0.2% offset YS σ_e

5.4.2 Low Temperature Creep Test

The same specimen geometry and test setup (s. Figure 5.3 and Figure 5.4) are considered to study the stress σ and temperature T dependence of LTC in SAE 9254. Pictures for correlation were taken time-triggered every 5 s for LTC tests. LTC strain $\varepsilon_{cr}(t)$ was measured by using the evaluation software Istra 4D, which allows applying a virtual gauge line element on the specimen in longitudinal or test load direction.

LTC deformation behavior of both IQT SAE 9254 and martempered SAE 9254 are studied in the temperatures 298 $K \leq T \leq 353$ K for a duration of 1 hr at each condition. The stress σ for LTC testing must be less than the YS σ_e of the material, i.e. $\sigma < \sigma_e$. Hence, the stress σ dependent LTC behavior of IQT SAE 9254 was studied in the stresses 1071 $MPa \leq \sigma \leq 1634$ MPa, whereas the stress σ dependent LTC behavior of martempered SAE 9254 was studied in the stresses 421 $MPa \leq \sigma \leq 632$ MPa. Three specimens were tested at each condition. The loading process during the LTC test happens at a constant rate of 500 N/s until achieving the required creep load σ, then remains constant. Figure 1.1(a) shows the schematic representation of the loading process in LTC testing.

5.4.3 Determination of Prior Austenite Grain size

For PAG size determination, the samples are sectioned from the IQT and martempered SAE 9254 wire rods. Subsequently, the samples were ground with silicon carbide abrasive papers of grit size up to 1200, then polished with diamond paste having particle sizes $6, 3$, and $1\ \mu m$. The PAG boundaries in IQT steel are revealed by etching the freshly polished surface with Bechet-Beaujard etchant for $25 - 30\ min$ at ambient conditions. The PAG boundaries in martempered steel are revealed by etching the freshly polished surface with 3% Nital for 120 s at ambient conditions. The average PAG size was determined by an ASTM standard linear intercept method[92].

5.4.4 Phase Analysis by X-ray Diffraction

The volume fraction of γ phase and dislocation densities are quantified by means of XRD. The samples for XRD prior to LTC are sectioned from the IQT and martempered wire rods, whereas the samples for XRD post LTC are sectioned from the middle of the gauge sections of LTC specimens. Subsequently, the samples were ground with silicon carbide abrasive papers of grit size up to 1200, then polished with the diamond paste of up to $1\ \mu m$.

An empyrean Panalytical X-ray diffractometer operated at 40 kV and 30 mA with $Cr - K\alpha$ monochromatic source and $V\ k\beta$ filter having 0.02 thickness was used to record the pattern in $64° \leq 2\theta \leq 162°$ in a continuous scanning mode with a step size of 0.039°. The instrumental broadening was corrected using standard LaB_6 sample[93]. The phase identification and crystal structure determination of the recorded XRD patterns is carried out according to the procedure given by B. D. Cullity[94]. Figure 5.6 shows an example of the XRD pattern of SAE 9254 steel grade. The {110}, {200}, {211} peaks and {111}, {200}, {220} peaks of the α' phase and γ phase are indexed, respectively. The changes in dislocation density, as well as in volume fraction of the γ phase due to LTC deformation are determined by considering the full width at half maximum (FWHM) and area under XRD peaks prior to and post LTC, respectively. The FWHM and area under XRD peaks belonging to both α' and γ phases were determined by fitting the peaks with a Voigt function (s. Figure 5.6 inset) using the Peak Analyzer toolbox of Origin 9.0 as described in Ref.[95–97]. Thereupon, the dislocation densities in α' and γ phases were determined according to the modified Williamson-Hall method[98] described in section 5.5.1. The volume fraction of γ phase prior to and post LTC deformation was determined according to the SAE 453[99] method described in section 5.5.2.

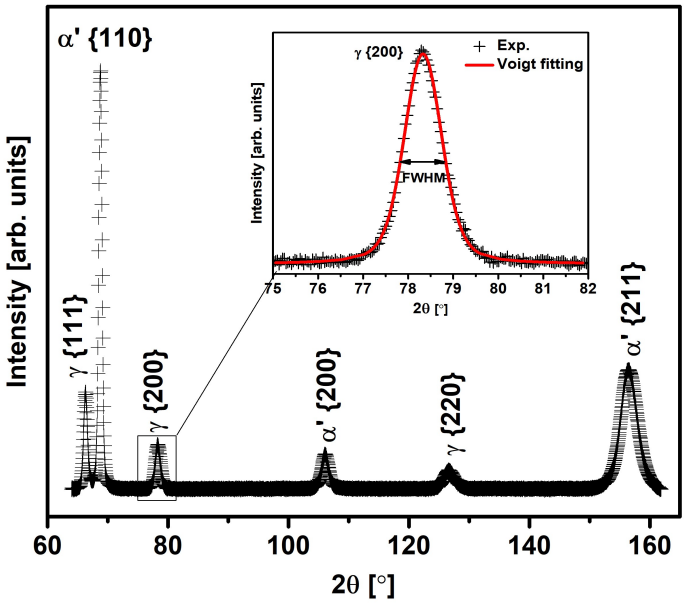

Figure 5.6: XRD pattern of SAE 9254 steel; Inset: Voigt fitting of γ {200} peak to determine the FWHM and area under the peak

5.4.5 Phase Distribution Mapping by EBSD

The specimens for EBSD measurements prior to and post LTC deformation are sectioned from the IQT and martempered wire rods and from the middle of the gauge section of LTC specimens, respectively. These specimens are polished up to 1 μm diamond paste followed by vibration polishing for 4.5 hr with 0.05 μm OPS solution on BUEHLER vibromet 2 equipment. A Helios NanoLab 600 scanning electron microscope (SEM) equipped with an Oxford detector operated at 15 kV and 11 nA was used for data acquisition. A working distance of 10 mm and a step size of $70 - 90$ nm were maintained to record the inverse pole figure (IPF), and respective phase map of the selected areas.

5.5 Analytical Calculation Methods

5.5.1 Determination of Dislocation Density

The dislocation densities in α' and γ phases were determined according to the modified Williamson-Hall method[98] with

$$\Delta K \cong \frac{0.9}{D} + b \cdot M_{\perp} \cdot \sqrt{\rho \cdot \frac{\pi}{2}} \cdot \left(K \cdot \overline{C}^{\frac{1}{2}} \right) \tag{5.1}$$

with $\Delta K = {}^{(2 \cdot cos\theta \cdot \Delta\theta)}/_{\lambda}$ and $K = {}^{(2 \cdot sin\theta)}/_{\lambda}$. Here, $\Delta\theta$ is the corrected FWHM, D is the crystallite size, b is the Burgers vector, $M_{\perp}$ is the dislocation distribution factor, ρ is the dislocation density, θ is the peak position, λ is the wavelength of X-ray source, and $\overline{C}$ is the average dislocation contrast factor for a specific peak.

The elastic constants of α' and γ phases required for the analysis are taken from Ref.[100] and Ref.[101], respectively. As reported by Sastäk et al.[102], the large fraction of dislocations have a rather screw character than an edge character in α' phase. The present analysis is restricted to determining the screw dislocation densities in both α' and γ phases by considering the respective $\overline{C}$ parameters from Ref.[98]. The constant $M_{\perp}$ is considered to be 1.7[95].

Figure 5.7 shows an example of determining the dislocation density specific to α' and γ phases in SAE 9254 steel. According to the Eq. (5.1), the slope of the linear relation between ΔK and $K \cdot \overline{C}^{1/2}$ delivers dislocation density in the specific phase (s. Figure 5.7). The Burgers vector $\frac{a}{2}[111]$ and $\frac{a}{2}[110]$ are considered for the determination of dislocation density in α' and γ phases, respectively.

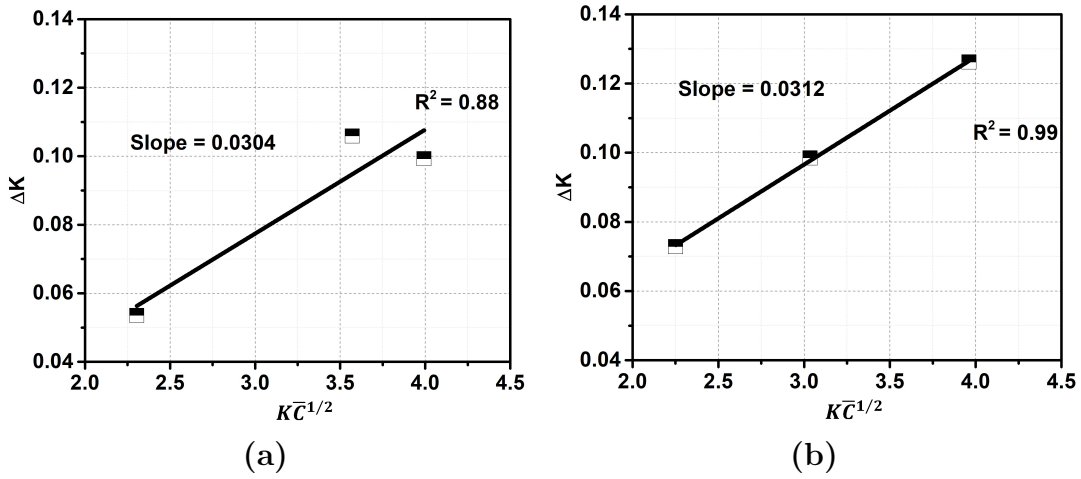

Figure 5.7: ΔK-$K \cdot \overline{C}^{1/2}$ plots of (a) α' phase, (b) γ phase in SAE 9254 steel

5.5.2 Quantification of Retained Austenite

ASTM E975-13[103] and SAE 453[99] are the standard methods available to determine the volume fraction of γ phase in steels. However, the ASTM E975-13 method should apply to the steels with no texture, whereas SAE 453 is applicable to steels with no/low to severe texture cases. In the present studies, SAE 453 method is considered to determine the volume fraction of γ phase in SAE 9254 steel. According to SAE 453 method, the peaks {200}, {220} of γ phase and {200} peak of α' phase should consider to determine the volume fraction of γ phase provided $Cr - K\alpha$ is the XRD source.

The area under the peaks {200}, {220} of γ phase, and {200} peak of α' phase, i.e. I_{γ}^{200}, I_{γ}^{220}, and $I_{\alpha'}^{200}$, are measured by fitting the specific peak with a Voigt function as described in section 5.4.4.

The basic equations to determine the volume fraction of γ phase depend on the degree of texture in the steel. A method for texture determination according to SAE 453 is described in Appendix A. The steel is considered to have no/low, medium, and severe textures if the percentage of deviation ($\%D$) is $< 20\%$, $20 - 200\%$, and $> 200\%$, respectively. It is observed that the considered SAE 9254 steel in the present studies contains either low or medium textures. Thus, the volume fraction of γ phase for specimens with low texture (Eq. (5.2)) and medium texture (Eq. (5.3)) are

$$\%\gamma = \frac{I_{\gamma}^{200}/R_{\gamma}^{200}}{\left(I_{\gamma}^{200}/R_{\gamma}^{200} + I_{\alpha'}^{200}/R_{\alpha'}^{200}\right)} \cdot 100 \tag{5.2}$$

$$\%\gamma = \frac{1}{\left[1 + R_T \cdot \left(\frac{I_{\alpha'}^{200}}{I_{\gamma}^{200}+I_{\gamma}^{220}}\right)\right]} \cdot 100 \tag{5.3}$$

with I_{γ}^{200}, I_{γ}^{220}, and $I_{\alpha'}^{200}$ being the experimentally measured area under the respective peaks, and R_{γ}^{200}, R_{γ}^{220}, $R_{\alpha'}^{200}$ being the theoretically determined area under the respective peaks. The R-values of the respective peaks depend on the composition of the steel grade. Hence, the R-values for SAE 9254 steel grade are calculated as described in Ref.[99] and given in Table A.1. The data set required for the determination of R-values has been taken from the Refs.[94;104]. The R_T in Eq. (5.3) is defined as

$$R_T = \frac{\left(R_{\gamma}^{200} + R_{\gamma}^{220}\right)}{R_{\alpha'}^{200}}, \tag{5.4}$$

which is determined as 4.08 for SAE 9254 composition.

5.5.3 Kernel Average Misorientation Analysis

The IPF maps recorded by SEM-EBSD are used to generate the KAM maps with the aid of an automated OIM Analysis software with a maximum misorientation of 5° by considering the first neighbor as the nearest neighbor.

Besides, the Schmid factor mapping of the scanned area specific to the γ phase is generated for the slip system $(111)[\bar{1}10]$ with a critical resolved shear stress (CRSS) of 0.2 MPa using the same automated OIM Analysis software. A uni-axial tensile loading direction of [100] is considered.

5.6 Basic Material Properties

5.6.1 Mechanical Properties of IQT SAE 9254

The IQT SAE 9254 steel has a UTS and YS σ_e of 2022 MPa and 1820 MPa at 298 K, respectively. The UTS and YS σ_e decreases with increasing temperature T up to 353 K slightly, whereas the RoA increases with increase in temperature T (s. Figure 5.8(a-c)).

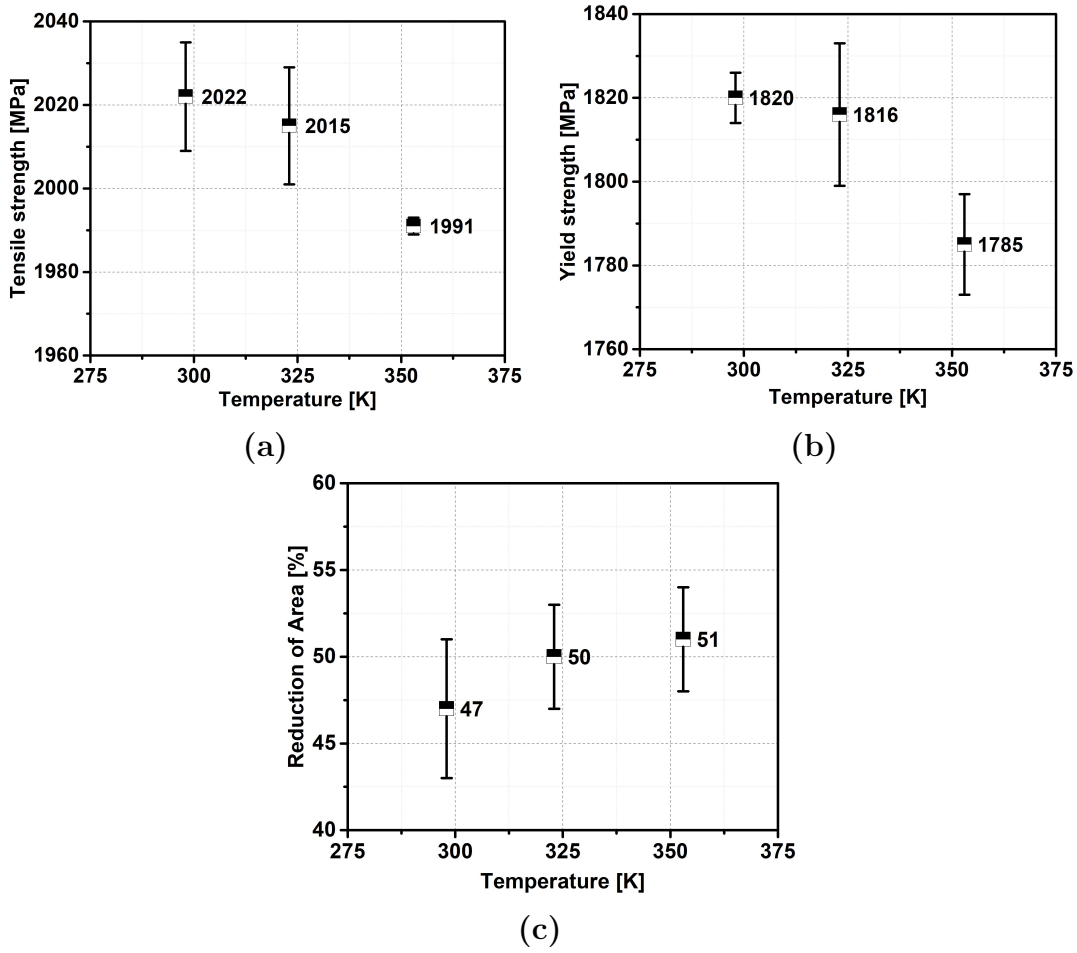

Figure 5.8: Temperature dependence of (a) UTS, (b) YS, and (c) RoA of IQT SAE 9254; the average values along with standard deviation are given in each diagram, respectively

5.6.2 Mechanical Properties of Martempered SAE 9254

The martempered SAE 9254 has a $UTS = 1112\ MPa$ and $\sigma_e = 685\ MPa$ at 298 K. UTS slightly decreases with a raise in temperature T, whereas YS σ_e and RoA remain constant as shown in Figure 5.9(a-c).

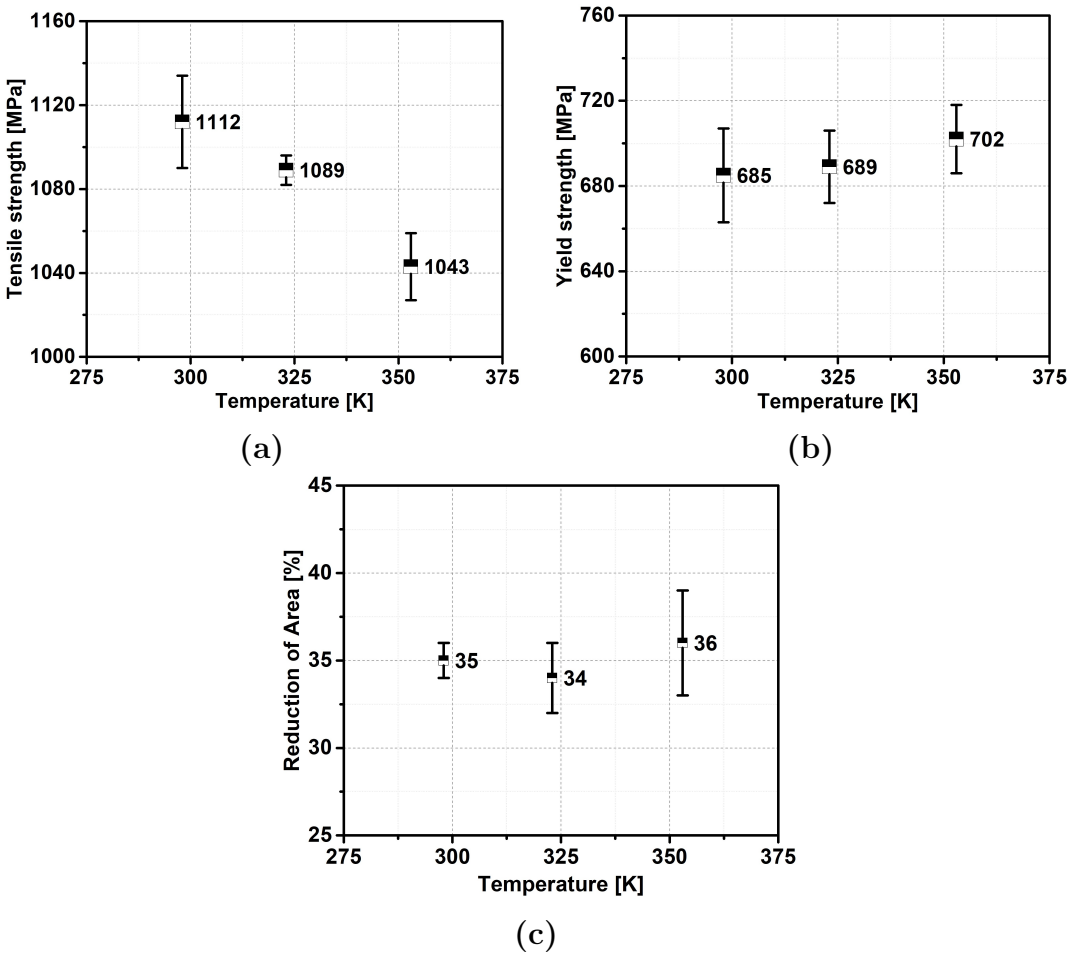

Figure 5.9: Temperature dependence of (a) UTS, (b) YS, and (c) RoA of martempered SAE 9254; the average values along with standard deviation are given in each diagram, respectively

5.6.3 Prior Austenite Grain Size

The adopted IQT heat treatment yields a fine grain microstructure with PAG size of $11 \pm 2\ \mu m$ (s. Figure 5.10(a)). The multiphase nature of the martempered SAE 9254 gets disclosed by means of metallography. Figure 5.10(b) shows the presence of metastable γ phase in α' matrix of the martempered SAE 9254. The PAG boundaries are highlighted in yellow dotted lines.

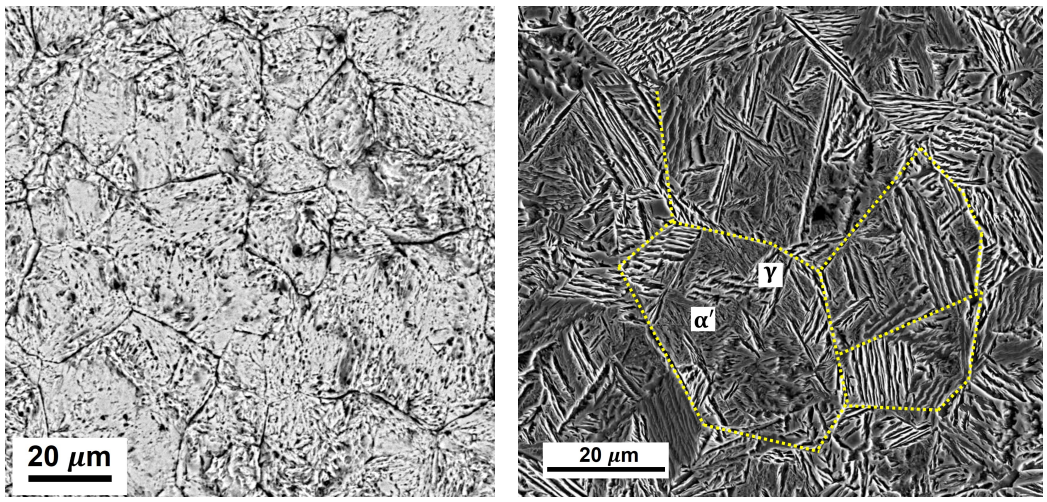

(a) (b)

Figure 5.10: (a) Back-scattered electron (BSE) micrograph illustrating the PAG boundaries in IQT SAE 9254, (b) Secondary electron (SE) micrograph illustrating the PAG boundaries in martempered SAE 9254

5.6.4 Retained Austenite Distribution Mapping

EBSD studies on IQT SAE 9254 revealed that the γ phase (red) distributed in the α' matrix (white) in the form of nano-islands (s. Figure 5.11(a)). The phase map Figure 5.11(b) is disclosing the distribution of γ phase (red) in the α' matrix (white) of martempered SAE 9254. As shown by two insets, the γ phase exists in blocky (γ_B) and filmy (γ_F) morphologies. Furthermore, the blocky γ_B phase is predominant in the vicinity of PAG boundaries (e.g. triple points), and packet boundaries of α' phase, whereas the filmy γ_F phase is located along the α' lath boundaries. These results are in good agreement with the findings of Sastry et al.[57].

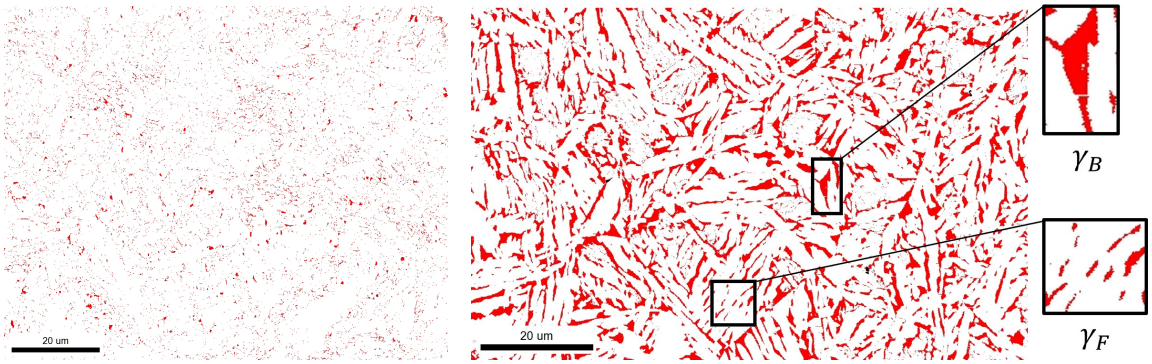

(a) (b)

Figure 5.11: EBSD phase map of (a) IQT SAE 9254, (b) martempered SAE 9254, showing the γ phase (red) distribution in α' matrix (white); Inset: blocky (γ_B) and filmy (γ_F) morphologies of the γ phase

Chapter 6

A Validation of the LTC Mechanism-Based Models

The purpose of this chapter is to verify both the modified SHT and the reworked ECM (refer to Chapter 4) in a two-stage process at the example of IQT SAE 9254 as described in section 3.2. At this stage, the unqualified model shall be ruled out for further validation process. The magnitude of the derived activation volume ν_e and YS σ_e from the second stage fitting of creep parameters are supported in the validation process of the reworked ECM. Eventually, an experimental-based hypothesis of LTC rate-controlling mechanisms in SAE 9254 is proposed based on the microstructural changes observed by means of XRD.

6.1 LTC Behavior of IQT SAE 9254

A set of three specimens, denoted as S1, S2, and S3, was tested in the temperatures 298 $K \leq T \leq 353$ K, and the stresses 1071 $MPa \leq \sigma \leq 1634$ MPa, respectively. It is observed that the LTC strain of IQT SAE 9254 was reproducible for every two specimens. However, there is a deviation in LTC strain data of the third specimen for each temperature T (s. Annexure B.1 and Annexure B.2). In the current studies, the reproducible data set is considered to verify and validate the modified SHT and reworked ECM. Owing to the reproducibility, the results related to one of the specimens at each test condition are presented here in the following sections.

6.2 A Verification of Modified SHT

The LTC strain ε_{cr} data are presented in Figure 6.1(a) and Figure 6.1(b) at regular intervals of 200 s each by individual symbols for the considered stress σ and temperature T levels, respectively. Figure 6.1(a) shows experimentally measured LTC

strain ε_{cr} at stresses 1071 $MPa \leq \sigma \leq$ 1634 MPa at a constant temperature $T = 353\ K$, and Figure 6.1(b) shows experimentally measured LTC strain ε_{cr} at temperatures 298 $K \leq T \leq 353\ K$ at a constant stress $\sigma = 1634\ MPa$. It is evident that the LTC strain ε_{cr} increases with increasing stress σ and temperature T at a given time t. The experimental data, which have been fitted according to the modified SHT creep law (Eq. (4.27)), are represented by solid lines in Figure 6.1. The modified SHT creep law fits well with all the experimental LTC strain ε_{cr} data with a coefficient of determination of $R^2 \geq 0.94$. The derived creep parameters α^S, β^S, and $\exp(\delta^S) = \alpha^S \cdot \beta^S$ by the best fitting of the experimental data are shown in Table 6.1.

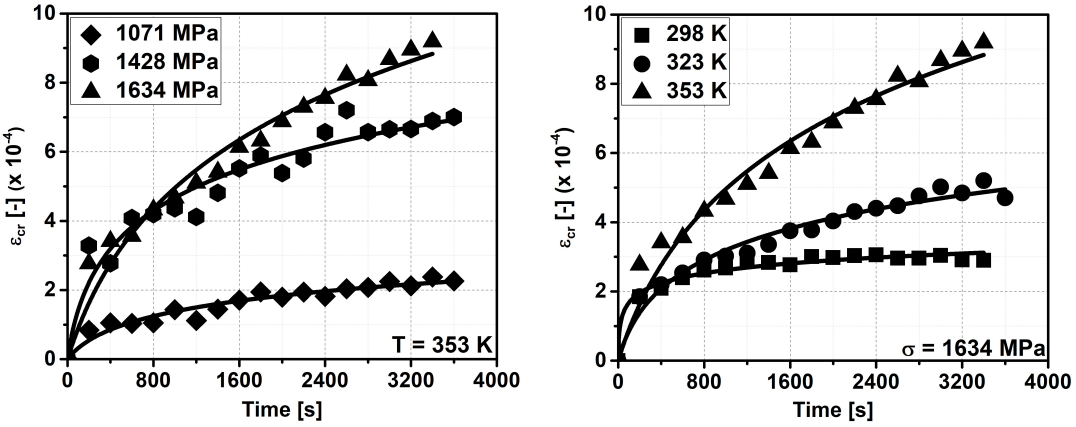

(a) **(b)**

Figure 6.1: Modified SHT fitting of (a) Stress dependent LTC strain at constant temperature $T = 353\ K$, (b) Temperature dependent LTC strain at constant stress $\sigma = 1634\ MPa$

Table 6.1: The creep parameters α^S, β^S, and $\exp(\delta^S)$ by best SHT fitting of LTC data of IQT SAE 9254

Stress $[MPa]$	Temperature $[K]$	α^S $(\cdot 10^{-4})[-]$	β^S $(\cdot 10^{-3})[s^{-1}]$	$\exp(\delta^S)$ $(\cdot 10^{-7})[s^{-1}]$	R^2
1634	298	0.41	574.64	235.60	0.97
1634	323	1.47	7.78	11.39	0.97
1634	353	3.86	2.61	10.09	0.97
1428	353	1.84	11.59	21.39	0.94
1071	353	0.75	5.31	3.98	0.94

In a subsequent step, the creep parameters α^S, $\exp(\delta^S)$ are fitted with respect to the stress σ and temperature T simultaneously according to Eqs. (4.25). Figure 6.2(a, b) shows the stress σ dependence of the creep parameter α_T^S at a constant temperature $T = 353\ K$, and the temperature T dependence of the creep parameter α_σ^S at a constant stress $\sigma = 1634\ MPa$, respectively. The derived creep parameter α^S increases

with increasing stress σ and temperature T. However, the modified SHT conceives the creep parameter α_T^S as an independent of stress σ (s. Eq. (4.25)). Furthermore, the temperature T dependence of the creep parameter α_σ^S is poorly described by the modified SHT with a coefficient of determination $R^2 = 0.70$ (s. Figure 6.2(b)).

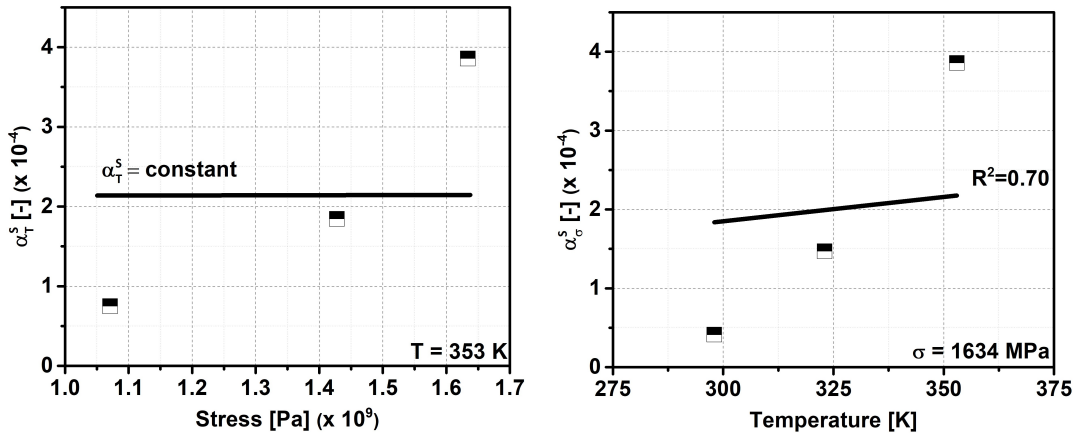

(a) (b)

Figure 6.2: (a) Stress dependence of creep parameter α_T^S at a constant temperature $T = 353\ K$, (b) Temperature dependence of creep parameter α_σ^S at constant stress $\sigma = 1634\ MPa$

Figure 6.3(a, b) shows the stress σ dependence of creep parameter $\exp(\delta_T^S)$ at a constant temperature $T = 353\ K$, and the temperature T dependence of creep parameter $\exp(\delta_\sigma^S)$ at a constant stress $\sigma = 1634\ MPa$, respectively. It is evident that the modified SHT is incapable of describing the stress σ and temperature T dependence of the creep parameter $\exp(\delta^S)$ with a poor coefficient of determination $R^2 = 0.08$.

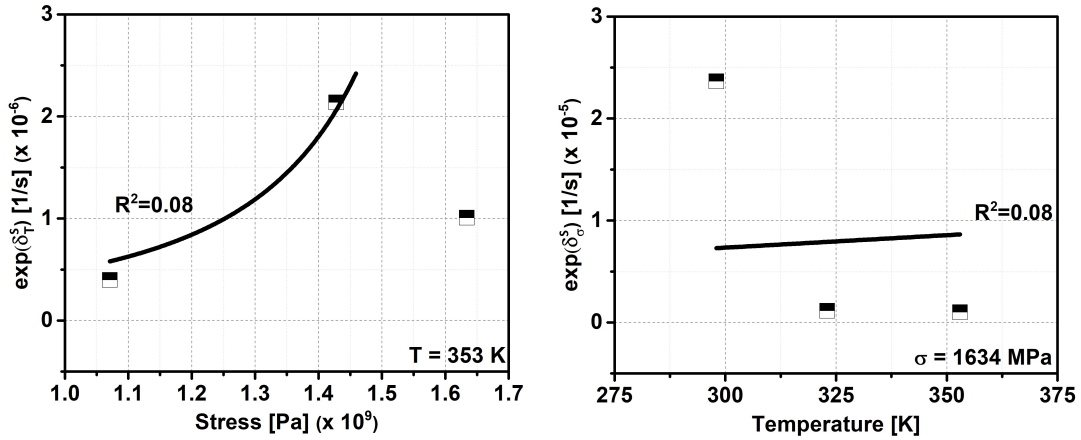

(a) (b)

Figure 6.3: (a) Stress dependence of creep parameter $\exp(\delta_T^S)$ at a constant temperature $T = 353\ K$, (b) Temperature dependence of creep parameter $\exp(\delta_\sigma^S)$ at constant stress $\sigma = 1634\ MPa$

In summary, the modified SHT fits well with the stress and temperature dependent

LTC strain of IQT SAE 9254 in the temperatures 298 $K \leq T \leq 353$ K and the stresses 1071 $MPa \leq \sigma \leq 1634$ MPa. However, it is incapable of describing the stress and temperature dependence of the creep parameters α^S and $\exp(\delta^S)$. Hence, the unqualified modified SHT is excluded for further validation.

6.3 A Verification and Validation of Reworked ECM

The very same stress σ and temperature T dependent LTC strain ε_{cr} data of IQT SAE 9254 presented in the above section is considered to verify the reworked ECM. The experimental data, which have been fitted according to the reworked ECM creep law (s. Eq. (4.32)), are represented by solid lines in Figure 6.4. The reworked ECM

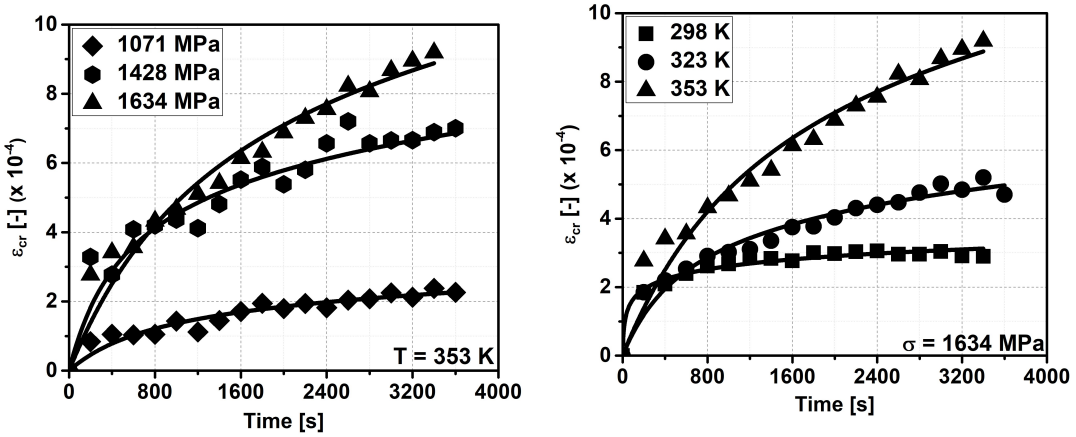

(a) (b)

Figure 6.4: Reworked ECM fitting of (a) Stress dependent LTC strain at constant temperature $T = 353$ K, (b) Temperature dependent LTC strain at constant stress $\sigma = 1634$ MPa

creep law fits well with all the experimental LTC strain ε_{cr} data with a coefficient of determination of $R^2 \geq 0.92$. The derived creep parameters α^E, f_0^*, and f_1^* by best ECM fitting of the experimental data are shown in Table 6.2.

Table 6.2: The creep parameters α^E, f_0^*, and f_1^* by best ECM fitting of experimental LTC data of IQT SAE 9254.

Stress $[MPa]$	Temperature $[K]$	α^E $(\cdot 10^{-4})[-]$	f_0^* $(\cdot 10^{-3})[s^{-1}]$	f_1^* $(\cdot 10^{-13})[s^{-1}]$	R^2
1634	298	0.43	288.13	0.084	0.97
1634	323	1.40	5.41	1.06	0.97
1634	353	3.38	2.29	14.09	0.96
1428	353	1.82	6.69	1.77	0.92
1071	353	0.70	3.88	2.43	0.93

In a subsequent step, the creep parameters α^E, f_0^*, and f_1^* are fitted with respect to stress σ and temperature T simultaneously according to Eq. (4.33) and Eq. (4.35). To shed light on the relative number ${}^{n(T)}/_{n(T=T_0)}$ of multiple activations of dislocation during LTC deformation, it is determined here by considering the fitting parameter $f_0^*(T)$ at 298 $K \leq T \leq$ 353 K and constant stress $\sigma = 1634\ MPa$. With Eq. (4.35), the relative number ${}^{n(T)}/_{n(T=T_0)}$ of activation reads

$$\frac{n(T)}{n(T=T_0)} = \frac{f_0^*(T=T_0)}{f_0^*(T)}. \tag{6.1}$$

Figure 6.5 shows that it increases linearly with temperature T. The best fitting to a linear function

$$\frac{n(T)}{n(T=T_0)} \approx \Phi(T) = a \cdot (T - T_0) + 1 \tag{6.2}$$

delivers parameters $a = 2.274\ K^{-1}$ and $T_0 = 298\ K$ with a coefficient of determination of $R^2 = 0.99$.

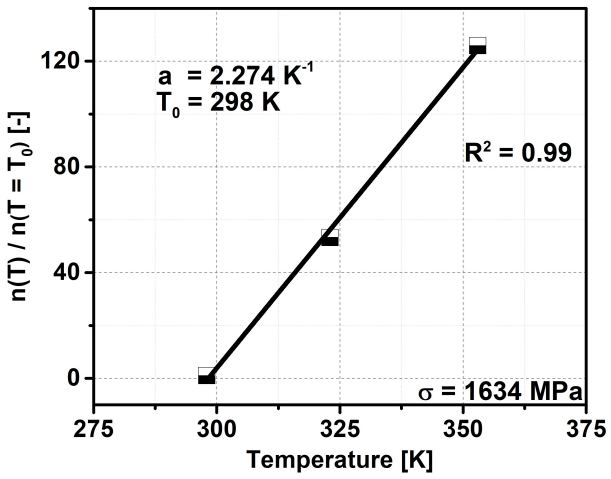

Figure 6.5: Temperature dependence of ${}^{n(T)}/_{n(T=T_0)}$ at constant stress $\sigma = 1634\ MPa$

Subsequently, the creep parameters α^E and ${}^{f_1^*}/_{f_0^*}$ have been fitted with respect to the stress σ and temperature T simultaneously in 3-dimensional according to Eq. (4.33) and Eq. (4.35). For convenience, these fits are shown here in 2-dimensional plots (s. Figure 6.6 and Figure 6.7). Figure 6.6(a, b) shows the stress σ dependence of the creep parameter α_T^E at a constant temperature $T = 353\ K$, and the temperature T dependence of the creep parameter α_σ^E at a constant stress $\sigma = 1634\ MPa$, respectively. The creep parameter α^E increases with increasing stress σ and temperature T. It is well described by Eq. (4.33) according to the reworked ECM with a coefficient of determination of $R^2 = 0.96$ (s. Figure 6.6). The fitting parameters C, σ_e are determined as 0.9842 Pa and 2160 MPa, respectively. Figure 6.7(a, b) shows the stress σ dependence of creep parameter ${}^{f_1^*}/_{f_0^*}\big|_T$ at a constant temperature $T = 353\ K$, and the temperature T dependence of creep parameter ${}^{f_1^*}/_{f_0^*}\big|_\sigma$ at a constant stress

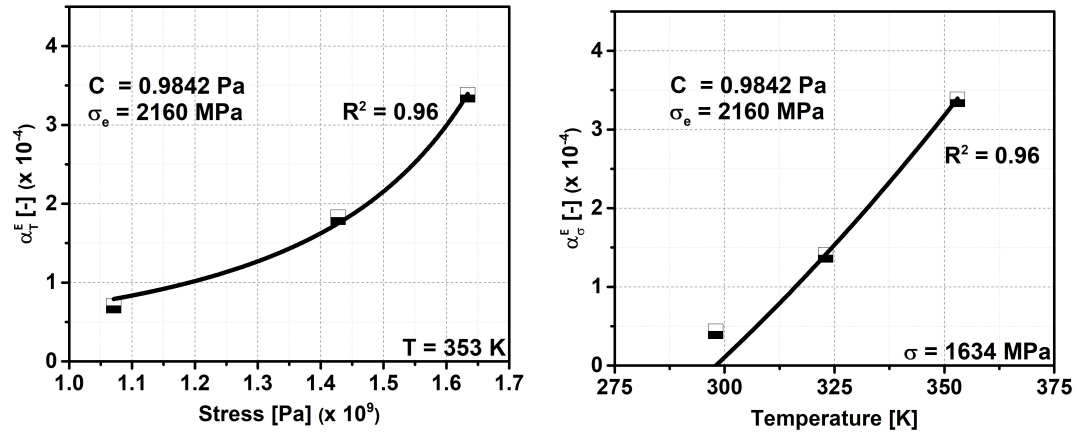

(a) (b)

Figure 6.6: (a) Stress dependence of creep parameter α_T^E at constant temperature $T = 353\ K$, (b) Temperature dependence of creep parameter α_σ^E at constant stress $\sigma = 1634\ MPa$

$\sigma = 1634\ MPa$, respectively. The stress σ and temperature T dependence of creep parameter f_1^*/f_0^* is well described by Eq. (4.35) according to the reworked ECM with a coefficient of determination of $R^2 = 0.97$. The fitting parameter ν_e is determined as $1.96 \cdot 10^{-28}\ m^3$.

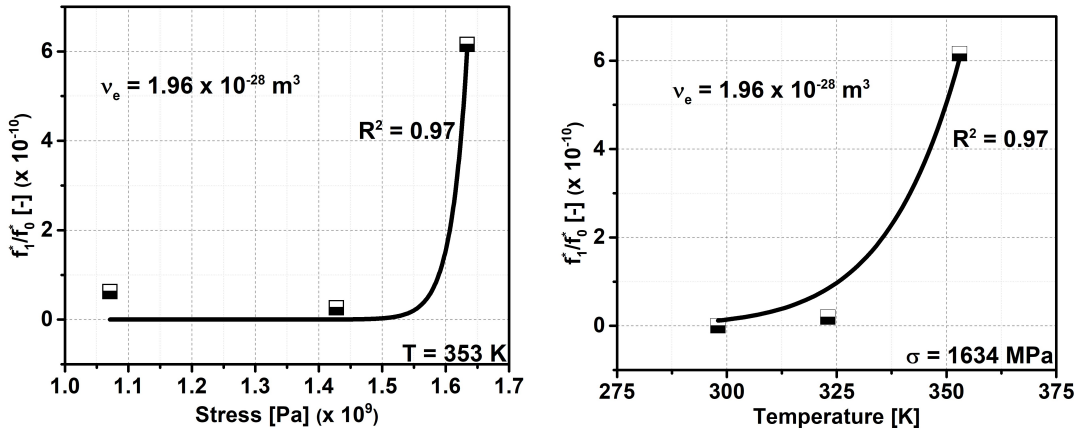

(a) (b)

Figure 6.7: (a) Stress dependence of the creep parameter $f_1^*/f_0^*|_T$ at constant temperature $T = 353\ K$, (b) Temperature dependence of the creep parameter $f_1^*/f_0^*|_\sigma$ at constant stress $\sigma = 1634\ MPa$

Figure 6.8 shows the average content of γ phase in IQT steel rods prior to and post LTC testing performed within $298\ K \leq T \leq 353\ K$ at constant stress $\sigma = 1634\ MPa$. The γ phase content in the IQT rod is 8.9% which is considered as a reference, whereas the volume fraction of γ phase in the deformed LTC specimens is about 7.6% irrespective of the test temperature T.

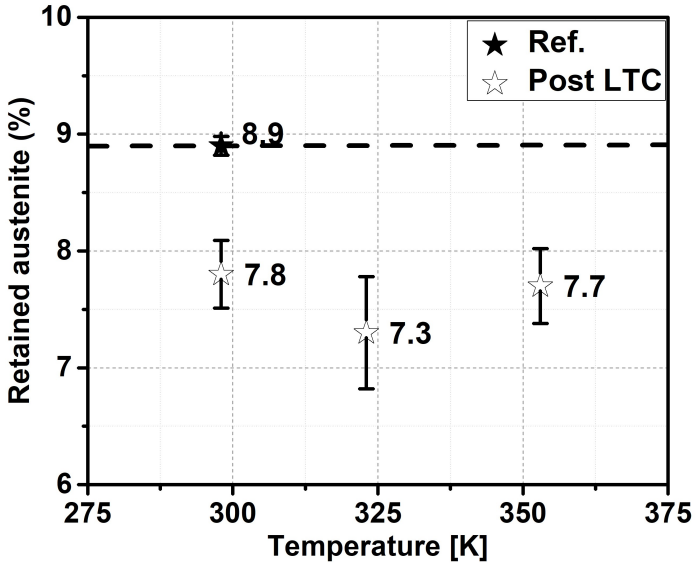

Figure 6.8: The volume fraction of γ phase prior to and post LTC testing performed at 298 $K \leq T \leq 353$ K and constant stress $\sigma = 1634$ MPa

In a nutshell, the modified SHT is unqualified to describe the LTC behavior of IQT SAE 9254 owing to its inability of describing the stress σ and temperature T dependence of the creep parameters α^S, $\exp(\delta^S)$. The reworked ECM fits well to the stress σ and temperature T dependence of LTC strain ε_{cr}, and the creep parameters α^E, f_1^*/f_0^*. Consequently, the reworked ECM describes the LTC behavior of the investigated IQT SAE 9254. Furthermore, the value of σ_e is determined by fitting the creep parameter α^E with respect to stress σ and temperature T as 2160 MPa, which is in the expected range of YS σ_e of the investigated IQT SAE 9254. The mean activation volume ν_e in Eq. (4.35) is determined by fitting the creep parameter f_1^*/f_0^* with respect to stress σ and temperature T as $1.96 \cdot 10^{-28}$ m^3. It indicates overcoming the Peierls-Nabarro stress as the mechanism for dislocation motion, which is the base for constructing the reworked ECM. Furthermore, the drop in the volume fraction of γ phase determined by XRD is supported in constructing an experimental-based hypothesis of LTC rate-controlling mechanisms in IQT SAE 9254 (refer to Chapter 7).

Chapter 7

An Experimental-Based Hypothesis of LTC Controlling Mechanisms in SAE 9254

First and foremost, the ability of reworked ECM in describing the stress σ and temperature T dependent LTC strain ε_{cr} of martempered SAE 9254 is verified. Once the reworked ECM is successfully validated, the firm microstructural evidence is produced with the aid of XRD and SEM-EBSD to propose and validate the LTC rate-controlling mechanisms in SAE 9254.

7.1 LTC Behavior of Martempered SAE 9254

A set of three specimens, denoted as S1, S2, and S3, was tested in the temperatures 298 $K \leq T \leq$ 353 K, and stresses 421 $MPa \leq \sigma \leq$ 632 MPa combinations for a duration of 1 hr at each condition, respectively. Unexpected deviations between the measured LTC data of the three specimens at each given test condition were observed (s. Annexure B.3 and Annexure B.4). It is assumed that the mixing of specimens from the three separate batches of martempered wire rods is the root cause. Alfredsson et al.[26] reported that the deviations in small-scale LTC strain are caused by the microstructural differences on a microscopic scale even though the very same heat treatment procedure was adopted for all the batches. The LTC strain data were carefully smoothed and subsequently fitted to the reworked ECM creep law (Eq. (4.32)). However, the S1 and S3 data performed at 421 MPa and 492 MPa at 353 K were excluded for further analysis since these data do not resemble the LTC behavior. The reworked ECM creep law fits well with the remaining experimental LTC strain data with a coefficient of determination of $R^2 \geq 0.91$. The creep parameters α^E, f_0^*, and f_1^* are given in Table 7.1 to Table 7.3.

Table 7.1: The fitted creep parameter α^E of the experimental LTC data of martempered SAE 9254

Stress $[MPa]$	Temperature $[K]$	α^E $(\cdot 10^{-5})[-]$		
		S1	S2	S3
632	298	6.54	2.89	2.06
632	323	5.23	6.50	4.61
632	353	6.17	15.06	6.53
562	353	6.55	6.46	4.01
492	353	-	6.30	-
421	353	-	2.37	-

Table 7.2: The fitted creep parameter f_0^* of the experimental LTC data of martempered SAE 9254

Stress $[MPa]$	Temperature $[K]$	f_0^* $(\cdot 10^{-3})[s^{-1}]$		
		S1	S2	S3
632	298	72.27	513.16	403.91
632	323	381.02	31.18	257.12
632	353	30.00	7.60	26.22
562	353	13.40	26.36	265.59
492	353	-	2.41	-
421	353	-	8.77	-

Table 7.3: The fitted creep parameter f_1^* of the experimental LTC data of martempered SAE 9254

Stress $[MPa]$	Temperature $[K]$	f_1^* $(\cdot 10^{-14})[s^{-1}]$		
		S1	S2	S3
632	298	1.63	10.00	10.00
632	323	10.00	3.34	10.00
632	353	503.49	33.74	350.41
562	353	5.45	1.47	8.64
492	353	-	0.81	-
421	353	-	0.77	-

Due to the deviations between the LTC strain data of the three samples at each test condition, the mean and extreme values of the creep parameter f_0^* are considered (s. Table 7.4).

Table 7.5 shows the relative numbers ${}^{n(T)}/_{n(T=T_0)}$ of dislocation activation for temperatures 298 $K \leq T \leq 353$ K at constant stress $\sigma = 632$ MPa corresponding to the mean and extreme values of the creep parameter f_0^*, respectively.

Table 7.4: The mean and extreme values of the creep parameter f_0^* are derived from Table 7.2

Stress $[MPa]$	Temperature $[K]$	f_0^* $(\cdot 10^{-3})[s^{-1}]$		
		mean	max.	min.
632	298	329.78	513.16	72.27
632	323	223.11	381.02	31.18
632	353	21.27	30.00	7.60

Table 7.5: The temperature dependence of mean and extreme relative numbers ${}^{n(T)}/_{n(T=T_0)}$ dislocation activation of the experimental LTC data

Stress $[MPa]$	Temperature $[K]$	${}^{n(T)}/_{n(T=T_0)}$ [-]		
		mean	max.	min.
632	298	1.0	1.0	1.0
632	323	1.5	1.3	2.3
632	353	15.5	17.1	9.5

As shown in Figure 7.1, it increases with temperature T. The best fitting to a linear function

$$\frac{n(T)}{n(T=T_0)} \approx \Phi(T) = a \cdot (T - T_0) + 1 \tag{7.1}$$

delivers parameters $a = 0.2706\ K^{-1}$ and $T_0 = 302.5\ K$ with a coefficient of determination $R^2 = 0.82$.

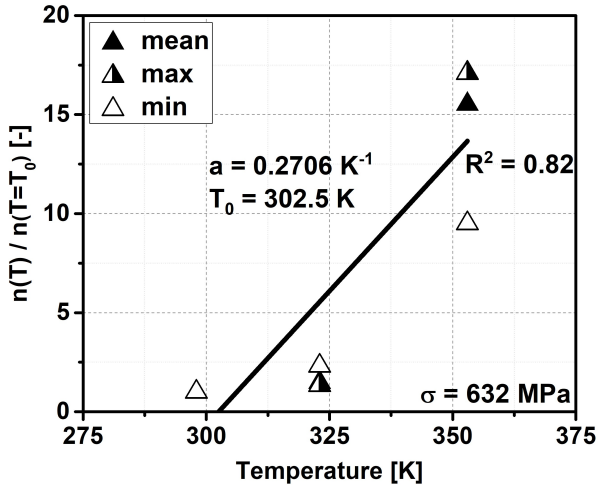

Figure 7.1: Temperature dependence of mean and extreme relative numbers ${}^{n(T)}/_{n(T=T_0)}$ of the experimental LTC data at constant stress $\sigma = 632\ MPa$

Despite the deviations between the LTC strain data, the reworked ECM still describes the fundamental trend in stress σ and temperature T of the creep parameters $n(T)$, $\alpha^E(\sigma, T)$, $f_0^*(T)$, and $f_1^*(T)$ (s. Table 7.1 to Table 7.3)[28]. Thus, it is expected

that the proposed hypothesis of the LTC contributing mechanism in IQT SAE 9254 (refer to Chapter 6) is still valid in the case of here considered martempered SAE 9254. Consequently, LTC strain in martempered SAE 9254 is assumed to be contributed by the localized slip in the γ phase. The reduction in LTC rate with time can then be attributed to the exhaustion of this specific mechanism by phase transformation of the γ phase[28].

7.2 Microstructural Characterization

7.2.1 A Quantification of Dislocation Density and Phase Fraction of the Retained Austenite

Figure 7.2 shows the XRD patterns of prior to (reference) and post LTC deformation specimens for 298 $K \leq T \leq 353$ K at a constant stress $\sigma = 632$ MPa. The {110}, {200}, {211} peaks and {111}, {200}, {220} peaks of the α' phase and γ phase are indexed, respectively. The changes in dislocation densities of α' and γ phases of

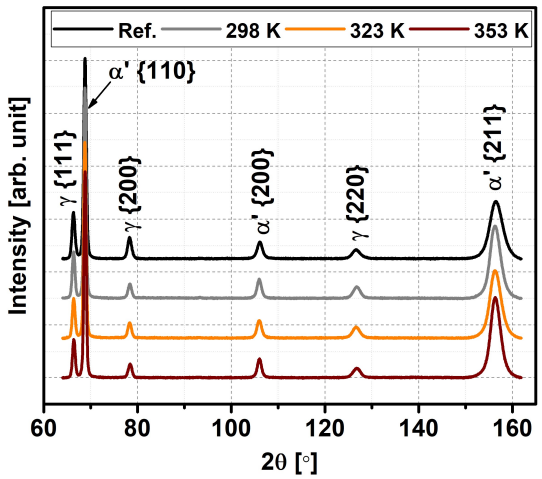

Figure 7.2: XRD patterns of prior to (reference) and post LTC deformation specimens for 298 $K \leq T \leq 353$ K at constant stress $\sigma = 632$ MPa

martempered SAE 9254 were determined according to the modified Williamson-Hall method (refer to section 5.5.1), and presented in Figure 7.3(a). The α' phase and γ phase show only a minor reduction in dislocation density due to LTC deformation up to 323 K (s. Figure 7.3(a)). Only the LTC sample at 353 K shows a considerable reduction of dislocation density in the α' phase and a moderate increase of dislocation density in the γ phase. The volume fraction of γ phase, which is 31.2% in the reference sample, gets reduced by LTC and it remains in the range of $24.8 - 26.1\%$ (s. Figure 7.3(b)).

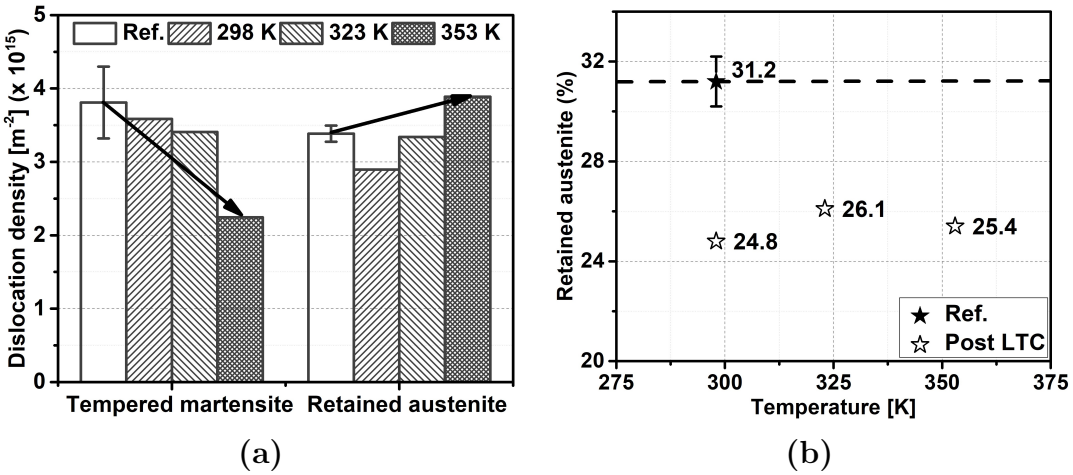

Figure 7.3: (a) Dislocation density per phase, and (b) Volume fraction of γ phase prior to and post LTC for 298 $K \leq T \leq 353$ K at constant stress $\sigma = 632$ MPa

7.2.2 KAM Analyses of Martempered SAE 9254

Figure 7.4 shows the KAM mapping prior to and post LTC deformation at temperature $T = 353$ K and stress $\sigma = 632$ MPa. A major part of both maps is covered by areas of α' and γ phases having misorientations of $0 - 1°$. However, Figure 7.4(b) shows

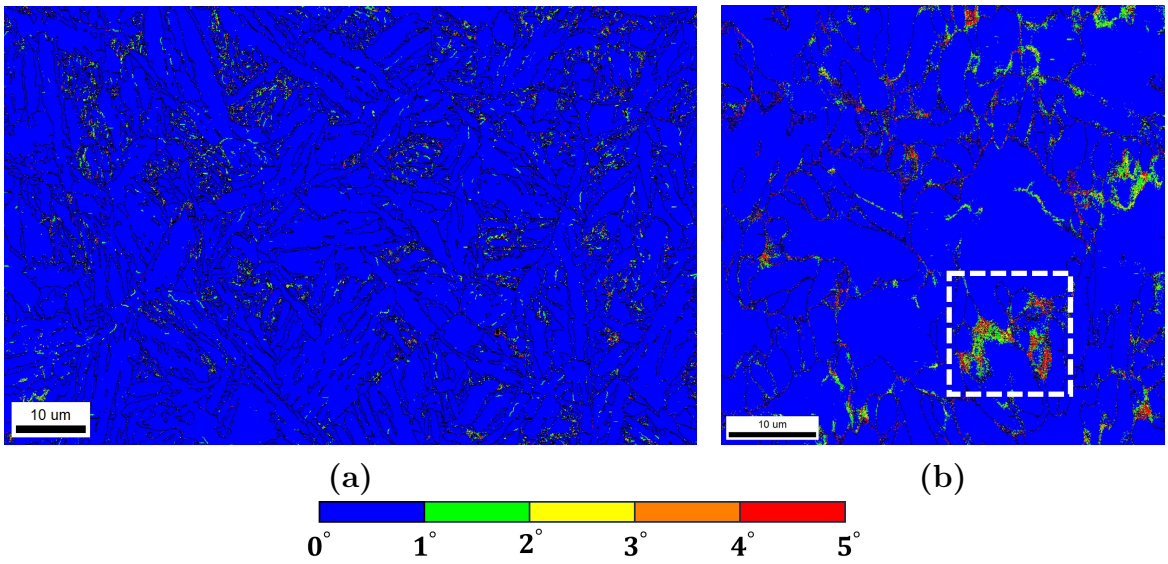

Figure 7.4: KAM mapping of martempered SAE 9254 (a) Prior to LTC, and (b) Post LTC performed at 353 K and at constant stress $\sigma = 632$ MPa

more spots belonging to a higher misorientation of $4 - 5°$ caused by LTC deformation. It reveals that the share of areas of α' and γ phases showing misorientations of $4 - 5°$ rose to 1.5% and 2.3%, respectively due to LTC deformation. The KAM analyses and phase map of the same area (s. Figure 7.4(b)) specific to α' and γ phases post LTC performed at 353 K are shown in Figure 7.5(a, c) and Figure 7.5(b, d), respectively.

The black areas of Figure 7.5 represent the respective other phase. For example, in Figure 7.5(a, c) the γ phase areas become black while considering the KAM and phase map specific to α' phase. Although a major part is covered by areas of α' and γ phases having misorientations of $0-1°$, one can notice the significant microstructural changes due to LTC deformation locally in the selected area (s. white box in Figure 7.5).

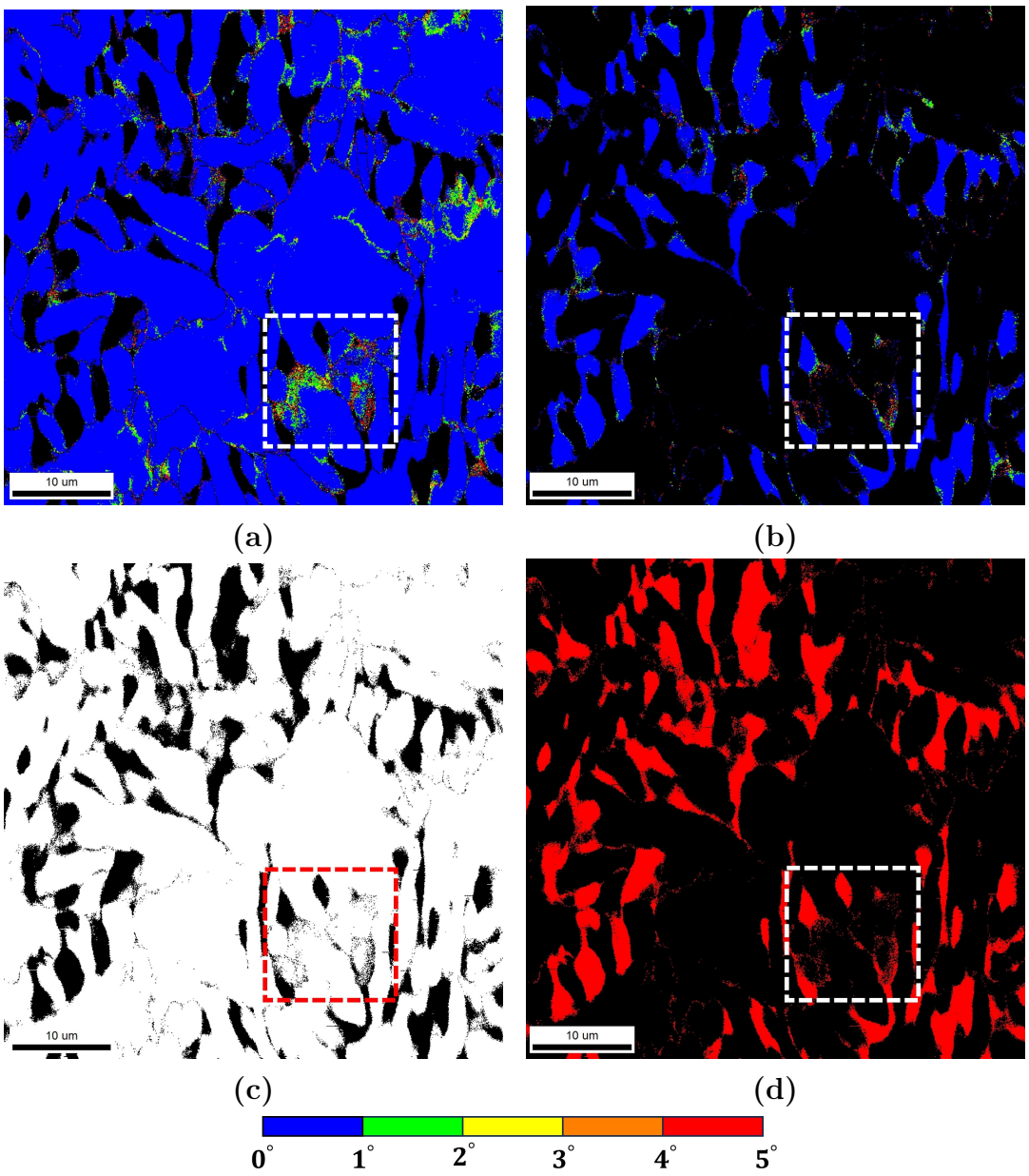

Figure 7.5: KAM analyses and phase map of the same area (s. Figure 7.4(b)) specific to (a, c) α' phase, (b, d) γ phase post LTC performed at 353 K, respectively; Note: α' phase (white) and γ phase (red) in Figure 7.5(c, d)

The KAM map of the selected area contains an aggregation of misorientations of $1-5°$ spread in both α' and γ phases. For better visualization of the microstructural changes, the selected area (s. white box in Figure 7.5) is shown with higher magnification in Figure 7.6. The KAM map of the selected area (s. Figure 7.6(a)) contains an

aggregation of misorientations of $1-5°$. The corresponding α' and γ phase specific KAM maps (s. Figure 7.6(b, c)) disclose that the majority of spots with misorientation of $1-3°$ are made up by α' phase. Within the γ phase, the spots with misorientation of $4-5°$ are more dominant.

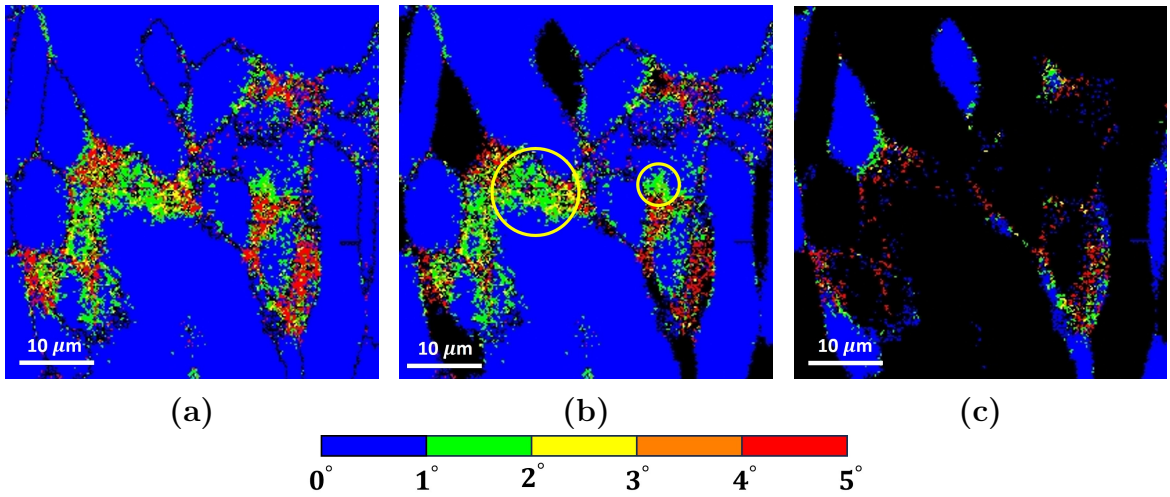

Figure 7.6: KAM maps of the selected area marked with a white box in Figure 7.5 (a) Overall, (b) α' phase specific, and (c) γ phase specific

Chapter 8

Discussion

The LTC mechanism-based models, i.e. SHT and ECM, are developed (refer to Chapter 4) by restricting the obstacles having activation stresses σ_i up to YS σ_e, and introducing a reasonable stress σ dependent obstacle distribution function ϕ_σ (s. Eq. (4.11)). The modified SHT related to a logarithmic creep law exhibits stress σ dependence of LTC strain in terms of the creep parameter $\delta^S(\sigma, T)$, however, the creep parameter $\alpha^S(T)$ remains stress σ independent (s. Eqs. (4.25)). Unlike the modified SHT, the reworked ECM follows a non-logarithmic creep law (s. Eq. (4.32)) as anticipated by Cottrell [89]. The reworked ECM exhibits stress σ dependence of LTC strain in terms of the creep parameters $\alpha^E(\sigma, T)$ and $f_1^*(\sigma, T)$ (s. Eq. (4.33) and Eq. (4.34)).

In Chapter 6, both the modified SHT and reworked ECM are experimentally verified at the example of IQT SAE 9254. The experimentally measured LTC strain ε_{cr} in IQT SAE 9254 exhibits significant stress σ and temperature T dependence in the temperatures $298\ K \leq T \leq 353\ K$ and the stresses $1071\ MPa \leq \sigma \leq 1634\ MPa$. The modified SHT fits well with the LTC strain ε_{cr} of IQT SAE 9254 at each abovementioned temperature T, and stress σ combinations, respectively (s. Figure 6.1). However, it is incapable of describing the stress σ and temperature T dependence of the creep parameters $\alpha^S(T)$ and $\delta^S(\sigma, T)$ (s. Figure 6.2 and Figure 6.3). An LTC mechanism-based model ought to describe the stress σ and temperature T dependence of LTC strain, as well as the creep parameters correctly. Thus, the unqualified modified SHT is excluded for further validation.

In contrast to that the reworked ECM is capable to describe the LTC strain ε_{cr} in IQT SAE 9254, as well as the stress σ and temperature T dependence of the creep parameters $n(T)$, $\alpha^E(\sigma, T)$, and ${f_1^*}^{(\sigma,T)}/_{f_0^*(T)}$, respectively (s. Figure 6.5 to Figure 6.7). The value of σ_e is determined by fitting the creep parameter α^E with respect to stress σ and temperature T as $2160\ MPa$, which is in the expected range of YS σ_e of the investigated IQT SAE 9254. The mean activation volume ν_e in Eq. (4.35) is determined by fitting the creep parameter ${f_1^*}/_{f_0^*}$ with respect to stress σ and temperature T as $1.96 \cdot 10^{-28}\ m^3$ that is equal to $12 \cdot b^3$ with the Burgers vector b of the most favourable

slip system in γ phase, i.e. (111)[110]. As reported by Conrad[105], the magnitude of activation volume ν_e indicates overcoming the Peierls-Nabarro stress as the mechanism for dislocation motion, which is the base for constructing the reworked ECM. It is proposed by strictly following the work of Neu et al.[25] and Alfredsson et al.[26] that the LTC strain ε_{cr} in IQT SAE 9254 is contributed by slip localization within γ phase.

It is evident from Figure 6.5 that the relative number ${}^{n(T)}/_{n(T=T_0)}$ of multiple activations of dislocation before exhaustion increases with temperature T during LTC deformation. The fitting parameter T_0 in Eq. (6.2) is determined as 298 K. It indicates that the dislocation activation ceases below ambient temperature, which is plausible to consider. Figure 8.1 shows the normalized LTC rate ${}^{\dot{\varepsilon}_{cr}(t)}/_{\dot{\varepsilon}_{cr}(t=0)}\big|_{\sigma}$ as a function of time t for three different temperatures T. The drop in normalized LTC rate ${}^{\dot{\varepsilon}_{cr}(t)}/_{\dot{\varepsilon}_{cr}(t=0)}\big|_{\sigma}$ with time t might be attributed to the exhaustion of dislocation glide within γ phase due to phase transformation of γ to α' phase. It is evident from

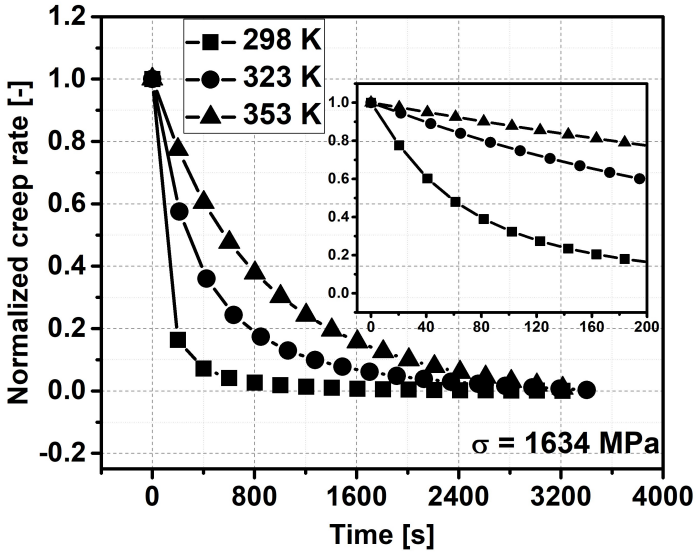

Figure 8.1: Normalized LTC rate ${}^{\dot{\varepsilon}_{cr}(t)}/_{\dot{\varepsilon}_{cr}(t=0)}\big|_{\sigma}$ as a function of time, temperature for LTC at 298 $K \leq T \leq 353$ K and at constant stress $\sigma = 1634$ MPa; Inset: Details are shown for a short time interval, i.e. upto 200 s

Figure 6.8 that the fraction of γ phase dropped by 15% of its initial amount during LTC deformation irrespective of the test temperature T, which might be due to the occurrence of phase transformation locally in the deformed γ phase. Furthermore, the drop in normalized LTC rate ${}^{\dot{\varepsilon}_{cr}(t)}/_{\dot{\varepsilon}_{cr}(t=0)}\big|_{\sigma}$ becomes sluggish at elevated temperatures. As shown in Figure 8.1 inset, the LTC rate $\dot{\varepsilon}_{cr}(t)$ dropped to 20% of its initial values in less than 200 s at 298 K, whereas this time t is higher for 353 K. The relation between $\ddot{\varepsilon}_{cr}(t)$ and $n(T)$ for the short time interval is derived from Eq. (4.33) and

Eq. (4.34) as

$$\ddot{\varepsilon}_{cr}(t) = -\alpha^E \cdot \frac{f_0^2}{2} \cdot \frac{1}{n^2(T)}. \tag{8.1}$$

One can realize from Eq. (8.1) that the rate of drop in LTC rate $\dot{\varepsilon}_{cr}(t)$ is inversely proportional to $n^2(T)$. As shown in Figure 6.5, $n(T)$ increases linearly with temperature T. Consequently, the rate of drop in $\dot{\varepsilon}_{cr}(t)$ can be considered as inversely proportional to T^2, which indicates that the rate of drop in $\dot{\varepsilon}_{cr}(t)$ becomes sluggish at elevated temperature T, for a given time t. This can be justified in terms of the stability of the γ phase (refer to section 2.2). Neu et al.[24] reported that the stability of γ phase increases with temperature T. As the γ phase stability increases, there would be high chances for multiple activations of dislocation within the γ phase prior to its transformation into α' phase. Based on these experimental results, the hypothesis of the LTC mechanism implies that LTC strain $\varepsilon_{cr}(t)$ in IQT SAE 9254 is contributed by slip localization within γ phase, whereas reduction in LTC rate is controlled by phase transformation, which might be occurring locally in the deformed γ phase.

However, it is challenging to validate the hypothesis at the example of IQT SAE 9254 that contains a rather low volume fraction of γ phase (8.9%) in the form of nano-islands (s. Figure 5.11(a)). Consequently, the author feels increasing the γ phase would be convenient to validate the proposed hypothesis of the LTC rate-controlling mechanisms in SAE 9254. Hence, the martempering technology is considered to increase the volume fraction of the γ phase in the very same SAE 9254 steel grade (refer to section 5.2.2).

First and foremost, the ability of reworked ECM in describing the stress σ and temperature T dependence of LTC strain ε_{cr} of martempered SAE 9254 is verified (refer to Chapter 7). In spite of deviations observed in LTC strain data of martempered SAE 9254, the reworked ECM is capable to describe the fundamental trend in stress σ and temperature T of the creep parameters $n(T)$, $\alpha^E(\sigma, T)$, $f_0^*(T)$, and $f_1^*(T)$ (s. Table 7.1 to Table 7.3)[28]. Thus, dislocation glide by overcoming the Peierls-Nabarro stress shall be considered as one of the basic mechanisms of LTC in martempered SAE 9254.

However, martempered SAE 9254 is not a single-phase material. It contains a significant amount of metastable γ phase in blocky γ_B and filmy γ_F morphologies distributed in the major α' matrix (s. Figure 5.11(b)). The chemical and mechanical stability of the γ phase in martensitic steels depends on several factors, e.g. composition, morphology, stress, temperature, strain, and strain rate[52]. It has been often reported that the blocky γ_B phase has a lower carbon content than the filmy γ_F phase. Consequently, the less stable γ_B phase transforms to martensite, whereas the γ_F phase remains stable against phase transformation even after fracture[58]. However, the filmy γ_F phase is vulnerable to elevated temperatures and decomposes into

ferrite and carbides owing to its high carbon concentration [59]. The investigations of Neu et al. [24;25;72], who considered carburized 4320 steel contains 35% of γ phase revealed that SAMT occurs predominantly in the temperatures 295 $K \leq T \leq 323$ K during monotonic and cyclic loading (s. Figure 2.4). Besides, they observed no SAMT beyond 333 K. Figure 7.3(b) shows the changes in volume fraction of γ phase due to LTC deformation for 298 $K \leq T \leq 353$ K at a constant stress $\sigma = 632$ MPa. The volume fraction in the reference sample is 31.2%, whereas the LTC samples have a volume fraction of γ phase in the range of $24.8 - 26.1\%$. The drop in volume fraction of the γ phase can be attributed to the occurrence of SAMT during LTC testing, especially at the temperatures 298 $K \leq T \leq 323$ K. Beyond that temperature, SIMT might take the place of SAMT [28]. Hence, SAMT and, at elevated temperatures, SIMT are to be considered as additional mechanisms contributing to LTC through volumetric changes.

The dislocation densities in α' phase and γ phases are slightly dropping during LTC up to 323 K (s. Figure 7.3(a)), which indicates that dislocation glide is not leading to a strain hardening effect. Furthermore, the LTC sample at a temperature $T = 353$ K shows a significant reduction in dislocation density in α' phase, disclosing a kind of stress-assisted recovery (SAR) within α' phase during LTC. Having in mind that SAMT and SIMT result in freshly formed α' phase of very high dislocation density, SAR almost balances this increase of dislocation density for temperatures $T \leq 323$ K and it even overcompensates for higher temperatures. SAR is a thermally activated process that is not restricted to the α' phase. It is very likely, that SAR occurs in the γ phase as well. However, a moderate increase of dislocation density occurs in the γ phase during LTC at the temperature $T = 353$ K. It indicates that the dislocation glide seems to become localized in the γ phase with increasing temperature T so that the reduction of dislocation density by SAR seems to be more than compensated by a strain hardening effect.

KAM maps generated by EBSD are considered to visually notice the microstructural changes that occurred due to LTC deformation. A major part of α' phase and γ phases prior to and post LTC have misorientation of only $0 - 1°$ (s. Figure 7.4). However, one can notice the significant microstructural changes due to LTC deformation (s. white box in Figure 7.5). The selected area contains an aggregation of spots with misorientation of $1 - 5°$ post LTC. A α' and γ phase specific KAM analyses (s. Figure 7.6(b, c)) disclose that the majority of spots with misorientation of $1 - 3°$ are made up by α' phase (s. Figure 7.6(b)). Owing to the same crystal structure, the SEM-EBSD data do not allow to distinguish the freshly formed α' phase from the existing α' matrix prior to LTC. Here it is assumed that these spots with misorientation of $1 - 3°$ might be low angle boundaries that arose due to rearrangement of dislocations during the SAR process in freshly formed α' phase. Within γ phase,

the spots with misorientation of $4-5°$ are more dominant (s. Figure 7.6(c)). On a microscopic scale, strain hardening due to localized dislocation glide in the γ phase raises the strain energy stored. In combination with SAR, low-angle boundaries arose due to the rearrangement of the increasing number of dislocations in the γ phase. It can be visualized in terms of misorientation in KAM maps.

Figure 8.2 shows the Schmid factor mapping specific to γ phase of the same area (s. Figure 7.4(b)) related to post LTC at temperature $T = 353\ K$ and stress $\sigma = 632\ MPa$. The black areas represent the α' phase. As shown in Figure 8.2, the γ phase has a distribution with CRSS of $0.28-0.50$. However, the area where significant microstructural changes occurred due to LTC deformation (s. white box in Figure 8.2) is identified as the region with a high CRSS of $0.46-0.50$, which is promoting the localized deformation within the γ phase.

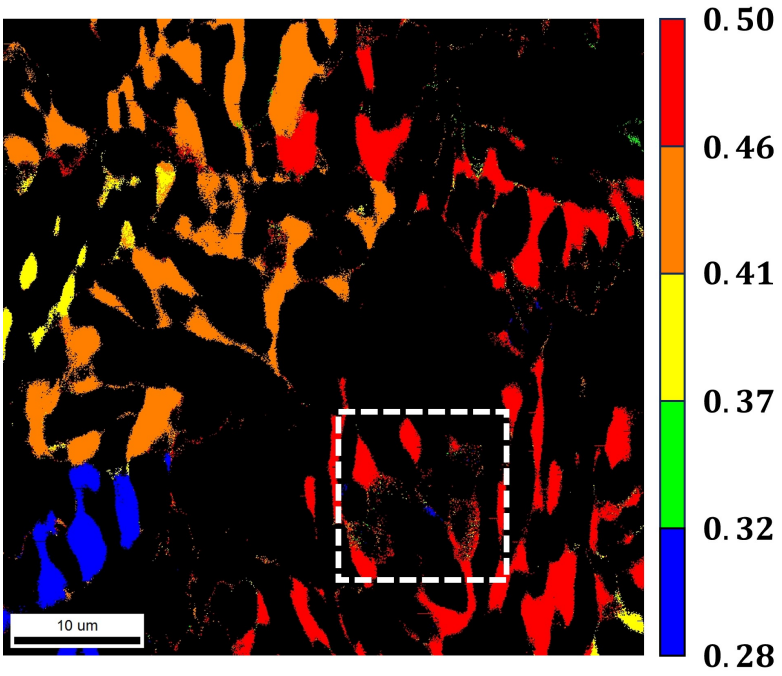

Figure 8.2: Schmid factor mapping of the same area (s. Figure 7.4(b)) specific to γ phase of martempered SAE 9254 post LTC performed at 353 K

In a nutshell, plastic deformation of martempered SAE 9254 during LTC is contributed by more than one mechanism: Dislocation glide localized in the metastable γ phase, and SAMT as well as SIMT. Furthermore, SAR in the α' and γ phases, SAMT as well as SIMT must be considered as LTC rate-controlling mechanisms. Therefore, the term Stress Assisted Plastic Deformation (SAPD) is introduced here to describe the overall phenomenon of the LTC deformation contributing mechanisms in martempered SAE 9254 as well as in MSS. It gets exhausted due to SAR, SAMT, and, at elevated temperature T, SIMT, hence, being the LTC rate-controlling mechanisms.

Chapter 9

Summary and Outlook

9.1 Summary

The rising demand for electric vehicles urges automotive suppliers to push their limits on the sag resistance of suspension coil springs or LTC resistance of MSS. Although various mechanisms are presumed to be LTC contributors in martensitic steels, i.e. dislocation glide, slip localization, and phase transformation (SAMT and/or TIT), the actual mechanisms behind the LTC strain in MSS are yet to be understood (refer to Chapter 2). Furthermore, the LTC rate-controlling mechanisms in MSS remain elusive.

A research approach of combined analysis by means of (i) an LTC mechanism-based model, and (ii) advanced microstructural characterization prior to and post LTC is considered to disclose the LTC rate-controlling mechanisms in SAE 9254 steel grade. A roadmap of the research approach to disclosing the LTC rate-controlling mechanisms is described in Chapter 3.

In Chapter 4, the LTC mechanism-based models are developed to make them capable of describing the stress σ and temperature T dependence of LTC strain, as well as creep parameters of martensitic steels.

In Chapter 6, both the modified SHT and reworked ECM are experimentally verified at the example of IQT SAE 9254. The modified SHT is incapable of describing the stress σ and temperature T dependence of the creep parameters $\alpha^S(T)$ and $\delta^S(\sigma, T)$. Consequently, the unqualified modified SHT is excluded for further validation. In contrast to that the reworked ECM is capable to describe the LTC strain ε_{cr} in IQT SAE 9254, as well as the stress σ and temperature T dependence of the creep parameters $n(T)$, $\alpha^E(\sigma, T)$, and $f_1^*(\sigma,T)/f_0^*(T)$, respectively. Furthermore, the magnitude of the derived activation volume ν_e and YS σ_e from the second stage fitting of creep parameters are supported in the validation of reworked ECM. It is observed that the fraction of the γ phase in IQT SAE 9254 dropped by 15% of its initial amount during

LTC deformation irrespective of the test temperature T. Based on these experimental results, a hypothesis of the LTC rate-controlling mechanisms in IQT SAE 9254 is proposed. However, it is challenging to validate the hypothesis at the example of IQT SAE 9254 which contains a rather low volume fraction of γ phase (8.9%) in the form of nano-islands.

In Chapter 7, the martempered SAE 9254 is considered to validate the proposed hypothesis of the LTC rate-controlling mechanisms in SAE 9254. First and foremost, the reworked ECM is verified and validated at the example of martempered SAE 9254. The microstructural changes due to LTC determined by XRD, as well as KAM, and respective phase maps obtained from EBSD are firm support to the proposed hypothesis of the LTC rate-controlling mechanisms (refer to Chapter 8).

In a nutshell, plastic deformation of SAE 9254 steel grade during LTC is contributed by more than one mechanism: Dislocation glide localized in the metastable γ phase, and SAMT as well as SIMT. Furthermore, SAR in the α' and γ phases, SAMT as well as SIMT must be considered as LTC rate-controlling mechanisms. Therefore, the term Stress Assisted Plastic Deformation (SAPD) is introduced here to describe the overall phenomenon of the LTC deformation contributing mechanisms in martempered SAE 9254 as well as in MSS. It gets exhausted due to SAR, SAMT, and, at elevated temperature T, SIMT, hence, being the LTC rate-controlling mechanisms.

9.2 Outlook

In the current studies, the freshly formed α' phase during LTC deformation is not distinguished from the existing α' matrix of martempered SAE 9254 owing to the fact that the conventional EBSD technique can't distinguish phases having a same crystal structure. However, the latest work of Blankart et al.[106] and Kang et al.[107] have proven that EBSD is able to distinguish between the freshly formed α' phase and the existing α' matrix of a material using the grain-average band slope analysis. The consideration of this state-of-the-art analysis further strengthens the evidence to validate the hypothesis of LTC rate-controlling mechanisms in SAE 9254. Besides, an *in-situ* LTC testing is well suited to substantiate the proposed LTC rate-controlling mechanisms.

The SAMT and SIMT have significant contributions to LTC strain along with dislocation glide in MSS in the temperatures $298\ K \leq T \leq 353\ K$. However, these mechanisms are not considered in the developed LTC models. Furthermore, the dislocation density ρ_m of SAE 9254 steel grade changes during LTC deformation. However, it is considered as a slowly varying function in time t while developing the LTC mod-

els. These changes must be implemented for further development of the sophisticated LTC mechanism-based model.

Appendix A

Determination of Texture in a Steel

According to SAE 453 method[99], the peaks {200}, {220} of γ phase should consider to determine the degree of texture in a steel. The texture in steel is classified as random or low, medium, and severe textures based on the percentage of deviation ($\%D$) which is defined as

$$\%D = \frac{I_r - R_r}{R_r} \cdot 100 \tag{A.1}$$

with the ratio of experimentally measured area under the peaks (I_r) and the ratio of theoretically determined area under the peaks (R_r)

$$I_r = \frac{I_\gamma^{220}}{I_\gamma^{200}} \quad \text{and} \quad R_r = \frac{R_\gamma^{220}}{R_\gamma^{200}}. \tag{A.2}$$

Here I_γ^{200}, I_γ^{220} are the experimentally measured area under the respective peaks, whereas R_γ^{200}, R_γ^{220} are theoretically determined area under the respective peaks in randomly oriented crystallographic steel. The R-values of the peaks for SAE 9254 steel composition are calculated as described in Ref.[99] and presented here in Table A.1. The data required for the determination of R-values is available in Refs.[94;104].

Table A.1: The R-values of for the peaks {200}, {220} of γ phase and {200}, {211} peaks of α' phase for SAE 9254 steel composition

Peak	R-value
γ_{200}	35.90
γ_{220}	49.31
α'_{200}	20.90
α'_{211}	180.20

Appendix B

LTC Data of IQT SAE 9254 and Martempered SAE 9254

A set of three specimens denoted as S1, S2, and S3, was tested at each condition. Here presented, the LTC strain data of IQT SAE 9254 (s. Figure B.1 and Figure B.2) and martempered SAE 9254 (s. Figure B.3 and Figure B.4).

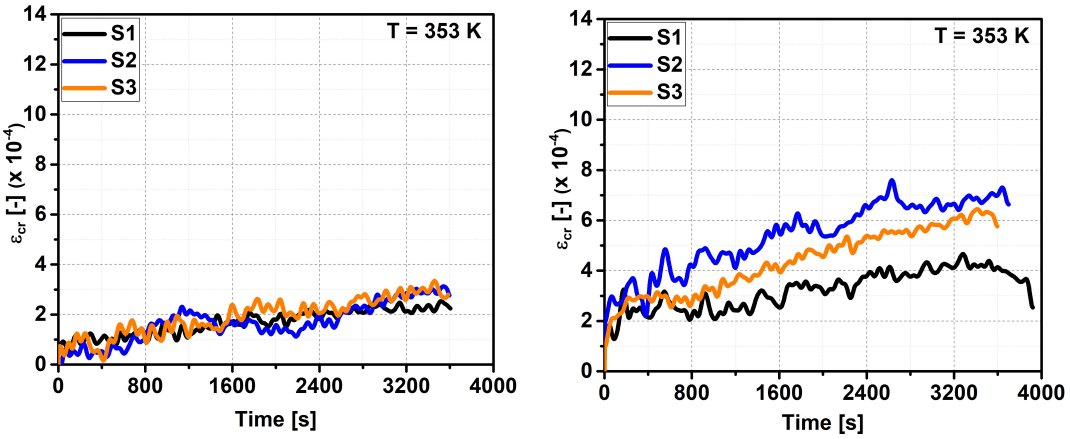

(a) (b)

Figure B.1: LTC data of IQT SAE 9254 performed at (a) 1071 MPa, (b) 1428 MPa at constant temperature $T = 353\ K$

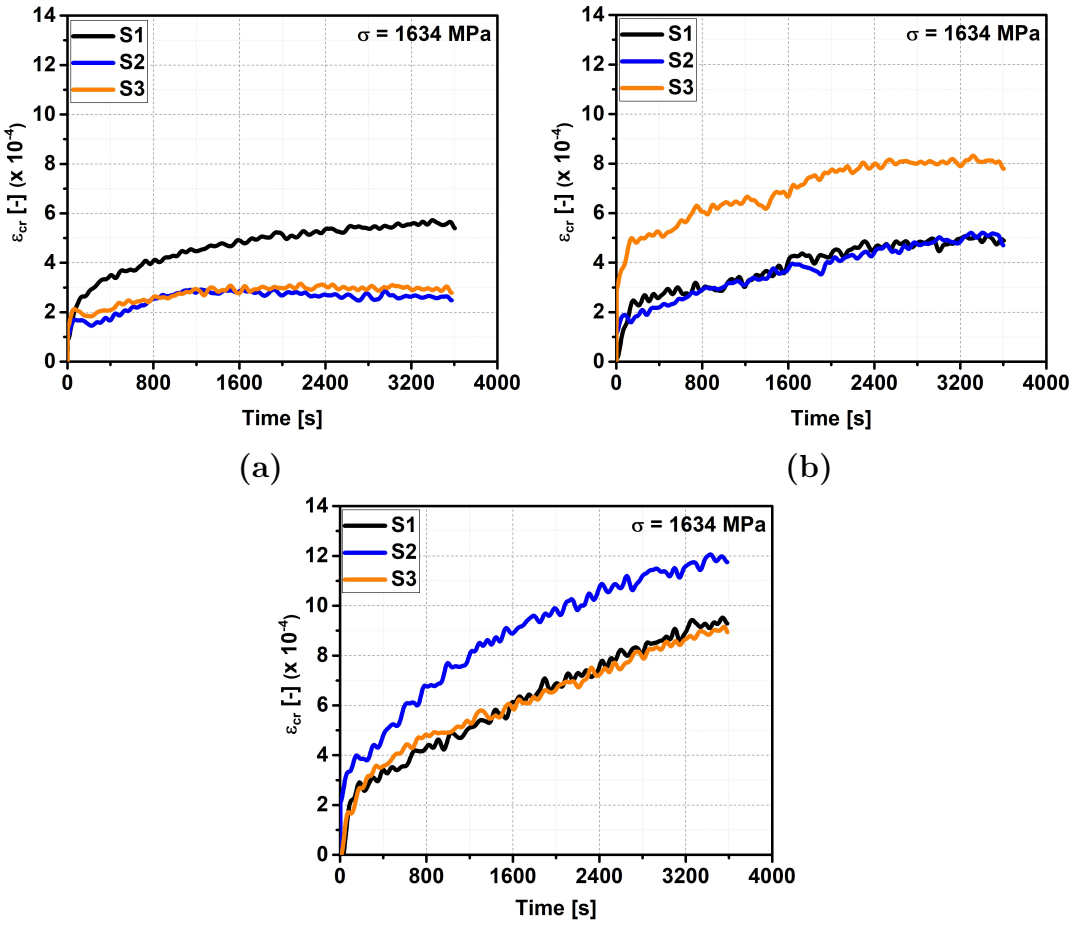

Figure B.2: LTC data of IQT SAE 9254 performed at (a) 298 K, (b) 323 K, (c) 353 K at constant stress $\sigma = 1634\ MPa$

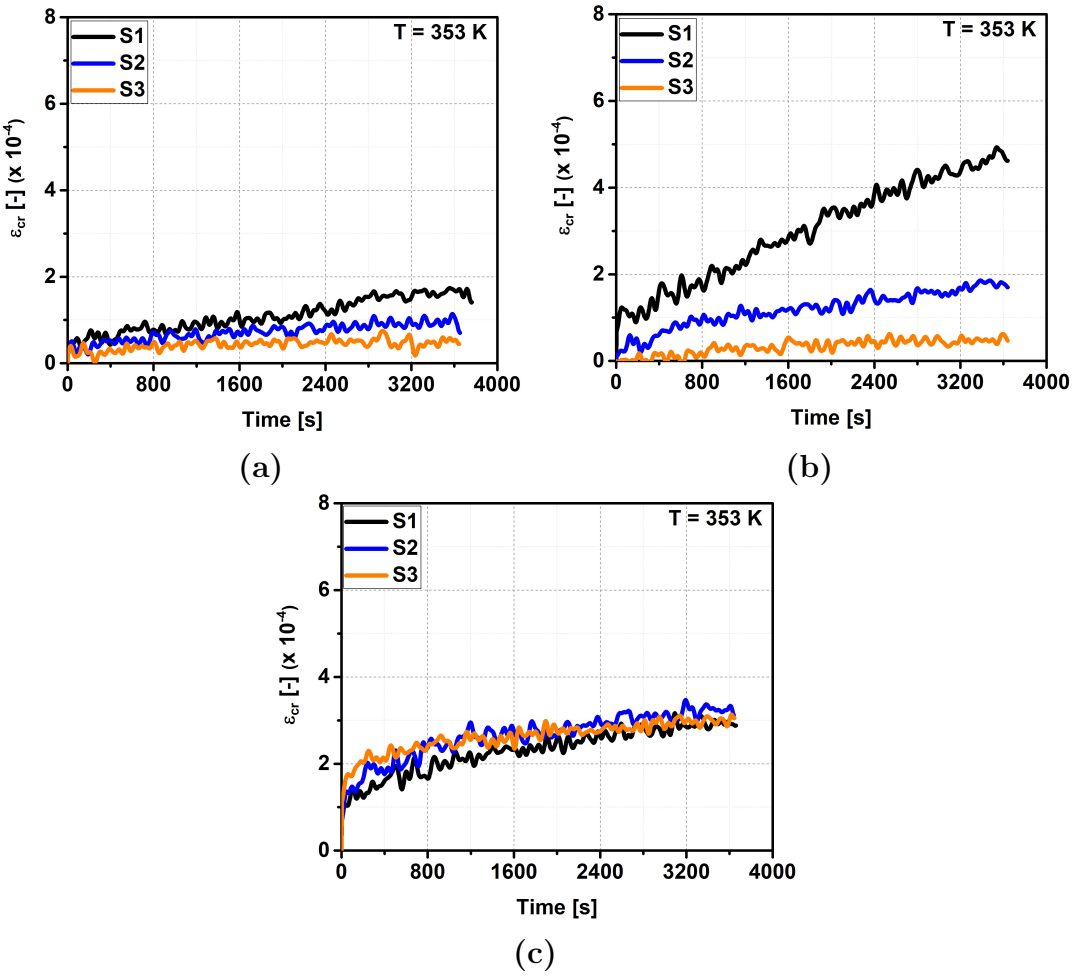

Figure B.3: LTC data of martempered SAE 9254 performed at (a) 421 MPa, (b) 492 MPa, (c) 562 MPa and at constant temperature $T = 353\ K$

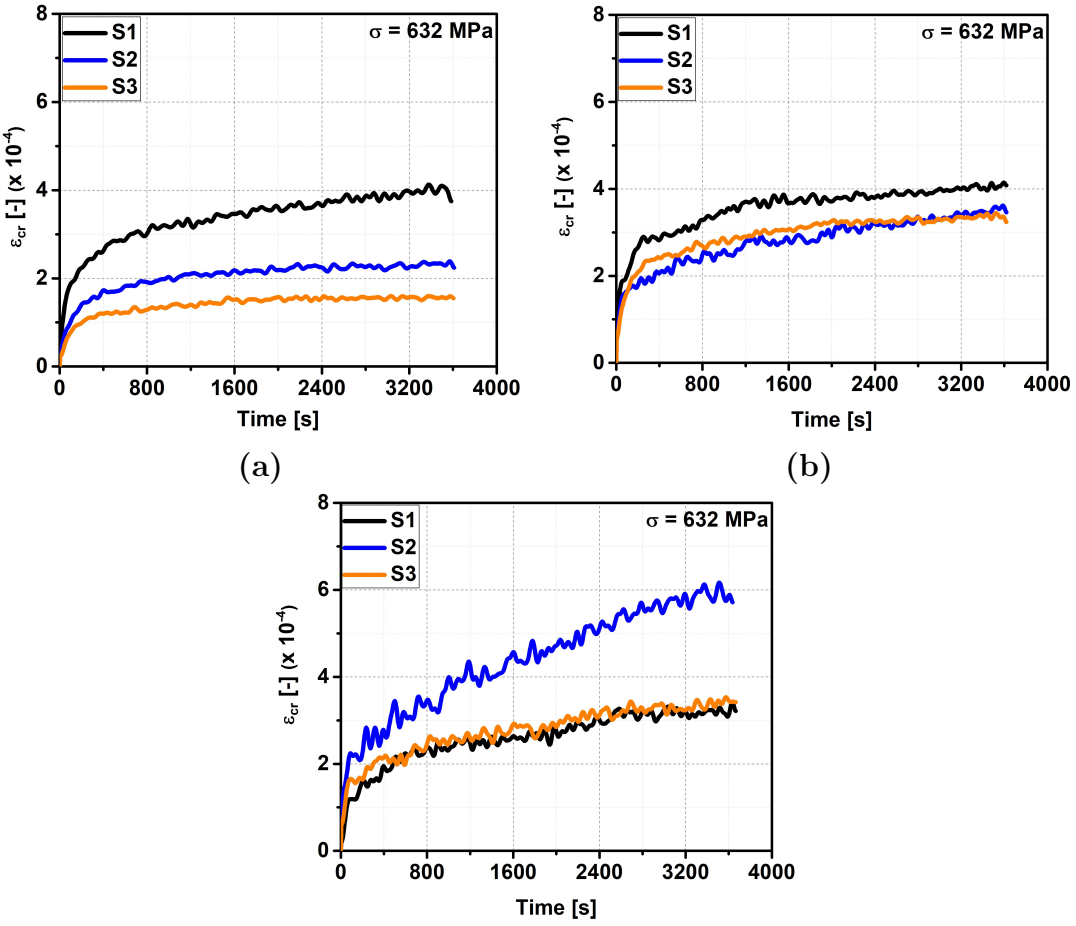

Figure B.4: LTC data of martempered SAE 9254 performed at (a) 298 K, (b) 323 K, (c) 353 K and at constant stress $\sigma = 632\ MPa$

Bibliography

[1] HJ Tata, ER Driscoll, and JJ Kary. Steels for automotive coil springs with improved resistance to relaxation. *SAE Transactions*, pages 1862–1876, 1980.

[2] Kazuhiro Kawasaki, Yoshiki Seto, Takao Yamazaki, and Toshio Hijikata. Properties of induction heat-treated high-strength spring wire. Technical report, SAE Technical Paper, 1983.

[3] Kazuhiro KAWASAKI, Takayo CHIBA, Norihisa TAKAOKA, and Takao YAMAZAKI. Micro-structure and mechanical properties of induction heating quenched and tempered spring steel. *Tetsu-to-Hagane*, 73(16):2290–2297, 1987.

[4] Kazuhiro KAWASAKI, Takayo CHIBA, and Takao YAMAZAKI. Characteristics of micro-structure of induction heating tempered spring steel. *Tetsu-to-Hagane*, 74(2):342–349, 1988.

[5] Toshiro Yamamoto, Ryohei Kobayashi, Toshio Ozone, and Mamoru Kurimoto. Precipitation-strengthened spring steel for automotive suspensions. *Journal of Heat Treating*, 3(3):220–227, 1984.

[6] M Assefpour-Dezfuly and A Brownrigg. Parameters affecting sag resistance in spring steels. *Metallurgical Transactions A*, 20(10):1951–1959, 1989.

[7] Teruyuki Murai, Seizo Takamuku, and Nobuharu Takenoshita. High sag resistance spring wire for automotive suspension. *SAE transactions*, pages 298–304, 1985.

[8] Teruyuki Murai, Hideo Ogita, Seizo Takamuku, and Norihisa Matsushima. Steel wire for a spring and method for the production thereof, July 3 1990. US Patent 4,938,811.

[9] Zhenbo Zhao, Derek O Northwood, Cheng Liu, and Yunxu Liu. A new method for improving the resistance of high strength steel wires to room temperature creep and low cycle fatigue. *Journal of Materials Processing Technology*, 89:569–573, 1999.

[10] Cheng Liu, Zhe Zhao, and Derek O Northwood. Effect of heat treatments on room temperature creep strain of a high strength steel. In *Key Engineering Materials*, volume 171, pages 403–410. Trans Tech Publ, 2000.

[11] Cheng Liu, Ping Liu, Zhenbo Zhao, and Derek O Northwood. Room temperature creep of a high strength steel. *Materials & Design*, 22(4):325–328, 2001.

[12] Cheng Liu, Sanjiwan Bhole, and Derek Northwood. The effects of ferrite content and morphology on the mechanical properties and room temperature creep of quenched and tempered sae 4340 steel. *JSME International Journal Series A Solid Mechanics and Material Engineering*, 46(3):272–277, 2003.

[13] A Oehlert and A Atrens. Room temperature creep of high strength steels. *Acta metallurgica et materialia*, 42(5):1493–1508, 1994.

[14] George Ellwood Dieter and David Bacon. *Mechanical metallurgy*, volume 3. McGraw-hill New York, 1976.

[15] WH Miller, RT Chen, and EA Starke. Microstructure, creep, and tensile deformation in ti-6al-2nb-1ta-0.8 mo. *Metallurgical Transactions A*, 18(8):1451–1468, 1987.

[16] T Neeraj, D-H Hou, GS Daehn, and MJ Mills. Phenomenological and microstructural analysis of room temperature creep in titanium alloys. *Acta materialia*, 48(6):1225–1238, 2000.

[17] Tatsuya Kameyama, Tetsuya Matsunaga, Eiichi Sato, and Kazuhiko Kuribayashi. Suppression of ambient-temperature creep in cp-ti by cold-rolling. *Materials Science and Engineering: A*, 510:364–367, 2009.

[18] TH Alden. Strain hardening during low temperature creep of 304 stainless steel. *Acta metallurgica*, 35(11):2621–2626, 1987.

[19] ME Kassner, P Geantil, and RS Rosen. Ambient temperature creep of type 304 stainless steel. *Journal of engineering materials and technology*, 133(2), 2011.

[20] Sheng-Hui Wang, Yonggang Zhang, and Weixing Chen. Room temperature creep and strain-rate-dependent stress-strain behavior of pipeline steels. *Journal of Materials Science*, 36(8):1931–1938, 2001.

[21] C Yen, T Caulfield, LD Roth, JM Wells, and JK Tien. Creep of copper at cryogenic temperatures. *Cryogenics*, 24(7):371–377, 1984.

[22] Junjie Shen, Shigeto Yamasaki, Ken-ichi Ikeda, Satoshi Hata, and Hideharu Nakashima. Low-temperature creep at ultra-low strain rates in pure aluminum studied by a helicoid spring specimen technique. *Materials transactions*, 52(7):1381–1387, 2011.

[23] Michael E Kassner and Kamia Smith. Low temperature creep plasticity. *Journal of materials research and technology*, 3(3):280–288, 2014.

[24] Richard William Neu. *An investigation into the mechanisms of cone bore growth in railroad bearings*. PhD thesis, University of Illinois at Urbana-Champaign, 1991.

[25] RW Neu and Huseyin Sehitoglu. Low-temperature creep of a carburized steel. *Metallurgical Transactions A*, 23(9):2619–2624, 1992.

[26] Bo Alfredsson, I Linares Arregui, and J Lai. Low temperature creep in a high strength roller bearing steel. *Mechanics of Materials*, 100:109–125, 2016.

[27] Mathias Münch, Robert Brandt, and Nagarjuna Remalli. A verification of mechanism based theories for low temperature creep of high strength steel. In *Proceedings of the Ilmenauer Federntag Conference, Ilmenau, Germany*, 2021.

[28] Nagarjuna Remalli, Mathias Münch, Mohsin Hasan, K Nanda Kishore, Felix Stern, Nikolas Baak, Frank Walther, Manjini Sambandam, Steffen Klapprott, Koteswararao V Rajulapati, et al. On the low temperature creep controlling mechanism in a high strength spring steel. *Journal of Materials Research and Technology*, 21:2309–2315, 2022.

[29] Won Jong Nam, Chong Soo Lee, and Deok Young Ban. Effects of alloy additions and tempering temperature on the sag resistance of si–cr spring steels. *Materials Science and Engineering: A*, 289(1-2):8–17, 2000.

[30] ST Furr. Development of a new laboratory test method for spring steels. 1972.

[31] Sangwoo Choi. Optimization of microstructure and properties of high strength spring steel. 2011.

[32] Stéphane AJ Forsik and Pedro EJ Rivera-Diaz-del Castillo. Martensitic steels: epsilon carbides in tempered. *Encyclopedia of Iron, Steel, and Their Alloys; CRC Press: Boca Raton, FL, USA*, pages 2169–2181, 2016.

[33] AG Allten and P Payson. The effect of silicon on the tempering of martensite. *Transactions of the American Society for Metals*, 45:498–532, 1953.

[34] WS Owen. The effect of silicon on the kinetics of tempering. *Transactions of the American Society for Metals*, 46:812–829, 1954.

[35] CJ Altstetter, Morris Cohen, and BL Averbach. Effect of silicon on the tempering of aisi 43xx steels. *Transactions of the ASM*, 55(1):287–300, 1962.

[36] J Gordine and I Codd. The influence of silicon up to 1. 5 wt.-per cent on the tempering characteristics of a spring steel. *J Iron Steel Inst*, 207(4):461–467, 1969.

[37] WJ Nam and HC Choi. Effect of si on mechanical properties of low alloy steels. *Materials science and technology*, 15(5):527–530, 1999.

[38] R Padmanabhan and WE Wood. Precipitation of ϵ carbide in martensite. *Materials Science and Engineering*, 65(2):289–297, 1984.

[39] G Miyamoto, T Furuhara, T Maki, JC Oh, and K Hono. Effect of si addition on the precipitation of iron carbide in tempered high carbon martensite. In *International Conference on Solid-Solid Phase Transformations in Inorganic Materials 2005*, 2005.

[40] Won Jong Nam, Dae Sung Kim, and Soon Tae Ahn. Effects of alloying elements on microstructural evolution and mechanical properties of induction quenched-and-tempered steels. *Journal of materials science*, 38:3611–3617, 2003.

[41] Mohsin Hasan. *Development of advanced high strength spring steels and evaluating its high cycle fatigue properties*. PhD thesis, University of Hyderabad, under preparation.

[42] TV Sharma Rajan, CP Sharma, and Ashok Kumar Sharma. *Heat treatment: principles and techniques*. PHI Learning Pvt. Ltd., 2011.

[43] George Krauss. Principles of heat treatment of steel. *American Society for Metals, 1980,*, page 291, 1980.

[44] G Krauss. Tempering of martensite in carbon steels. In *Phase transformations in steels*, pages 126–150. Elsevier, 2012.

[45] KH Jack. Results of further x-ray structural investigations of the iron–carbon and iron–nitrogen systems and of related interstitial alloys. *Acta Crystallographica*, 3(5):392–394, 1950.

[46] CS Roberts, BL Averbach, and Morris Cohen. The mechanism and kinetics of the 1st stage of tempering. *Transactions of the American Society for Metals*, 45:576–604, 1953.

[47] KW Andrews. The structure of cementite and its relation to ferrite. *Acta Metallurgica*, 11(8):939–946, 1963.

[48] KW Andrews. The structure of cementite and its relation to ferrite and epsilon carbide—ii. *Acta Metallurgica*, 12(8):921–929, 1964.

[49] Mathias Münch. *Low Temperature Creep of high strength spring steel.* PhD thesis, University of Siegen, under preparation.

[50] Stephanie Sackl, Michael Zuber, Helmut Clemens, and Sophie Primig. Induction tempering vs conventional tempering of a heat-treatable steel. *Metallurgical and materials transactions a*, 47:3694–3702, 2016.

[51] Stephanie Sackl, Harald Leitner, Michael Zuber, Helmut Clemens, and Sophie Primig. Induction hardening vs conventional hardening of a heat treatable steel. *Metallurgical and Materials Transactions A*, 45:5657–5666, 2014.

[52] Binbin He. On the factors governing austenite stability: intrinsic versus extrinsic. *Materials*, 13(15):3440, 2020.

[53] Christina Schröder, Marco Wendler, Olena Volkova, and Andreas Weiß. Microstructure and mechanical properties of an austenitic crmnnimon spring steel strip with a reduced ni content. *Crystals*, 10(5):392, 2020.

[54] Tsuguyasu Wada, Harue Wada, John F Elliott, and John Chipman. Thermodynamics of the fcc fe-mn-c and fe-si-c alloys. *Metallurgical Transactions*, 3:1657–1662, 1972.

[55] HKDH Bhadeshia and DV Edmonds. The bainite transformation in a silicon steel. *Metallurgical Transactions A*, 10:895–907, 1979.

[56] Harshad Kumar Dharamshi Hansraj Bhadeshia and JW Christian. Bainite in steels. *Metallurgical transactions A*, 21:767–797, 1990.

[57] Cheruvu N Sastry and William E Wood. On the presence of retained austenite at the prior austenite grain boundaries of aisi 4340 steel. *Materials Science and Engineering*, 45(3):277–280, 1980.

[58] Feiyu Zhao, Peng Chen, Baoyu Xu, Qian Yu, R Devesh K Misra, Guodong Wang, and Hongliang Yi. Martensite transformation of retained austenite with diverse stability and strain partitioning during tensile deformation of a carbide-free bainitic steel. *Materials Characterization*, 179:111327, 2021.

[59] A Saha Podder, I Lonardelli, A Molinari, and HKDH Bhadeshia. Thermal stability of retained austenite in bainitic steel: an in situ study. *Proceedings of the Royal Society A: Mathematical, Physical and Engineering Sciences*, 467(2135):3141–3156, 2011.

[60] Peter Hedström, Lars-Erik Lindgren, J Almer, U Lienert, J Bernier, Mark Terner, and Magnus Odén. Load partitioning and strain-induced martensite formation during tensile loading of a metastable austenitic stainless steel. *Metallurgical and Materials Transactions A*, 40:1039–1048, 2009.

[61] Derek Hull and David J Bacon. *Introduction to dislocations*, volume 37. Elsevier, 2011.

[62] G Meric De Bellefon, JC Van Duysen, and K Sridharan. Composition-dependence of stacking fault energy in austenitic stainless steels through linear regression with random intercepts. *Journal of Nuclear Materials*, 492:227–230, 2017.

[63] Donald T Pierce, José Antonio Jiménez, James Bentley, Dierk Raabe, C Oskay, and JE Wittig. The influence of manganese content on the stacking fault and austenite/ε-martensite interfacial energies in fe–mn–(al–si) steels investigated by experiment and theory. *Acta Materialia*, 68:238–253, 2014.

[64] RM Latanision and AW Ruff. The temperature dependence of stacking fault energy in fe-cr-ni alloys. *Metallurgical Transactions*, 2:505–509, 1971.

[65] David Rafaja, Christiane Ullrich, Mykhaylo Motylenko, and Stefan Martin. Microstructure aspects of the deformation mechanisms in metastable austenitic steels. In *Austenitic TRIP/TWIP Steels and Steel-Zirconia Composites: Design of Tough, Transformation-Strengthened Composites and Structures*, pages 325–377. Springer, 2020.

[66] O Grässel, G Frommeyer, C Derder, and H Hofmann. Phase transformations and mechanical properties of fe-mn-si-al trip-steels. *Le Journal de Physique IV*, 7(C5):C5–383, 1997.

[67] A Dumay, J-P Chateau, S Allain, S Migot, and O Bouaziz. Influence of addition elements on the stacking-fault energy and mechanical properties of an austenitic fe–mn–c steel. *Materials Science and Engineering: A*, 483:184–187, 2008.

[68] Christiane Ullrich, Stefan Martin, Christian Schimpf, Andreas Stark, Norbert Schell, and David Rafaja. Deformation mechanisms in metastable austenitic

trip/twip steels under compressive load studied by in situ synchrotron radiation diffraction. *Advanced Engineering Materials*, 21(5):1801101, 2019.

[69] U Krupp, I Roth, HJ Christ, M Kübbeler, and CP Fritzen. On the mechanism of martensite formation during short fatigue crack propagation in austenitic stainless steel: experimental identification and modelling concept. In *Proceedings of the 13th International Conference on Fracture, Beijing, China*, 2013.

[70] RW Neu and Huseyin Sehitoglu. Transformation of retained austenite in carburized 4320 steel. *Metallurgical Transactions A*, 22:1491–1500, 1991.

[71] GB Olson and Morris Cohen. Stress-assisted isothermal martensitic transformation: application to trip steels. *Metallurgical Transactions A*, 13:1907–1914, 1982.

[72] RW Neu and Huseyin Sehitoglu. Stress-induced transformation in a carburized steel—experiments and analysis. *Acta metallurgica et materialia*, 40(9):2257–2268, 1992.

[73] GB Olson and Morris Cohen. A mechanism for the strain-induced nucleation of martensitic transformations. *Journal of the Less Common Metals*, 28(1):107–118, 1972.

[74] GB Olson and Morris Cohen. Kinetics of strain-induced martensitic nucleation. *Metallurgical transactions A*, 6(4):791–795, 1975.

[75] Ivan Gutiérrez-Urrutia and Dierk Raabe. Multistage strain hardening through dislocation substructure and twinning in a high strength and ductile weight-reduced fe–mn–al–c steel. *Acta Materialia*, 60(16):5791–5802, 2012.

[76] Donald T Pierce, Jose Antonio Jiménez, James Bentley, Dierk Raabe, and James E Wittig. The influence of stacking fault energy on the microstructural and strain-hardening evolution of fe–mn–al–si steels during tensile deformation. *Acta Materialia*, 100:178–190, 2015.

[77] Frederick Harwood Norton. *The creep of steel at high temperatures*. Number 35. McGraw-Hill Book Company, Incorporated, 1929.

[78] RW Bailey. The utilization of creep test data in engineering design. *Proceedings of the Institution of Mechanical Engineers*, 131(1):131–349, 1935.

[79] OH Wyatt. Transient creep in pure metals. *Proceedings of the Physical Society. Section B*, 66(6):459, 1953.

[80] Frank Garofalo. Fundamentals of creep and creep-rupture in metals(creep and creep rupture in metals and alloys, fundamental information for instruction and reference). *NEW YORK, MACMILLAN CO., LONDON, COLLIER- MACMILLAN, LTD., 1965. 258 P*, 1965.

[81] HKDH Bhadeshia. Steels for bearings. *Progress in materials Science*, 57(2):268–435, 2012.

[82] EJ Orowan. West of scotland iron and steel institute. *Paper read*, 14, 1947.

[83] FRN Nabarro. Theory of crystal dislocations oxford. *Clarendon P*, 1967.

[84] FRN Nabarro. The time constant of logarithmic creep and relaxation. *Materials Science and Engineering: A*, 309:227–228, 2001.

[85] CL Smith. A theory of transient creep in metals. *Proceedings of the Physical Society (1926-1948)*, 61(3):201, 1948.

[86] Alfred Seeger, J Diehl, Siegfried Mader, and H Rebstock. Work-hardening and work-softening of face-centred cubic metal crystals. *Philosophical Magazine*, 2(15):323–350, 1957.

[87] AH Cottrell. The time laws of creep. *Journal of the Mechanics and Physics of Solids*, 1(1):53–63, 1952.

[88] DO Welch and R Smoluchowski. Exhaustion theory of creep in metals at low temperatures. *Journal of Physics and Chemistry of Solids*, 33(5):1115–1127, 1972.

[89] AH Cottrell. Logarithmic and andrade creep. *Philosophical magazine letters*, 75(5):301–308, 1997.

[90] Flake C Campbell. *Elements of metallurgy and engineering alloys*. ASM international, 2008.

[91] Milton Abramowitz and Irene A Stegun. *Handbook of mathematical functions with formulas, graphs, and mathematical tables*, volume 55. US Government printing office, 1948.

[92] ASTM Subcommittee. *Standard test methods for determining average grain size*. ASTM International, 1996.

[93] NIST Srm. 660a; lanthanum hexaboride powder line position and line shape standard for powder diffraction. *Certificate, National Institute of Standards and Technology, US Department of Commerce: Gaithersburg, MD, USA*, 2000.

[94] Bernard Dennis Cullity. *Elements of X-ray Diffraction*. Addison-Wesley Publishing, 1956.

[95] Farideh HajyAkbary. Optimising mechanical behaviour of new advanced steels based on fine non-equilibrium microstructures. 2015.

[96] Davor Balzar and Hassel Ledbetter. Voigt-function modeling in fourier analysis of size-and strain-broadened x-ray diffraction peaks. *Journal of Applied Crystallography*, 26(1):97–103, 1993.

[97] John J Olivero and RL Longbothum. Empirical fits to the voigt line width: A brief review. *Journal of Quantitative Spectroscopy and Radiative Transfer*, 17(2):233–236, 1977.

[98] T Ungár, I Dragomir, Á Révész, and A Borbély. The contrast factors of dislocations in cubic crystals: the dislocation model of strain anisotropy in practice. *Journal of applied crystallography*, 32(5):992–1002, 1999.

[99] Chester F Jatczak. Retained austenite and its measurement by x-ray diffraction. *SAE Transactions*, pages 1657–1676, 1980.

[100] Sudook A Kim and Ward L Johnson. Elastic constants and internal friction of martensitic steel, ferritic-pearlitic steel, and α-iron. *Materials Science and Engineering: A*, 452:633–639, 2007.

[101] Richard Palmer Reed and NJ Simon. *Materials Studies for Magnetic Fusion Energy Applications at Low Temperatures, IV*. US Department of Commerce, National Bureau of Standards, 1981.

[102] Bohdan Sestäk and Alfred Seeger. Gleitung und verfestigung in kubisch-raumzentrierten metallen und legierungen. *International Journal of Materials Research*, 69(4):195–202, 1978.

[103] American Society for Testing and Materials. *Standard practice for X-ray determination of retained austenite in steel with near random crystallographic orientation*. ASTM International, 2013.

[104] Arthur James Cochran Wilson and V Geist. International tables for crystallography. volume c: Mathematical, physical and chemical tables. kluwer academic publishers, dordrecht/boston/london 1992 (published for the international union of crystallography), 883 seiten, isbn 0-792-3-16-38x, 1993.

[105] H Conrad. Thermally activated deformation of metals. *Jom*, 16(7):582–588, 1964.

[106] Charline Blankart, Robin Emmrich, Lars Bähren, and Ulrich Krupp. Influence of press-hardening in combination with quenching and partitioning treatment on the microstructure of medium manganese steel. *steel research international*, page 2200907, 2023.

[107] Jun-Yun Kang, Seong-Jun Park, and Man-Been Moon. Phase analysis on dual-phase steel using band slope of electron backscatter diffraction pattern. *Microscopy and Microanalysis*, 19(S5):13–16, 2013.

List of Publications

Publications

1. **N. Remalli**, M. Münch, M. Hasan, K. N. Kishore, F. Stern, et al., "On the Low Temperature Creep Controlling Mechanism in a High Strength Spring Steel", Journal of Materials Research and Technology; 2022; vol. 21; 2309-2315.

2. **N. Remalli**, M. Hasan, K. N. Kishore, G. Rajavel, M. Münch, et al., "Pivotal Role of Retained Austenite as a Low Temperature Creep Controlling Mechanism in a Martensitic Spring Steel", Journal of Materials Science & Engineering: A, 2023; vol. 887; 145751.

3. R. Brandt, **N. Remalli**, M. Münch, "On the Nature of Low Temperature Creep Mechanism-Based Models", to be submitted.

Conference Proceedings

1. M. Münch, R. Brandt, **N. Remalli**, "A Verification of Mechanism-Based Theories for Low Temperature Creep of High Strength Steel," Ilmenauer Federntag 2021, Germany on 7th October 2021.

2. M. Münch, **N. Remalli**, R. Brandt, "Low Temperature Creep of Martensitic Steels under Tensile Loading," 4th International ECCC conference, Germany on 7-10 September 2017.

Oral Presentations

1. **N. Remalli**, R. Brandt, "An Insight into the Low Temperature Creep Mechanism in High Strength Steel" in Indo-German Workshop on Advanced Automotive Steels (IGWAAS-2021), March 4-5, 2021